UNIVERSITÀ DEGLI STUDI DI PADOVA


SCUOLA DI SCIENZE

Dipartimento di Geoscienze

Direttore Prof. Fabrizio Nestola


TESI DI LAUREA MAGISTRALE

IN

GEOLOGIA E GEOLOGIA TECNICA

# A study on the contribution of satellite RADAR interferometry to analyse the activity of Aso volcano (Japan)


Relatore: **Prof. Mario Floris**

Correlatori: **Prof. Andrea Marzoli**
**Dott.ssa Giulia Tessari**

Laureanda: **Silvia Puliero**

Matricola: **1141688**


**ANNO ACCADEMICO 2017/2018**

# Riassunto

Lo scopo di questo lavoro è comparare l'uso di dati SAR acquisiti da differenti sensori e capire quale di questi riesce a stimare meglio piccoli e grandi spostamenti in aree vulcaniche, mantenendo una buona informazione spaziale. Tramite la ricostruzione dell'evoluzione delle deformazioni, è possibile analizzare il comportamento dell'edificio vulcanico prima, durante e dopo un'eruzione.

Lo studio è focalizzato sul vulcano Aso, nella parte centrale dell'isola di Kyushu (Giappone), che si distingue per la sua ampia caldera (18 km x 25 km). Al suo interno è contenuta la parte di coni post calderici giovani più di 0.1 Ma. Tra i 17 coni, l'unico attivo da 80 anni è il Nakadake, composto da sette crateri più piccoli. Nell'intervallo di tempo considerato (2007-2018), non si sono verificate grandi eruzioni; durante il periodo di instabilità, una prevalente subsidenza si è manifestata contemporaneamente all'attività di degassamento. Sebbene la scarsa intensità dell'attività, gli spostamenti del terreno, rilevabili tramite tecniche di telerilevamento, possono riflettere i cicli di riempimento-sgonfiamento della camera magmatica, situata al di sotto del principale cratere inattivo (Kusasenri), ad una profondità di 4-5 km.

Usando la tecnica InSAR *Small Baseline Subset* (SBAS), i dati SAR ALOS Palsar-1 dal 2007 al 2011, Sentinel-1 dal 2014 al 218 e ALOS Palsar-2 dal 2016 al 2018 sono stati calibrati tramite misure del *Global Navigation Satellite System* (GNSS).

Con l'utilizzo del software SARscape, per ogni arco temporale, sono state create delle mappe di velocità e spostamento per ottenere delle serie temporali di deformazioni per analizzare e identificare i movimenti dovuti all'attività vulcanica. Un importante evento sismico verificatosi durante il periodo temporale investigato, è il terremoto di Kumamoto di magnitudo $M_w$ 7.0 avvenuto il 16 Aprile 2016, a 60 km di distanza dal bordo della caldera. Sia dalle serie temporali dei GPS che da quelle SAR è stato importante escludere l'effetto cosismico per stimare un corretto movimento dovuto all'attività del vulcano.

Nelle serie temporali di spostamento, per ogni arco temporale, sono stati esaminati tre punti in corrispondenza della localizzazione dei GPS interni alla caldera e alcuni punti nella parte coni post calderici. Analizzando queste serie è necessario considerare che le

deformazioni sono influenzate da molti fattori come la geodinamica, effetti atmosferici, il rumore, il tipo di processamento adoperato per le immagini e i terremoti, oltre all'attività vulcanica e alle caratteristiche del sensore usato per le acquisizioni.

I risultati finali mostrano che solo nel caso di un tempo di rivisitazione del satellite più corto e una minore lunghezza d'onda è possibile rilevare le attività poco intense, ma a volte, usare dati SAR con un tempo di rivisitazione maggiore e una lunghezza d'onda più grande, può aiutare ad ottenere una migliore informazione spaziale in aree vegetate, come nel caso della caldera del vulcano Aso.

# Abstract

The aim of this work is to compare the use of SAR datasets acquired by different sensors and understand which one has the best performance estimating from small to large ground displacements in volcanic area, maintaining a good spatial information. Through the reconstruction of the deformations evolution, it is possible to analyse the behaviour of the volcanic edifice before, during and after eruptions.

The study is focused on Aso volcano, in the central part of the Kyushu island (Japan), which stands out for its wide caldera (18 km x 25 km). Inside the rim is included the post-caldera central cones younger than 0.1 Ma. Among 17 cones, the only crater which has been active for 80 years is Nakadake, composed by seven craterlets. In the considered time span (2007-2018), no large eruptions occurred; during its unrest period, a prevalent subsidence has persisted simultaneously with the degassing activity. Although the low intensity activity, ground displacements, detectable through remote sensing techniques, can reflect the inflate-deflate cycles of the magma chamber, situated below one of the main inactive crater (Kusasenri) at a depth of 4-5 km.

Using *Small Baseline Subset* (SBAS) InSAR technique, ALOS Palsar-1 from 2007 to 2011, Sentinel-1 from 2014 to 2018 and ALOS Palsar-2 from 2016 to 2018 SAR datasets have been calibrated through *Global Navigation Satellite System* (GNSS) measurements. With the employment of SARscape software, for each time span, velocity and displacements maps have been generated to obtain deformations time series to analyse and identify the motion due to volcanic activity. An important seismic event occurred during the investigated time period is the $M_w$ 7.0 Kumamoto earthquake happened on April 16, 2016, 60 km far from the caldera rim. Both in SAR and GPS time series was important to exclude the coseismic effect to estimate the correct trend movement due to the volcano activity.

In the displacement time series, three points in correspondence of GPS located within the caldera and few points in the post-caldera central cones have been examined for each time span. Analysing the displacements time series is necessary considered that deformations are affected by many factors as geodynamic, atmospheric effects, noise, type of images

processing and earthquakes further the volcanic activity and the characteristics of the sensor used for the acquisitions.

The final results show that only in case of short satellite revisiting time and lesser wavelength is possible to detect low intensity activities, but sometimes using SAR data with longer revisiting time and higher wavelength helps to obtain a better spatial information in vegetated area, as in the case of Aso caldera.

# Table of contents

Riassunto ..... i

Abstract ..... iii

Table of contents ..... v

Chapter 1: Introduction ..... 1

Chapter 2: Overview of the study area ..... 3

2.1 Geographic and geological setting ..... 3
2.2 Aso Volcano ..... 10
2.2.1 Eruptions and type of activity ..... 16
2.2.2 Kumamoto earthquake ..... 18

Chapter 3: Materials and methods ..... 23

3.1 Satellite RADAR remote sensing ..... 23
3.2 Synthetic aperture RADAR (SAR) remote sensing ..... 32
3.3 Satellite RADAR interferometry (InSAR) ..... 33
3.3.1 Interferometric processing ..... 37
3.4 Advanced interferometric techniques: SBAS and PS ..... 40
3.5 Satellites and sensors dataset ..... 44
3.6 GPS dataset ..... 49

Chapter 4: Results ..... 53

4.1 Velocity maps and displacement time series ..... 58
4.1.1 Palsar-1 dataset ..... 58
4.1.2 Sentinel-1 dataset ..... 62
4.1.3 Palsar-2 dataset ..... 68
4.2 Kumamoto earthquake ..... 71

Chapter 5: Discussion ..... 73

Chapter 6: Conclusions ..... 73

References ..... 83

# Chapter 1: Introduction

In the last twenty years the growing availability of satellite RADAR images has allowed to study ground deformations due to different phenomena as landslides (Wasowski and Bovenga, 2014; Xie et al., 2016; Tessari et al., 2017; Zhao et al., 2018), earthquakes (Moro et al., 2011; Merryman Boncori et al., 2015; Yu et al., 2018), subsidence (Tomàs et al., 2014, Yerro et al., 2014; Tosi et al., 2016; Fiaschi et al., 2017; Di Paola et al., 2018) and volcanic eruptions (Ayele et al., 2007; Biggs et al., 2009; Kobayashi et al., 2018) with the purpose to investigate characteristics, conditioning and triggering factors of these hazardous phenomena. RADAR remote sensing allows to explore wide areas during whatever atmospheric conditions and also during the night.

Observing the movement of the volcanic edifice can help to understand the behaviour before, during and after eruptions with the aim to predict them in the future and to assess the volcanic hazard. In fact, ground deformations in volcanic area, often reflect the deflate-inflate cycles of the magmatic chamber below the surface.

According to Dzurisin (2007), magma movements, landslides, faults or hydrothermal systems are different processes that can cause ground deformations at volcanoes; each pattern of displacement can be diagnostic of specific physical process, as dyke intrusion, cooling lava/pyroclastic flow or degassing activity and all of them can be detect and identify by *Interferometric Synthetic-Aperture RADAR* (InSAR) (Biggs and Pritchard, 2017).

The classic volcano deformation cycle is characterized by an uplift due to the inflation of the magma reservoir. When the eruption occurs, a rapid subsidence caused by the deflation takes place. However, many volcanoes do not show this behaviour: for instance, calderas. In general, calderas have long reposed periods highlighted by degassing activity or magma upwelling between very large eruptions. The unrest periods can be triggered also by external factors as big earthquakes, which can influence the hydrothermal systems too (Biggs and Pritchard, 2017). This is what occurs to Aso volcano. Aso stands out for its wide caldera (18 km x 25 km), whose surface is the expression of long-lived and complex magmatic system, that is characterized by a shallower hydrothermal system.

According to Nobile et al. (2017), eruptions are preceded by subsidence periods, that can last for several decades (Sudo et al., 2006).

The aim of this work was to compare various sensors (ALOS Palsar-1, Sentinel-1 and ALOS Palsar-2) characterized by different revisiting times and wavelengths and understand which one allows to better investigate Aso volcano activity.

Using InSAR technique is possible to quantify ground displacements, through the phase variation backscattered along the LOS (Line Of Sight) from a target on the terrain. The analysis, through *Differential Interferometric Synthetic Aperture Radar* (DInSAR) techniques, of a multi-temporal dataset of SAR images from different time spans and with different sensors, gives the opportunity to determine displacements time series. In particular, the employment of the *Small Baseline Subsets* (SBAS) advanced technique, improved by Berardino et al. (2002), allows to estimate and reduce the atmospheric effect and in addition to obtain a spatial displacement information with an accuracy of the order of the millimetres per year (Gomarasca, 2009).

The examined datasets consist in stack images from 2008 to 2011 for ALOS Palsar-1, from 2014 to 2018 for Sentinel-1 and from 2016 to 2018 for ALOS Palsar-2. The resultant SAR velocity and displacement maps were adapted with phase of 14 GPS time series through SARscape software, after the subtraction to them of the prevalent SE plate motion component.

In the Sentinel-1 time series, $M_w$ 7.0 Kumamoto earthquake occurs on April 16, 2016; to avoid overestimating in this period the ground displacements due to the magma reservoir, the GPS time series and the Sentinel-1 time span were split in two subsets: one before the event and one after.

Moreover, singular interferograms for the earthquake were generated with Palsar-2 and Sentinel-1, to help to understand further differences between the sensors.

In this work, the Aso caldera geological and volcanic features and the Kumamoto earthquake, that affected the area during the investigated period, are reported in chapter 2; after the description of the methods, SAR and GPS data and how they have been processed (chapter 3), the obtained results (chapter 4) are discussed in chapter 5, comparing the employment of the different sensors.

# Chapter 2: Overview of the study area

## 2.1 Geographic and geological setting

Japan is an archipelago composed of 6852 islands situated in the Pacific Ocean. The major islands are four and they cover the 97% of the Japan surface: Honshu, Hokkaido, Kyushu and Shikoku. (Fig. 1)


*Fig. 1: Geographic localization of Japan and its principal island. (bjchinesetranslation.com)*

Because of its localization over the Ring of Fire (Fig. 2), Japan is a land rich in volcanoes, where over 110 are active (Zhao et al., 2012). This particular area surrounds the Pacific Ocean and here occur, about 90% of the world's earthquakes and volcanic eruptions.

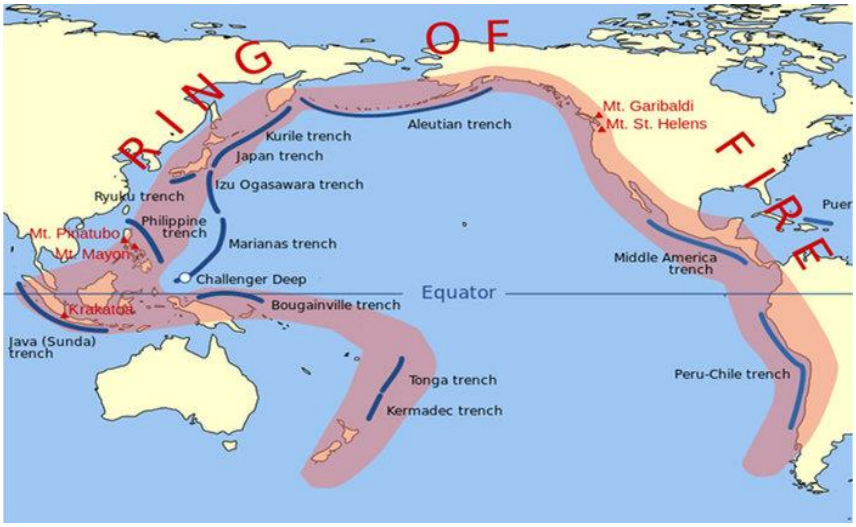


*Fig. 2: Localization of the Ring of Fire around the Pacific Plate. (education.abc.net.au)*

This wide seismic zone is the result of plate tectonics: the oceanic Pacific; Juan de Fuca, Cocos and Nazca plates interact with continental Australian, Philippine, North American, Caribbean and South American plates with different type of boundary as shown in Fig. 3.

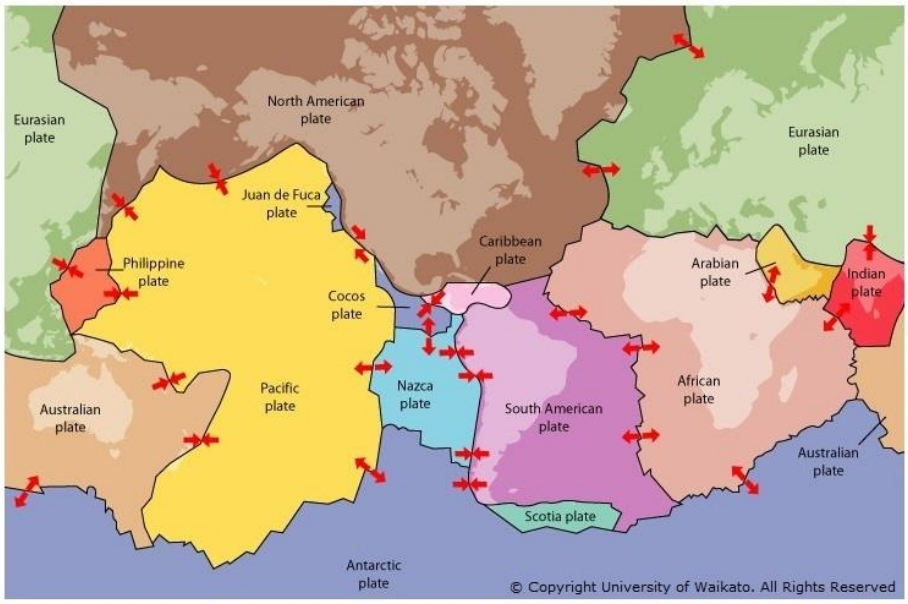


*Fig. 3: Tectonic plates and their boundary. (sciencelearn.org.nz)*

In general, all the Japanese volcanoes are situated over different volcanic arcs generated from the interaction of four plates: the Philippine Sea Plate, the Amurian Plate (part of

the Eurasian Plate), the Okhotsk Plate (perhaps a part of the North American Plate) and the Pacific Plate.

The Pacific Plate is moving underneath the Okhotsk Plate with a velocity of 8-9 cm/yr generating the Kuril Trench and the Kuril Arc with an oblique subduction directed north westward and with a perpendicular subduction towards west, the Japan Trench and the Northeast Japan Arc (or Honshu Arc). The same Pacific Plate subducts westward beneath of Philippine Sea Plate (PHS), causing the formation of Izu-Bonin Trench and Izu-Bonin Arc (Taira, 2001).

A normal westward convergence of PHS Plate underneath the Amurian Plate (velocity of 4-5 cm/yr), causes formation of the Ryukyu Trench and Ryukyu Arc. An oblique subduction directed north westward forms Nankai Trough and the Southwest Japan Arc (Fig. 4) that generates the westward motion of the Nankai forearc sliver (Fitch, 1972, Kagami, 1989), an area included between Nankai Trough and a right-lateral strike-slip fault (MTL, the Median Tectonic Line). (Fig. 4)

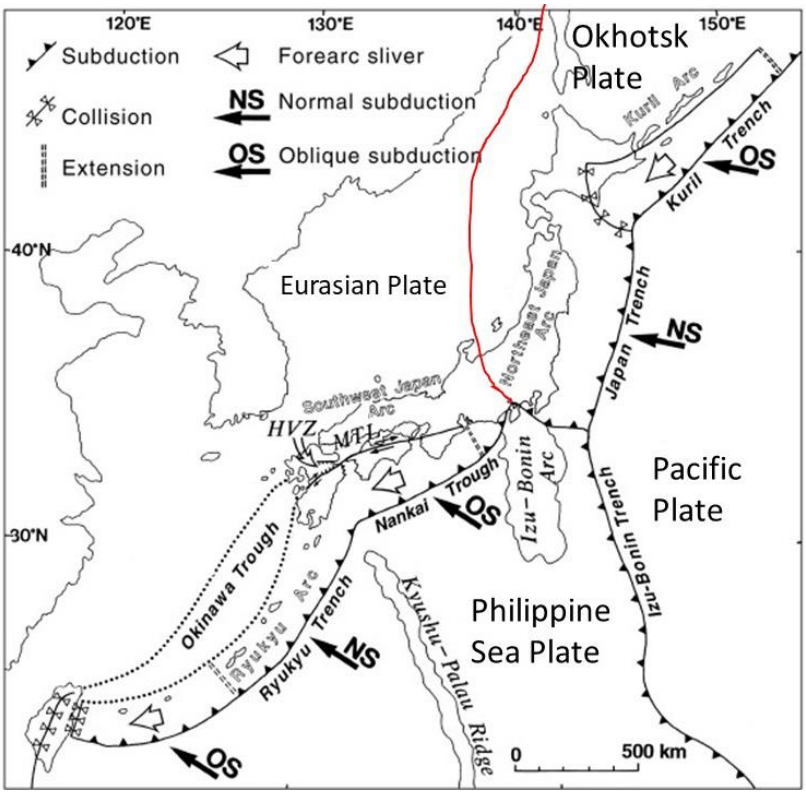


*Fig. 4: Map showing tectonic framework around the Japanese Islands.*
*Red line indicates the western convergent boundary between the Okhotsk and the Eurasian Plate.*
*The Amurian Plate is not represented in this figure.*
*[HVZ, Hohi volcanic zone; MTL, Median Tectonic Line.] (Kamata and Kodama 1999, modified)*

The Okinawa Trough is an intra-continental back-arc basin extending for 1200 km with NE-SW direction behind the Ryukyu Arc, from Kyushu to Taiwan, with a maximum depth of 2200 m in the southern part (Shinjo and Kato, 2000). It was generated in the early Pleistocene with formation of northeast-trending normal faults in the central and northern parts of the trough, because of weakness zone activated during previous tectonic phases (Sibuet et al., 1995).

The Median Tectonic Line (MTL) crosses Japan in a NE-SW direction and it extends over 900 km with a dip from 45°N to vertical (Loveless and Meade, 2010); it separates Mesozoic granites in the inner belt of southwestern Japan to the Palaeozoic sedimentary sequences in the outer belt. The maximum rate movement is about 0,6 cm/yr.

After a slowdown period, the resumption at ca. 6 Ma of the subduction of the PHS Plate (Mahony et al., 2011, Kamata and Kodama, 1999) and after a change in subduction direction of the PHS Plate from NNW to WNW (ca. 2 Ma) (Seno, 1985), the activation of the MTL right-lateral strike-slip fault was due to the sliding westward of the Nankai Sliver (Tsukuda, 1992), at around 0.8-0.5 Ma (Okada, 1980; Seno, 1985). (Fig. 5)

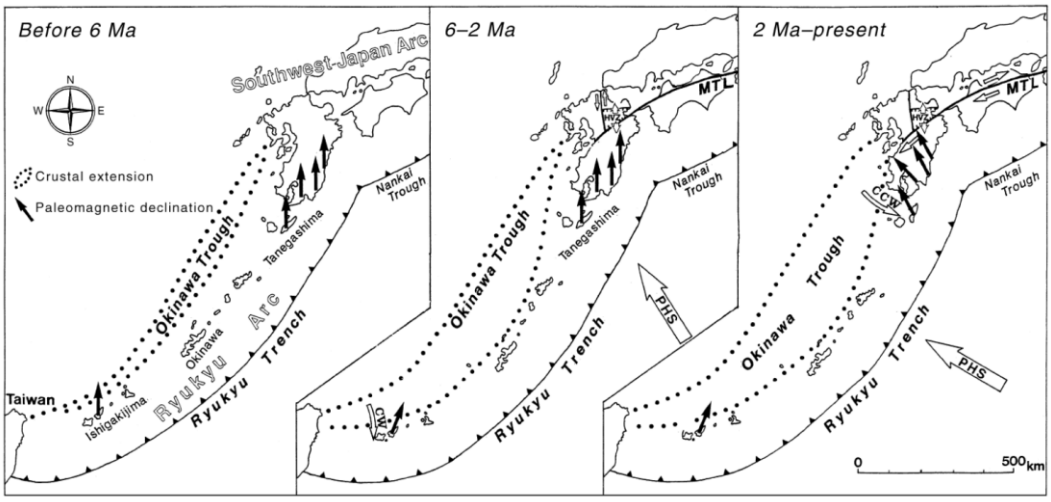


*Fig. 5: Tectonic development of the Southwest Japan and Ryukyu Arc from 6 Ma up to present. [PHS, Philippine Sea Plate, MTL, Median Tectonic Line] (Kamata and Kodama, 1999)*

This change in the plate motion has activated a counter-clockwise rotation of 30° with respect to north Kyushu and to Eurasia (discovered by paleomagnetic investigation) of the southern part of Kyushu Island (Fig. 6), in southwest Japan (Kodama, 1995). Before

this period, during the Late Paleogene, the MTL had a thrust movement. (Ichikawa, 1980).

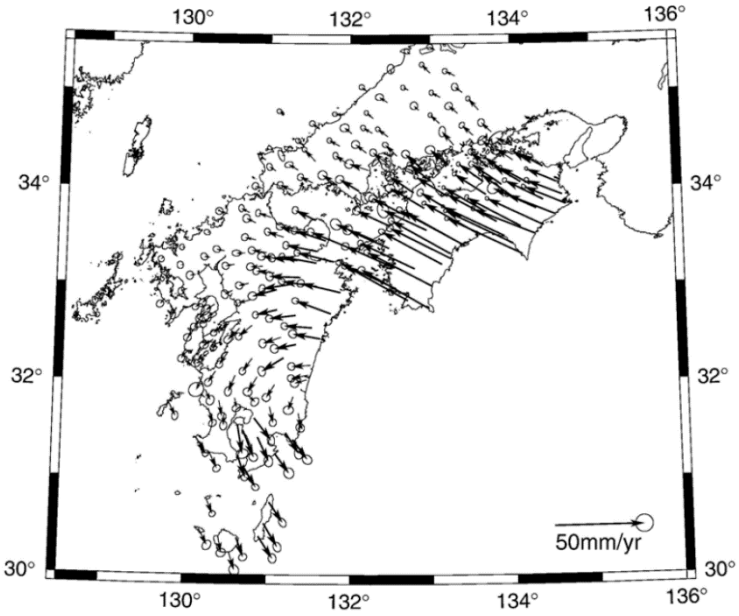


*Fig. 6: Present counter-clockwise rotation of southwest Japan relative to Amurian Plate. Arrows are representative of horizontal velocity. (Nishimura and Hashimoto 2006)*

The dextral trend of the MTL triggered the activation in Central Kyushu of the Hohi Volcanic Zone (HVZ), a northern extension of the Okinawa Trough, subsequently to the movement of the rhomboidal basin (Nankai Sliver). HVZ is a volcano-tectonic depression: that means it was established during a period of subsidence caused by normal fault in an early stage of rifting, simultaneously to the eruption. Activated at 2 Ma, it was characterized by an intensive volcanic activity. Now it has a NS extension constant rate of 0.1 cm/yr and its size is 70 km x 40 km (Kamata, 1989).

Until 2 Ma, the area was interested by andesitic lava flows related to EW fissure eruptions, connected to the formation of lava plateaus and intrusion of EW-oriented feeder dikes that confirms a NS extensional stress during the Plio-Pleistocene (Kamata, 1989)

Since 2 Ma until present day, volcanism has changed in composition from andesitic to dacitic with low eruption rates and with generation of monogenetic volcanoes. In

connection with the development of HVZ, volcanism was characterized by a diminishing of the lava flow eruptions and with an increase of pyroclastic flows (ignimbrites) of more than 10 $km^3$, forming calderas of almost 10 km in diameter, like the Aso caldera (Kamata and Komada, 1999).

The composition type of volcanism in Central Kyushu consists in calc-alkalic and high-alkali tholeiite series with a prevalent eruption of andesitic magma. In general, the volcanic rocks younger than 1.6 Ma, as in Aso, have a higher potassium content than older rocks (Kamata e Kodama, 1999) (Fig. 7).

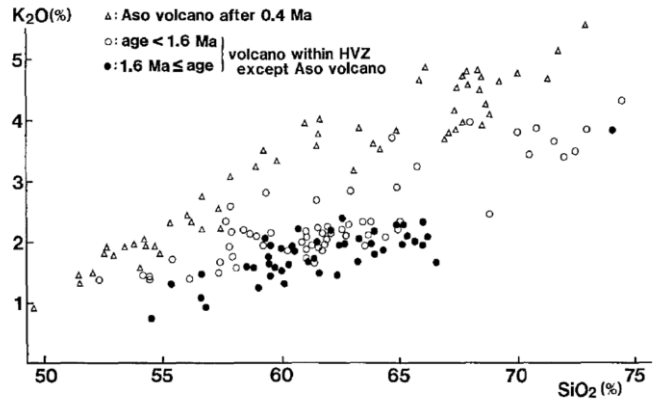


*Fig. 7: $K_2O$-$SiO_2$ diagram in wt%. Closed circles, volcanic rocks older than 1.6 Ma in HVZ. Open circles, volcanic rocks younger than 1.6 Ma in HVZ, except for ejecta of Aso volcano. Triangles, ejecta of Aso volcano. (Kamata, 1989)*

The reason of this potassium increase is probably due to lower degrees of partial melting of the mantle source in the early Quaternary period (Nakada & Kamata, 1991). This is related to the change in subducting direction of PHS Plate around 2 Ma, that has modified chemical and physical conditions of magma generation and evolution (Kamata, 1989, Kamata e Kodama, 1999).

Basaltic rocks in Central and North Kyushu are divided into three types: the Northwest Kyushu alkalic basalts, calc-alkalic magnesian basaltic andesite of the Yabakei-type and high-alumina basalt of the Kuju-type (Nakada and Kamata, 1991).

Another important geological structure is the Beppu-Shimabara graben, which has an extension from East to West of Kyushu Island and with a NS extensional stress. It is a zone characterized by subsidence and its southern margin is the Oita-Kumamoto Line

(OKTL), the western continuation of the MTL (Matsumoto, 2016, Kamata, 1998, Kusumoto, 2016). (Fig. 8)

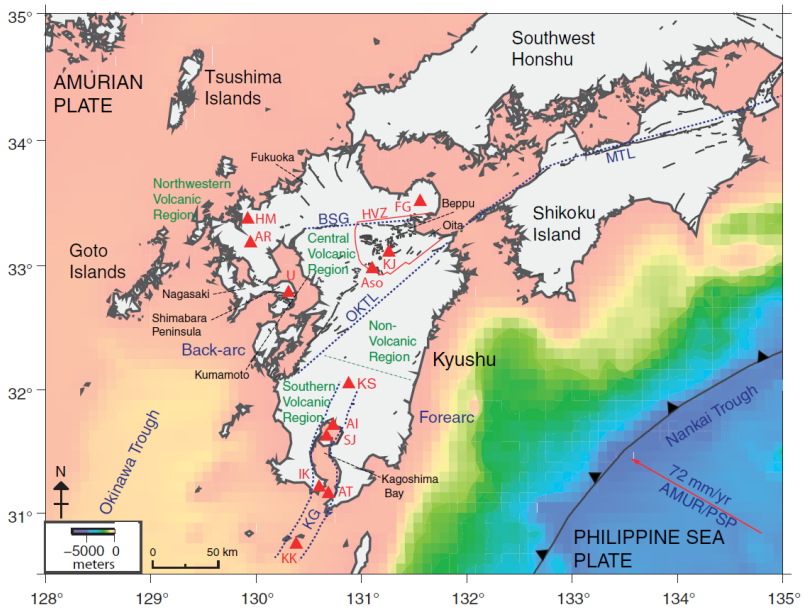


*Fig. 8: Detailed active tectonic setting of Kyushu. View of the Beppu-Shimabara graben (BSG) delimited by dotted blue lines. The graben boundary in the southern part is the Oita-Kumamoto Tectonic Line (OKTL). Red dotted line surrounds Hohi Volcanic Zone (HVZ). (Mahony et al., 2011)*

In the central part of Kyushu Island, a complex tectonic area, is situated the Aso volcano, whose activity is focus of our study. The OKTL is divided in two smaller faults by the Aso volcano: in the eastern part, the Imahata fault, in the western part, the Futagawa (slip rate: 0.9 mm/yr) and the Hinagu faults (slip rate: 0.5 mm/yr) (Baize, 2016). (Fig. 9)

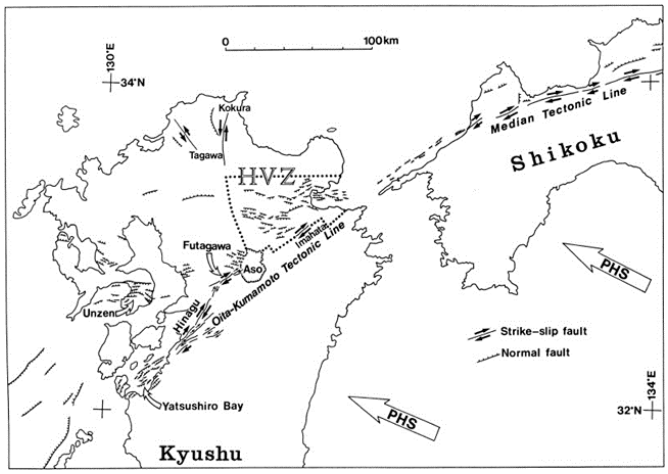


*Fig. 9: Aso volcano separates the Oita-Kumamoto Line (OKTL) in two smaller faults: Imahata fault at East and Futagawa and Hinagu fault at West. (Kamata, 1998)*

## 2.2 Aso Volcano

In Kyushu Island there are about twenty volcanoes and the most important are: Fukue-jima, Kirishima, Kuju, Sakurajima, Unzen and Aso, whose activity will be discussed in this work.

Aso-san is located in the central part of Kyushu Island along the southwestern Japan Island Arc (Kaneko et al., 2007), within of the Aso Kuju National Park in the Kumamoto Prefecture. Together with Yufu-Tsurumi and Kuju, Aso is a volcano younger than 0.1 Ma. All these volcanoes are aligned on a NE-SW volcanic front generated during the Quaternary and it is oblique to E-W volcanic front formed during the Pliocene (1.5 Ma). This chain is related to the change of subduction of PHS since 2 Ma (Kamata, 1998) and it is perpendicular to the current subduction direction (WNW) (Matsubara and Seno, 1980; Seno and Maruyama, 1984). (Fig. 10)

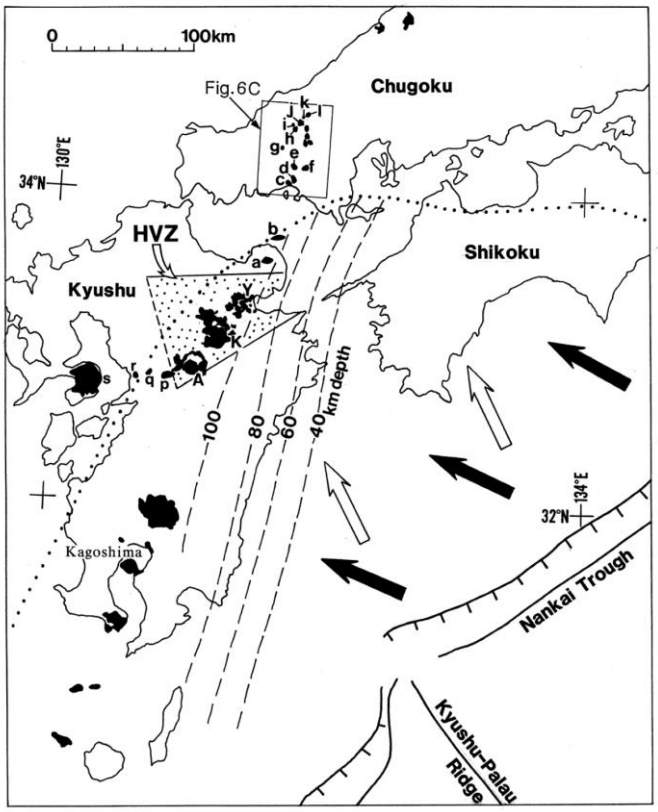


*Fig. 10: View of the Southwest Japan. Black arrows represent the present motion of the Philippine Sea Plate perpendicular to the EW volcanic front. White arrows indicate the past motion of the PHS Plate before 2 Ma according to Seno (1985). Dotted line is the contour line of deep-seismic plane on the underthrusting plate.*
*[A=Aso volcano]. (Kamata 1998)*

The western extension of the MTL, the Oita-Kumamoto Line (OKTL), crosses the volcano from East to West.

Aso is a monogenetic volcano situated within the southern part of the HVZ and its caldera is one of the largest in the world with main axes of 25 kilometres North-South and 18 kilometres East-West. Two caldera floors, Asodani Valley and Nangodani Valley, occupy respectively the northern and southern portions of the caldera interior and are situated to 500 m above sea level. Its rim can reach two times the height of the base of the caldera. (Fig. 11)

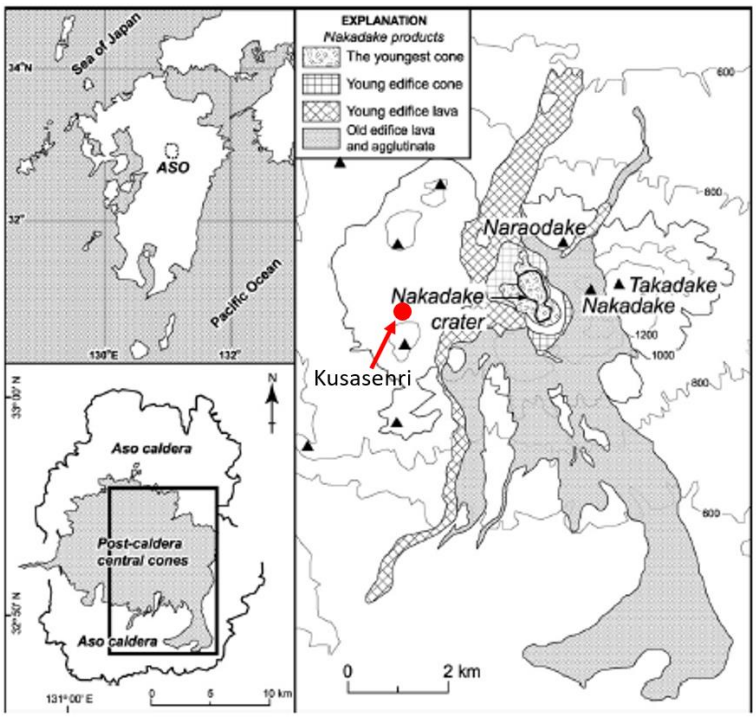


*Fig. 11: Localisation of the post-caldera central cones in Aso volcano and its main craters. (Ono and Watanabe, 1985, modified)*

The caldera was generated after four big cyclic explosive eruptions (Aso 1-4) with VEI = 6–7 (Kaneko et al 2015) from ca. 270 Ka to 90 Ka with a wide production of pyroclastic flows (Kamata, 1998). The word “cyclic”, for Fisher and Schmincke (1984), means a series of pulses without long time gaps between them.

These intensive events consist respectively in Aso-1 270,000 years ago, Aso-2 140,000 years ago, Aso-3 120,000 years ago and Aso-4 90,000 years ago. (Fig. 12)

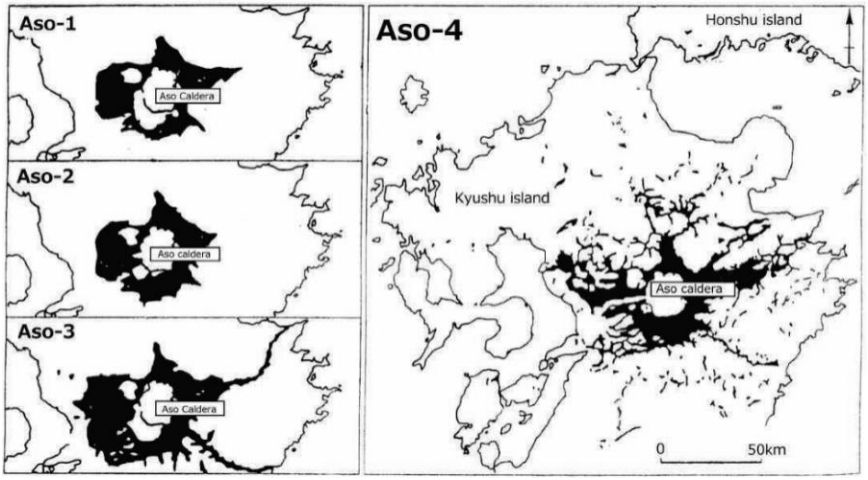


*Fig. 12: Distribution of Aso 1-4 pyroclastic flow deposits. (Ono and Watanabe, 1983)*

Aso-1 to Aso-3 cycles produced pyroxene rhyolite and pyroxene andesite, whereas Aso-4 mostly erupted hornblende rhyolite (Ono et al., 1977). The last eruption (Aso-4) was the most intensive with a production of more than 600 $km^3$ between airfall tephra and pyroclastic deposits and it could be divided in two subcycles characterized by a progression from silicic to mafic magma (Kaneko et al., 2007). The caldera was formed during this stage. The first subcycle is divided in three units where the most voluminous is made of >60 $km^3$ deposits. The second subcycle is also divided in three units, where the most abundant has a volume of ca. 10 $km^3$. Mafic scoriae produced by both subcycles have different whole-rock composition, for example in terms of $SiO_2$ (wt.%=50–54) and slightly different trends in CaO vs $SiO_2$, but the same compositional features of the phenocrysts. The chemical compositional variations are explained with two models for Kaneko et al. (2007): one suggests that there was a mafic magma replenishment between the two subcycles and the other one suggests, that mafic scoriae from the second subcycles are originated from the deeper part of the mafic layer of the pre-eruptive magma chamber and so they derived from a single zoned magma layer. The second model is anyway the easier to interpret. (Fig. 13)

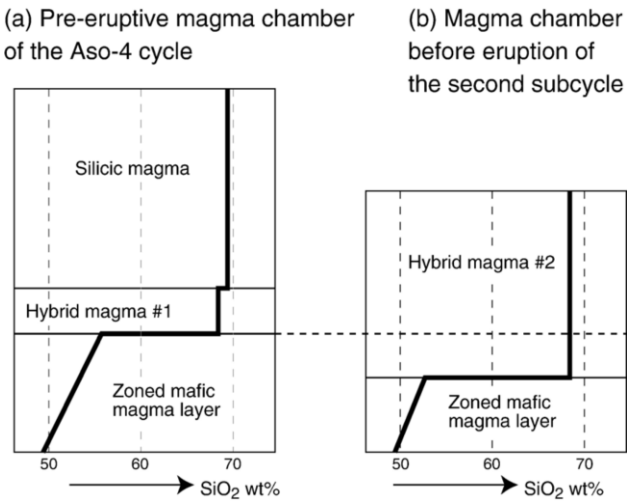


*Fig. 13: Schematic sketch of compositional structure of the Aso-4 magma chamber (not to length scale). Schematic vertical profile of whole-rock composition on $SiO_2$ is presented (bold line). (a) Pre-eruptive magma chamber. (b) Magma chamber before the eruption of the second subcycle. (Kaneko et al, 2007)*

According to Kaneko et al. (2007), the dimensions of the layered magmatic chamber before Aso-4 are estimated at 10 km in E-W direction and 20 km N-S at a depth of 3 km. The caldera was generated during fissure eruptions on the East and West of the magmatic chamber, that subsequently developed a collapse of the basement with 500 m subsidence, generating the caldera rim.

Today, thanks to tomographic data that highlight a low-velocity zone, the depth of a shallow magmatic chamber is estimated to be at 5-6 km below the inactive crater Kusasenri (Sudo and Kong, 2001; Sudo et al., 2006). It is a spherical chamber with a radius of 2-3 km, which has a volume around 100 $km^3$, but this alone couldn't have ejected more than 600 $km^3$ magma during Aso-4. Therefore, another deeper low-velocity layer to validate this value is needed: at depth between 10 and 24 km beneath the western part of the caldera such low velocity layer has been detected. It contains at most 15% melt or 30% aqueous fluid and its sized is estimated to be around 20 km x 15 km. A small magma sill at 15 km depth probably triggered a phreatomagmatic activity in 2003 (Abe et al., 2010; Unglert et al., 2011). (Fig. 14)

Shallow hydrothermal reservoirs located in the western part of Aso volcano at depths of 1–2,5 km have been revealed using magnetotelluric resistivity modeling (Asaue et al., 2006). These structures are confirmed by Huang et al. (2018), through ambient seismic noise tomography.

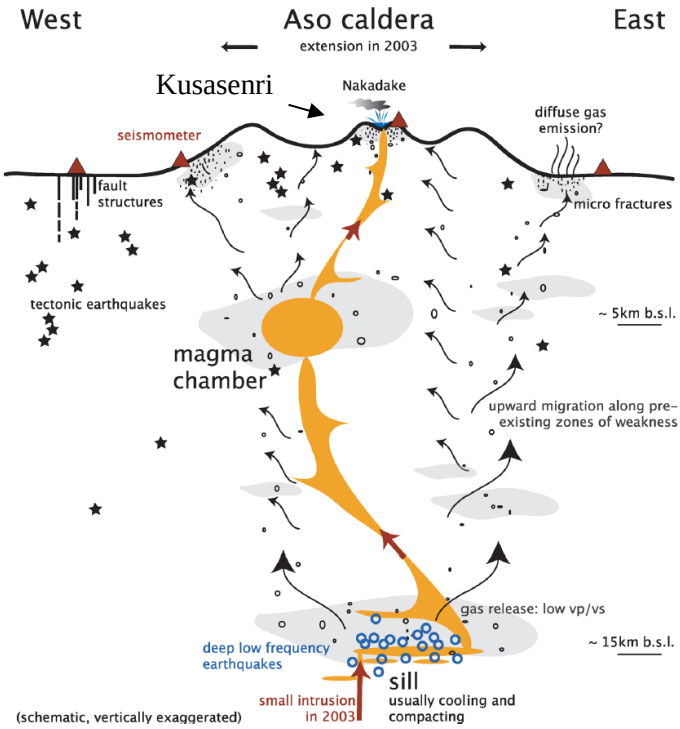


*Fig. 14 Distribution of the various magmatic chamber below the Aso Caldera. Black stars are tectonic earthquakes Sill and magma chamber inferred from previous studies (Sudo and Kong, 2001). (Unglert et al, 2011, modified)*

The Moho depth ranges from 32-39 km beneath the Caldera and surrounding area (Abe et al., 2010).

As highlighted in section 2.1, rocks in the HVZ are mainly calc-alkaline and high-alkali tholeiitic series. The rocks younger than 1.6 Ma generally have higher $K_20$ (Kamata, 1989).

Near Aso volcano, on the southwestern margin of the HVZ, volcanic activity has occurred for 2.2 Ma, but large-scale pyroclastic flows erupted only after 0.4 Ma. Post-caldera lava domes are characteristically high in alkalies. Older volcanic rocks in the inner walls of Aso caldera have a further higher $K_20$ content and were produced after 0.4 Ma. They are clearly separated from the common volcanic rocks in the HVZ and their origin maybe come from another different magma from HVZ (Kamata, 1989). The post-caldera lava dome is younger than 0.1 Ma. Inside there are more than 17 central cones, where the highest peak is Mt. Takadake (1592 m). (Fig. 15)

Nakadake (1506 m) is a young composite volcano of basaltic andesite to basalt (Ono and Watanabe, 1985). As shown in Fig. 15, it is divided in three parts: the old volcanic part (O), where the active cone rises about 900 m from the caldera floor, a young volcanic edifice (Y) and the youngest pyroclastic cone (A) within consists of seven N–S aligned craterlets. The wall of the active and northernmost craterlet is 140 m high (Ono et al., 1995).

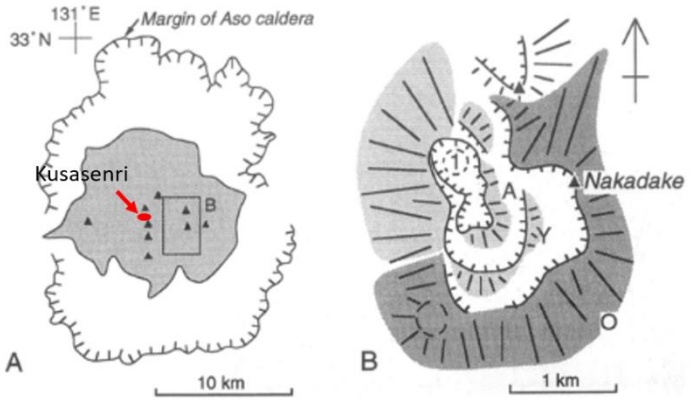


*Fig. 15: Sketch map around Naka-dake volcano, Aso caldera, Kyushu, Japan. (A) The margin of the caldera. (B) Nakadake volcano. 1=active, northernmost craterlet. (Ono et al, 1995, modified)*

Since 553 A.D., and mainly in the last 70 years, Nakadake is the most active crater. During its active periods it was characterized by strombolian, phreatic and phreatomagmatic eruption and a discharge of black and fine ash with ejection of hot scoriae or driblets. Occasional phreatic explosions eject coarse lithic blocks (Ohsawa et al., 2010, Miyabuchi and Terada, 2009). Ash ejected is formed by brittle fracturing of the solid glossy top part of the magma column (Ono et al., 1995).

Since 1995, the northernmost part is occupied by a hyperacid lake in its dormant and subsidence periods and intensive gas emission occurs through the lake water. After drying the lake, fumaroles appeared at the centre of the crater floor (Shinohara et al., 2018). It can reach a temperature up to 80°C during its activity periods (Miyabuchi et al., 2008). Its name is Yudamari and its size is 180 m and 210 m long NNW and WSW direction, respectively, with an estimated depth of 20 m; it has a pale blue-green colour, where the blue component is attributed to Rayleigh scattering of sunlight by very fine aqueous colloidal sulphur particles and the green component due to absorption of sunlight by

dissolved ferrous ions. The visibility of the green colour only is linked to activation of subaqueous fumaroles activity at the bottom of the lake, that increases colloidal sulphur or $Fe^{2+}$ concentration (Onda el al., 2003).

### 2.2.1 Eruptions and type of activity

As mentioned before, the most active crater is Nakadake and in the last 20 years it was characterized by a cyclic volcanic process: strombolian, phreatic and phreatomagmatic eruptions and emission of black ash (Miyabuchi et al., 2009; Cigolini et al., 2018).
As Ono et al. (1995) wrote, the most characteristic volcanic activity of Aso volcano is the fallout of black ash from fumaroles. The duration is ranges between few months and three years; the height of the smoke plume usually does not exceed 1000 m and the eruption products have juvenile basaltic andesite composition. The strombolian activity, in general, lasts less than ten days in total and the volume ejected is comparable with the ash from fumaroles. Phreatomagmatic eruptions are less frequent and their successive explosions form eruption columns that rarely exceed 2000 m of height. These occur because of heavy precipitation and it is due to the presence of the lake in non-active periods, which suggests the huge role of the groundwater (<400 m deep, with seasonal changes; Miyabuchi et al., 2008), that cools down the top part of the magma column and rarely causes explosive eruptions.
The main eruptions between 1989 and 2016 are reported in Tab. 1 (Nobile et al., 2017)

| Start date | End date | VEI | Type | Eruptive vent |
|---|---|---|---|---|
| 1989 Apr 5 | 1991 Feb 9 | 2 | Phreatomagmatic eruptions | Nakadake |
| 1992 Apr 23 | 1993 Jun (?) | 2 | Mud eruptions | Nakadake |
| 1994 May 2 | 1995 Nov (?) | 2 | Mud eruptions | Nakadake |
| 1997 | 2002 | | Hot crater lake | Nakadake |
| 2003 Jul 10 | 2003 Jul 14 | 1 | Ash fall | Nakadake |
| 2004 Jan 14 | 2004 Jan 14 | 1 | Ash fall | Nakadake |
| 2005 Apr 14 | 2005 Aug (?) | 1 | Phreatomagmatic eruptions | Nakadake |
| 2008 Feb 17 | 2008 Feb 17 | 1 | Phreatomagmatic eruption | Nakadake |
| 2009 Feb 4 | 2009 Feb 4 | 1 | Tephra fall | Nakadake |
| 2009 Nov 2 | 2010 Jul | | Seismic swarm | |
| 2011 May 15 | 2011 Jun 9 | 1 | Tephra fall | Nakadake |
| 2014 Jan 13 | 2014 Feb 19 | 1 | Phreatomagmatic eruption | Nakadake |
| 2014 Aug 30 | 2015 May 1 | 2 | Strombolian eruption | Nakadake |
| 2015 Sep 3 | 2015 Oct 23 | 2 | Phreatomagmatic eruption | Nakadake |
| 2016 Mar 4 | 2016 Apr 16 | 1 | Ash falls | Nakadake |

*Tab. 1: List of Aso volcano eruptions from 1989 to 2016 according to JMA (Japan Meteorological Agency). (Nobile et al 2017)*

The eruptions, that are interesting for our study, are included in the period from 2007 to 2018 at the Nakadake crater. From 2008 to February 2009, the area surrounding the crater was affected by several tephra fall events (Cigolini et al., 2018).

In mid-July 2010, volcanic unrest was characterized by a high amplitude seismic swarm (Nobile et al., 2017). In this period, hot fumaroles were actively degassing at the southern rim of the crater lake.

The most important activity occurred at Aso volcano started in April 2011, when small mud eruptions and ashfall emissions occurred at the Nakadake crater. The end of this interval (June 2011) was determined by a diminishing activity and by the increase of the hot water coverage in the crater from 60% to 80% of its full volume (Wunderman, 2012). After June 9, 2011, no activity was registered until January 2014, when a small phreatomagmatic eruption started and then went on until February 2014.

The first absence of hot water in the crater since February 1993 has been noted in July 2014.

One of the strongest eruptions occurred during this period is the strombolian activity from November 2014 to May 2015. This eruption has been preceded since late August 2014 by a large number of isolated volcanic tremors. The eruption occurred from two active vents at Nakadake, producing explosions of incandescent material onto the crater rims. Ashfall was registered in the surrounding Kumamoto (W), Oita (NE), and Miyazaki (SE) prefectures for a quantity of 1,500,000 tons from the beginning of the activity until the first days of February 2015 From November to February, continuous GNSS measurement showed slight extension of the baseline across Kusasenri, where a magma chamber is considered to be present in deeper parts. Since March the extension has slowed down (Japan Meteorological Agency). After this event, a series of larger explosions happened from August to October 23, 2015 with pyroclastic flows and ejecta that impacted the immediate area around the crater. Before its disappearance at the end of June 2015, an increase in the lake temperature up to 80° C has been noted at the beginning of June (Japan Meteorological Agency, 2015). On December 7, 2015 milk-white plumes rose as high as 700 m above the crater rim. The presence of the lake was observed again after this very small explosion.

From February 2016 to April 2016 a new eruption has been registered at Nakadake with emission of lapilli and ashfall. In May, hot water reappeared and covered 70% of the crater (Japan Meteorological Agency, 2016).
The results of continuous GNSS measurement showed a slight extension of the baseline across Kusasenri, from around July 2016 until mid-November 2016. During this period, an explosion occurred on October 8, 2016 and was moved up by a series of larger tremors, after the longest period of thermal rest.
No eruptions happened in 2017 and in 2018. Since May 2018, the hot green water has covered 100% of the crater volume. The activity has continued with only high fumarolic emissions (Japan Meteorological Agency, 2017).

### *2.2.2 Kumamoto earthquake*

Kumamoto is a city in western central Kyushu Island and it is the capital of the Kumamoto Prefecture. It is situated in the southwestern boundary of the Beppu-Shimabara graben at ca. 40 km Southwest of Aso volcano.
An earthquake sequence occurred here in 2016 and caused large crustal deformations.
This event has reactivated numerous pre-existing faults in the shallow crust, as the Futagawa and the Hinagu fault and allows also to study new faults, as Idenokuchi fault, parallel to the Futawaga one.
The earthquake caused damage due to strong ground motions, surface ruptures, and subsequent landslides: more than 100 people were killed (Fire and Disaster Management Agency, 2016).
Although in the past Southwest Japan has experimented stronger seismic activity, recently, it has been noticed that it has a less intense seismicity than in Northeast Japan, due to a gradual strain accumulation during an interseismic period (Kato et al., 2016). (Fig. 16)

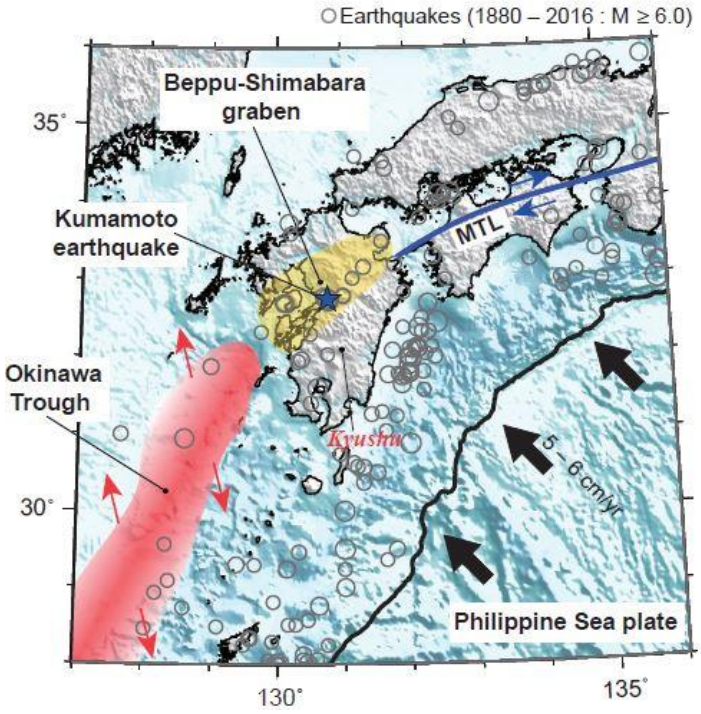


*Fig. 16: Seismotectonic setting of Southwest Japan, including the Kyushu area. Blue line denotes the Median Tectonic Line (MTL) and its right-lateral strike slip. The yellow shaded area indicates Beppu-Shimabara graben and the red shaded area represents Okinawa Trough and its extensional system. Grey circles show earthquake epicentres from 1880 to 2016 shallower than 60 km and with magnitudes ≥6.0. Blue star symbolizes the epicentre of the 2016 Kumamoto earthquake. (Kato et al., 2016)*

Elastic energy was released during the intensive seismicity happened in the western part of Aso volcano and its accumulation is due to the convergence between the different plates beneath Japan.

The mainshock happened at 10 km depth on April 16, 2016 at 01:25 JST (Japan Standard Time) with $M_w$ 7.0 ($M_{JMA}$ 7.3), which followed the $M_w$ 6.2 ($M_{JMA}$ 6.5) earthquake at 21:26 JST on April 14, 2016 at 9 km depth and the $M_w$ 6.0 ($M_{JMA}$ 6.4) on April 15, 2016, 00:03:48 JST at depth of 8 km.

The mainshock epicentre was located above Futagawa Fault (ENE-WSW oriented). Instead, the two foreshocks had the epicentre above the northernmost part of Hinagu Fault (SWS-NEN oriented). Together, the length of their surface ruptures reaches around 30 km along the previously mapped ca.100-km-long active fault with a further extension toward west (Kumahara et al., 2016). (Fig. 17)

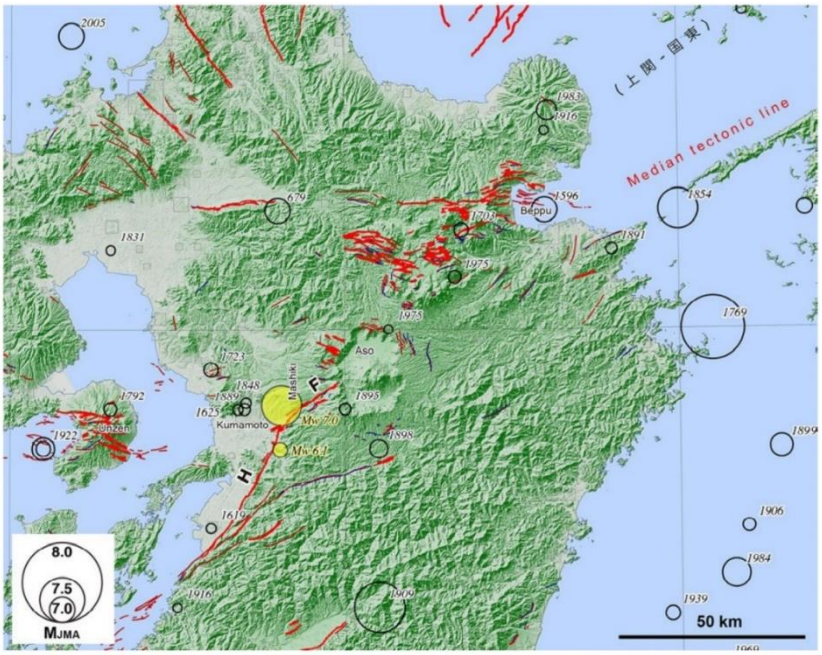


*Fig. 17: Representation of the Quaternary faults (Nakata and Imaizumi eds., 2002) and earthquakes Usami, 1996) in the Northern Kyushu. Red lines denote Quaternary faults. Black circles indicate the seismic intensity of earthquakes since 1700.Yellow circles symbolize the 2016 earthquake epicentres along Futugawa (F) and Hinagu (H) Faults. (Okumura, 2016)*

The right-lateral strike slip faulting style of the three events conforms to the regional deformation patterns on geological timescale.

According to Kato et al. (2016), the sequence deformation could be explained by three fault segments: A1, A2, B. (Fig. 18)

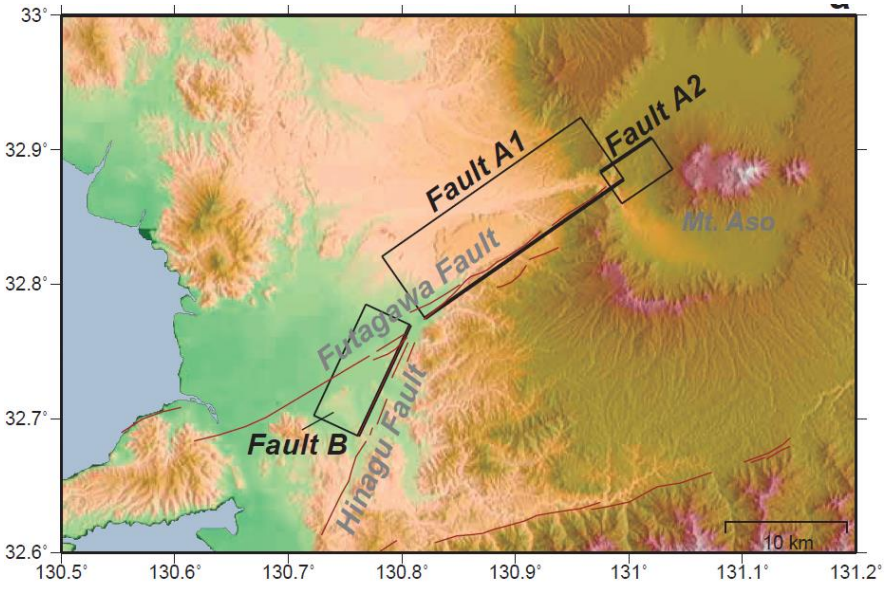


*Fig. 18: Source fault model of the Mw 6.2 foreshock and the Mw 7.0. Black rectangles denote the three fault planes of A1, A2, B projected ono the surface. (Kato et al., 2016)*

Fault A1 is the longest segment (ca. 20 km) of Futagawa fault and the nearest to Aso volcano. By geodetic inversion, Kato et al. (2016) showed that a normal component dipping 60° to the northwest needed to be summed to the right-lateral movement (Baize, 2016). Through its motion during the mainshock, A1 released most of the elastic energy, after a slip estimated to be around 2 m for Hao et al. (2017) and Okumura (2016); according to Kato et al. (2016), it was estimated a slip of 4.1 m including the mainshock plus the 2 foreshocks. The vertical slip due to the normal movement is up to 0.5 m south-side-up, but up to 0.2 m north-side-up (Okumura, 2016).

Fault B is situated along the northernmost segment of the Hinagu Fault and it showed mainly a right-lateral strike slip of 3 m, value, which includes also the coseismic slip of the 6.0 $M_w$ and 6.2 $M_w$ earthquakes (estimated to be 1.1 m in total for both).

Fault A2 (5 km long according to Okumura, 2016) is located within the caldera of Aso volcano and it is characterized by a right-lateral strike slip. Its dip is toward Southeast, opposite to A1 and B fault. Consequently, it could be considered a conjugate fault of A1. The average slip for mainshock and foreshocks is estimated to be ca. 3.8 m. (Fig. 19)

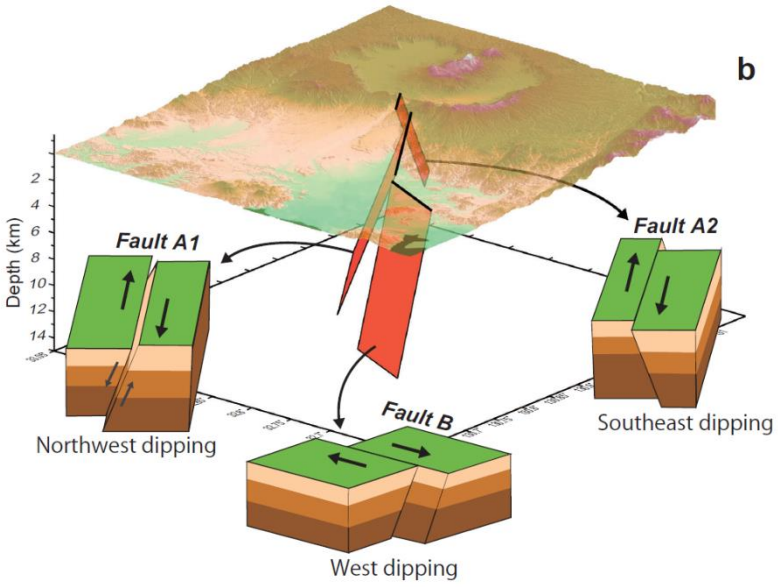


*Fig. 19: 3D perspective view of fig. 17. Fault A2 is located inside the caldera of Aso volcano and it has a different dip from A1 and B fault. (Kato el al., 2016)*

The mainshock triggered 230 seismic swarm events until May 8, 2016 also to 50-100 km away from the epicentre (Aizawa et al 2017), small explosive eruptions in Aso volcano until April 30, 2016 and a seismic tremor that decreased after May 15, 2016 (Japan Meteorological Agency). In fact, Aso volcano expanded volumetrically, mainly in the EW direction, but the summit subsided by ca. 20 cm after the mainshock. The increase of temperature in the caldera could have prevented the generation of aftershock at both eastern edge of the fault A1 e A2, because high temperatures (>300-350°C) inhibit the nucleation of earthquakes (Blanpied et al., 1995). This is considered the limit depth for shallow crustal ones. The presence of magma beneath the Aso volcano blocked the propagation of coseismic rupturing north eastward. (Lin et al., 2016)

In the past, earthquakes larger than $M_w$ 7.0 in this area were inferred only by paleoseismological excavations and by an estimated recurrence interval of 3600–11,000 years long the Hinagu fault and of 8100–26,000 years along the Futagawa fault (NIAIST, 2007).

# Chapter 3: Materials and methods

## 3.1 Satellite RADAR remote sensing

Remote sensing consists of different techniques that studies objects or phenomena from a certain distance through emitted, reflected and transmitted electromagnetic radiation from the terrestrial surface. Many acquisition modes exist and each one can detect in a different portion of the Electromagnetic Spectrum (EM). (Fig. 20)

Sensors are active or passive instruments: the first type is characteristic of RADAR and LIDAR and consists in the acquisition of backscattered radiations emitted from the system itself. The intensity received depends on the structural features and roughness of the examined surface and on the wavelength of the incident energy signal. The second type records the reflected electromagnetic energy coming from the Sun or emitted by Earth. Typical passive sensors are photo cameras, scanners, video cameras (Gomarasca, 2009).

Sensors are installed in platforms as satellites or airborne.

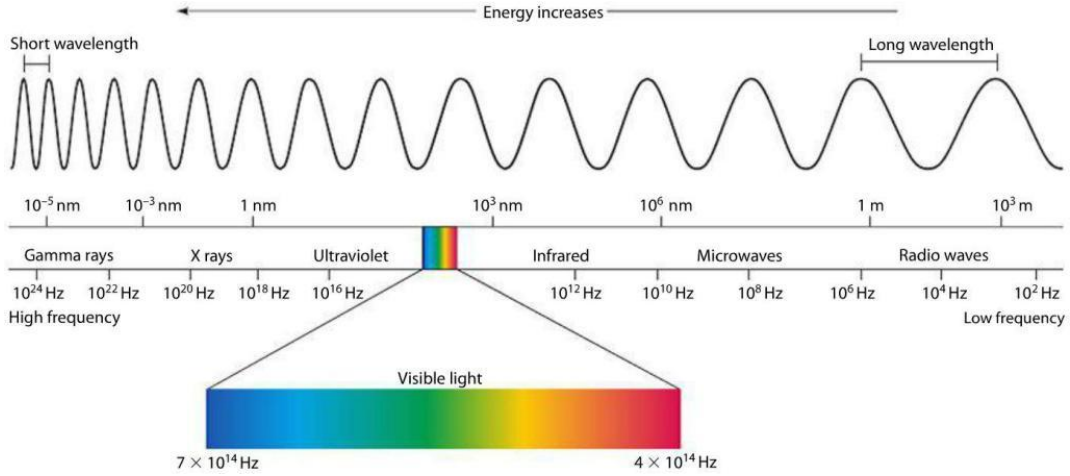


*Fig. 20: The electromagnetic spectrum. (www.miniphysics.com)*

This work is focused on the use of RADAR (Radio Detection And Ranging) active sensors, and in particular Synthetic Aperture RADAR (SAR), mounted on satellites.

A RADAR system is composed by a transmitter, a receiver, an antenna and a recording device. In case of monostatic RADAR, transmitter and receiver are built in the same antenna, instead, in case of bi-static, they are in two separated antennae. The system is based on the principle of echo: the wave returns to the transmitting antenna with a certain intensity due to investigated objects on the surface. RADAR employs electromagnetic waves in the range of microwaves (1 mm–1 m) sent periodically on observed scene by a transmitter in short impulses duration, with high power, a certain wavelength (λ) and a bandwidth. The antenna allows the propagation in the space of the wave and to pick up the echo energy return from the target. The receiver filters and amplifies the backscattered signal coming from the obstacles, then stored in analogic or digital form by recording device and subsequently converted in bidimensional images.

The roughness size of the objects is important, and it can reflect in different way the incident wave: in case of smooth surface, there is a specular reflection and the magnitude of energy coming back to receiver, is very low. Typical examples are streets and water that appear black in images. It can happen also when the size of the target is smaller than the signal wavelength. Otherwise, if the surface is rough, the energy is backscattered in all directions and a wide quantity comes back to the receiver making bright that object in the image (Sabins 1997). (Fig. 21)

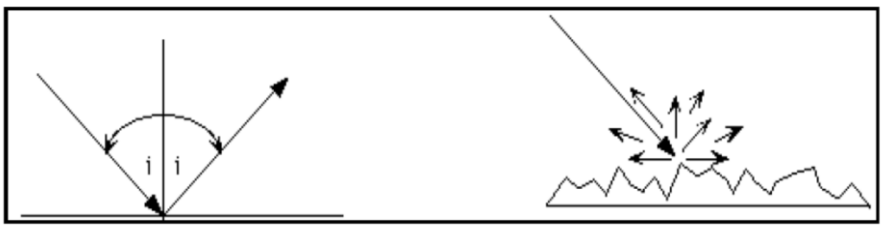


*Fig. 21: On the left specular reflection on a smooth surface; on the right backscattered reflection on a roughness surface. (SAR-Guidebook, Sarmap 2009)*

Thus, the backscattered signal depends on the characteristics of the RADAR dispositive (frequency, polarisation, acquisition geometry) and on the target features (geometry, roughness, moisture content, dielectric properties, electric resistivity).

Therefore, from the recorded backscattered signals, information about the distance sensor-target can be also obtained, known the propagation speed of the electromagnetic waves (c=300.000 km/s) and calculating the temporal delay from sent signal to received echo. If transmitted impulses do not encounter any obstacles, they are not backscattered signals and consequently no information is stored. Images generated are made up of pixels, whose value is proportional to the power of the signal reflected from the corresponding cell on the ground to the antenna (Gomarasca 2009).

RADAR sensors use different bands characterized by various wavelengths and frequency, that can investigate different obstacles. The purpose of their application is to measure and monitor the ground deformations on the terrestrial surface.

The most employed bands are (ESA, Gomarasca 2009):

- X-band: λ = 2.7 – 5.2 cm; f = 5.75 – 10.90 GHz
- C-band: λ = 5.2 – 7.1 cm; f = 4.20 – 5.75 GHz
- L-band: λ = 19.3 – 76.9 cm; f = 0.390 – 1.550 GHz

According to Fujiwara et al., (2016), the advantages of RADAR sensors are:

- to investigate the terrestrial surface also in bad atmospheric conditions (e.g. with clouds, storms or fog) and during the night;
- to penetrate more or less the vegetation based on the frequency and wavelength chosen. L-band penetrates more than X-band because of its low frequency and long wavelength (Iisaka, 1998) (Fig. 22), but it also depends on the water content, that changes dielectric properties;
- to examine wide areas with repeated observations over a short time period, related to the revisiting time;

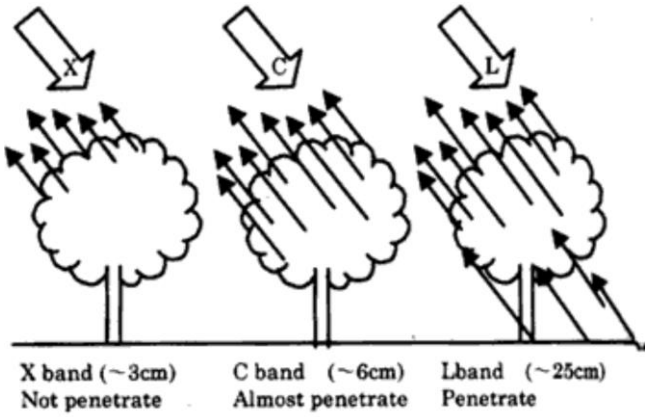


*Fig. 22: Wavelength of the signal and ability to penetrate vegetation. (geospatialworld.net)*

The obtained remote sensing information require a ground validation to be reliable. Another limit of RADAR are the radiometric and geometric distortions in the acquired images.

Satellites equipped with RADAR sensors fly along sun-synchronous and near-polar orbit at an altitude of 500-800 km, in order that they can acquired over the same position at the same time every repeat cycle, with a swath width around 100 km.

They move above two trajectories: one ascending, that acquires data from South to North and one descending, from North to South as shown in Fig. 23.

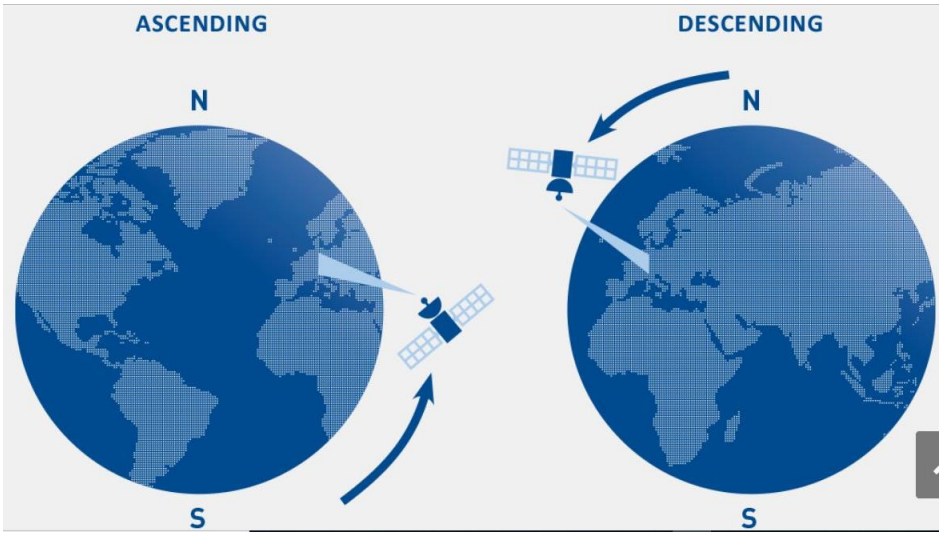


*Fig. 23: Ascending orbit on the left and descending orbit on the right. (site.tre-altamira.com)*

RADAR antenna illuminates an area in the surface called *antenna illumination footprint*, included in the *swath* area. The direction of flight path is known as *azimuth*, instead the perpendicular direction on the ground is called *range*. The antenna-target distance is called *slant range* or LOS (*Line Of Sight*), along which the backscattered signal is detected, and its projection on the terrestrial surface is known as *ground range* (Fig. 24).

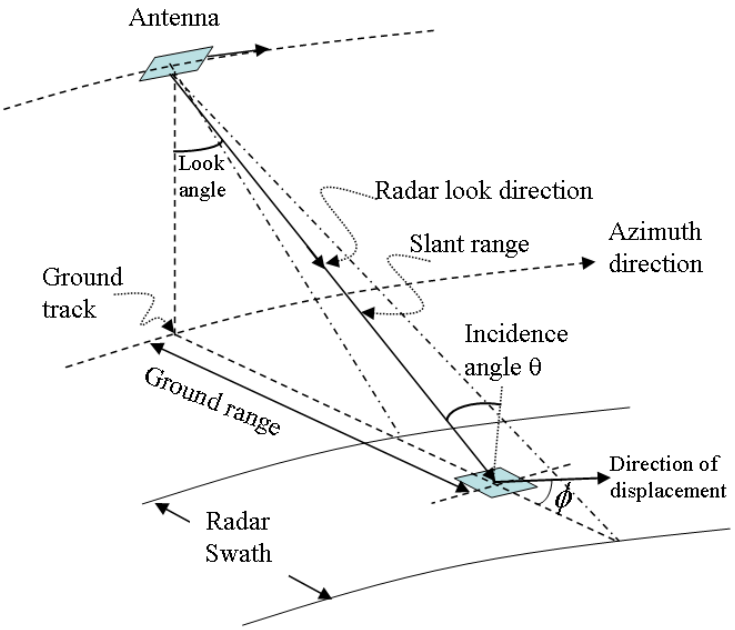


*Fig. 24: Acquisition geometry of RADAR satellites. (Zhou et al., 2009)*

The RADAR acquisition closer to the *nadir* is *near range*, instead the further is *far range*. In general, the acquisition geometry is right-looking type tilted between 30° and 50°. If satellites acquire symmetrically to the left and to the right of the *nadir*, it is not possible distinguish between two different points with same distance from the sensor, because the same incident wave-front illuminates both points at the same time with consequently same backscattered signal received from the antenna. This angle (θ) comprised between the *nadir* and the incident ray along *slant range* is called *off-nadir*. Higher is the angle inclination, wider is the ground exploration area and better resolution the image has, but at the same time the backscattered signal intensity decreases. (Gomarasca 2009).

Two type of spatial resolution exist: along *range* and along *azimuth* (Fig. 25).

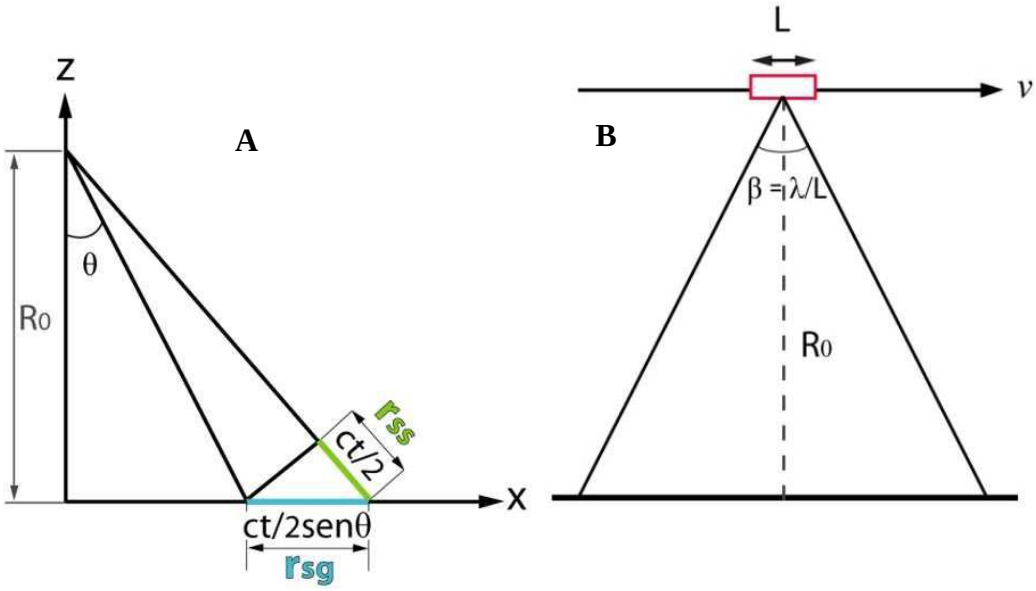


*Fig. 25: A) slant and ground range resolution; B) azimuth resolution for a Real Aperture RADAR (RAR) system. (Pasa, 2014)*

The first one is taken along *slant range* and considering c as the speed of light in vacuum (3 x $10^8$ m\s) and τ as the duration of the transmitted impulse, the spatial resolution ($r_{ss}$) (Fig. 25, A) is:

$$r_{ss} = \frac{c \cdot \tau}{2}$$

The *ground range* projection ($r_{sg}$) (Fig. 25, A) is:

$$r_{sg} = \frac{c \cdot \tau}{2\ sin\theta}$$

where θ is the incident RADAR angle.

Along the *azimuth*, spatial resolution ($r_{sa}$) (Fig. 25, B) is the smallest size up to which the sensor can clearly detect two different points along the flight direction. It is inversely proportional to the dimension of the antenna (L) sending the signals and proportional to the radar-target distance ($R_0$), to the radar beam width (β) and to the radar wavelength (λ) (Gomarasca 2009):

$$r_{sa} = \beta \cdot R_0 = \frac{\lambda \cdot h}{L \cdot cos\theta} \quad \text{where} \quad R_0 = \frac{h}{\cos\theta} \quad \text{and} \quad \beta = \frac{\lambda}{L}$$

From this last formula emerges that a Real Aperture RADAR (RAR) sensor built above satellite platform, has spatial resolution limited by antenna width (L): if its dimension increases, the resolution decreases. Thus, to have resolution in the range of meters, an antenna long almost one kilometre is needed.

For RAR systems, only the amplitude of each echo return is measured and processed (SAR-Guidebook, Sarmap 2009).

To avoid the resolution problem, above satellites are built Synthetic Aperture RADAR (SAR) systems, discuss in paragraph 3.2.

Besides the well-known advantages, RADAR images are subject to some distortions, mainly geometrical distortions and textural distortions (*speckle*) (Gomarasca, 2009).

The *slant range* acquisition mode generates geometric distortions due to the angle (θ) of side-looking viewing and to the variable topography.

If instead the topography is flat and the sensor altitude is known, it is possible to correct the geometric deformations.

Typical RADAR geometric distortions are *foreshortening, layover e shadowing* and they vary differently from *near* to *far range:* the first images result more compressed than the second ones. (Fig. 26)

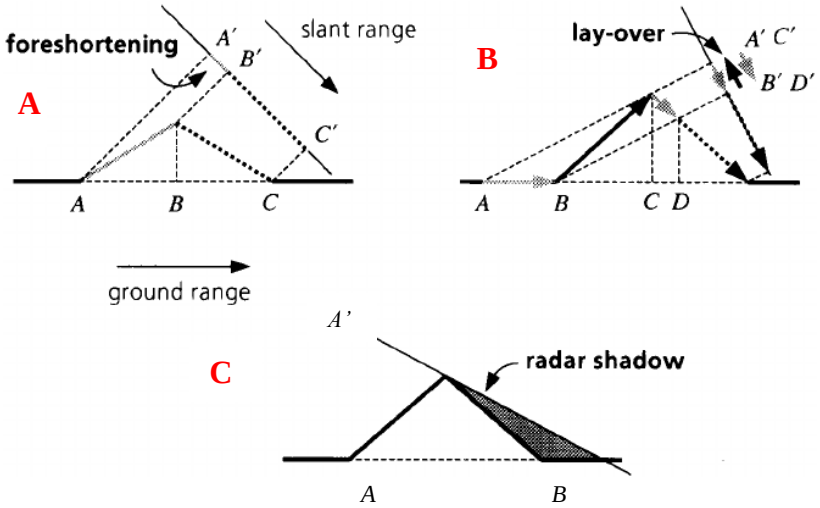


*Fig. 26: Different type of geometric distortions. (Bamler, 2000, modified)*

*Foreshortening* is related to the acquisition perspective that causes a compression of the target. It happened when an acute angle is generated between the RADAR beam and the normal component to the surface (Fig. 26, A). This phenomenon is stronger, if the slope (AB) of the topography is perpendicular to the sensor-target connection (AA'). It can be identified by brighter areas in the image (A'B'), because the backscattered signal to the sensor is compressed from numerous points along the slope in fewer pixel. Quite the opposite happens to the other slope (BC), that appears darker in image (B'C'), because of a signal distribution of fewer points stretched in many pixel.

*Layover* (Fig. 26, B) is the extreme case of the *foreshortening* and it happens when the RADAR signal reaches the mountain top (C) before its base (B), specifically when the terrain slope exceeds the incident angle of the signal. In images (C'D'), this effect is identified with bright areas and it is due to the inversion between the top and the base mountain, after the projection from ground range to slant range (Bamler, 2000).

*Shadowing* (Fig. 26, C) is the area that can be found behind steep mountains (AA') at shallow incidence angles (Bamler, 2000). Resultant images appear dark, because no information is detected.

The only geometric distortion that can be corrected is the *foreshortening* by a Digital Elevation Model (DEM), instead the other two can only be identified but not corrected.

During the acquisition, another problem can be highlighted: the radiometric distortions. They influence the quantity of backscattered energy received by the sensor (Triglia, 2010).

A typical of a phenomenon that provokes amplification or a damping in the backscattered signal is *speckle*: noise, that disturbs the image quality and makes the interpretation difficult. This is produced by destructive or constructive interferences between backscattered electromagnetic waves coming back to the sensor from different targets in the same pixel. The effect created in the image is a texture with light and dark points randomly distributed (Fig. 27). One way to reduce the *speckle* is filtering the image, but this implies a reduction in spatial resolution.

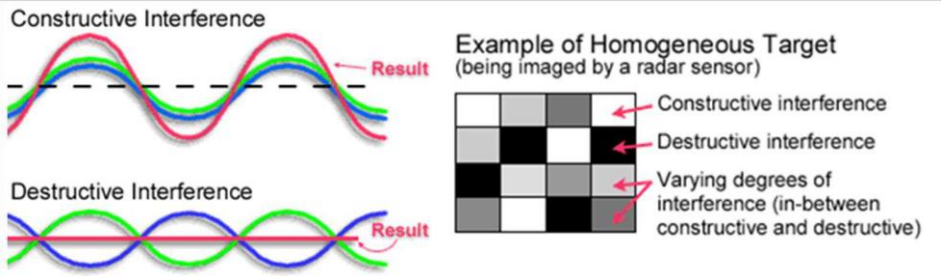


*Fig. 27: Speckle effect due to constructive and destructive interferences. (Canadian Centre of Remote Sensing)*

In general, RADAR sensors are built with polarised signal to better investigate the terrestrial surface and its targets. The polarisation is one of the fundamental properties of the electromagnetic waves and it corresponds to the oscillation direction of the electric field during the wave propagation. To define its direction, H letter is used for horizontal polarisation and V for the vertical one.

In Fig. 28, different combinations of signals polarisation are shown: for instance, if a sensor is polarised with HH type both transmitted and backscattered signal are horizontal polarised. Similar is the VV polarisation, with both signal vertical polarised. With HV and VH, transmitted signal is horizontal polarised and the backscattered one is vertical polarised and vice-versa, respectively.

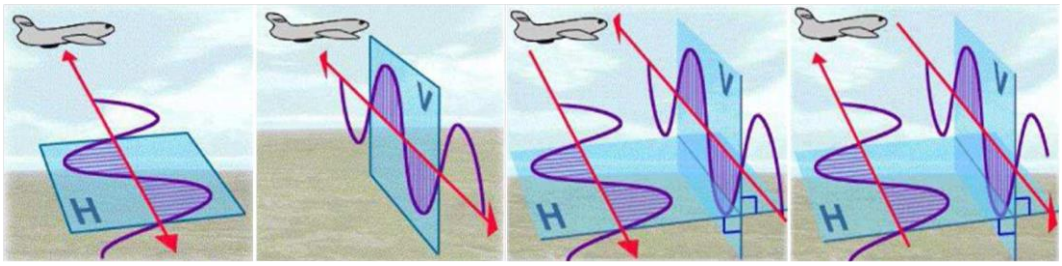


*Fig. 28: Different type of polarisation: HH, VV, HV and VH. (www.envisat.esa.int)*

The like-polarisation (HH or VV) occurs when the polarisations of the transmitted and backscattered signal are the same type. The physical process responsible for that is quasi-specular surface reflection as calm water that appears black.

The cross-polarisation (HV or VH) occurs when transmitted signal is perpendicular to the backscattered one. The sensor usually records a weaker signal, associated with different reflections due to surface roughness (SAR-Guidebook, Sarmap 2009). Depending on the different type of polarisation used, the electromagnetic waves interact differently with targets (Richards, 2009).

## 3.2 Synthetic aperture RADAR (SAR) remote sensing

As discuss in section 3.1, to increase spatial resolution along the *azimuth*, the size of the RADAR antenna should be increase, but this could create some difficulties to carry it on board of satellites. Another way to improve the resolution should be the reduction of the signal wavelength, but this could diminish also the ability to penetrate clouds, that is one of the advantages of the RADAR.

The solution to overcome these limits and problems is represented by the *Synthetic Aperture RADAR* (SAR). The first idea of SAR system was created in 1951 by Carl Wiley from Goodyear Aircraft Corporation. The convenience of this acquisition mode is the observation of the same target from different point of view, for the whole time span in which object is inside the beam amplitude, using a small antenna. The physical principle on which it is based the system, is the Doppler effect, that allows to use a small antenna as it were a bigger one having high resolution (Gomarasca, 2009).

A RAR antenna stores different radar return echoes from the same target during the platform motion, to the aim of rebuild the echo that would be recorded from a SAR antenna ($L_s$), longer that the real antenna (D). It is possible to define the width of synthetic antenna considering an orbiting satellite along its flight path with velocity v, a real antenna (D) and a time interval, in which pulses are transmitted from different part of the sensor. While the platform is moving above the orbit, electromagnetic waves hit the target. (Fig. 29)

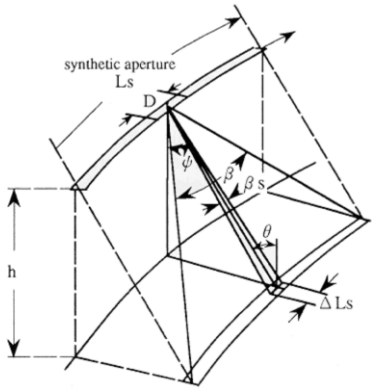


D : real aperture
$\beta$ : real beam width
$\beta$ s : synthetic beam width
h : height
$\Delta$ Ls : azimuth resolution
$\psi$ : off nadir angle

*Fig. 29: Relation between RAR and SAR. (SAR-Guidebook, Sarmap 2009)*

The interval of time T = $t_1$ - $t_0$ the satellite covers a distance of:

$$L_s = v \cdot T = \frac{h \cdot \lambda}{D} = \beta_s$$

where $\beta_s$ is the synthetic beam width.

The SAR resolution along *azimuth* is:

$$r_{az} = \frac{h \cdot \lambda}{2 \cdot L_s} = \frac{h \cdot \lambda}{2 \cdot \frac{\lambda}{D} \cdot h} = \frac{D}{2}$$

In conclusion, the resolution on the ground along *azimuth* is half of the real size of the antenna. The spatial resolution along the *range* is the same of the RAR system ($r_{ss} = (c \cdot \tau)/2$) and its relative *ground range* projection ($r_{sr}$).

To obtain a spatial resolution along *range* of a few meters, the pulse should have a duration in the order of $10^{-7}$-$10^{-8}$ s, but the energy required to transmit the signal would be too high, reducing consequently the signal-noise ratio and also the radiometric resolution.

The results obtained by SAR acquisition are data containing information about amplitude and phase, as discussed in section 3.5.

## 3.3 Satellite RADAR interferometry (InSAR)

The SAR interferometry (InSAR), consists in the study of the phase differences between two SAR images, obtained recording backscattered signals from the same scene observed in subsequent time (Ferretti et al., 2007).

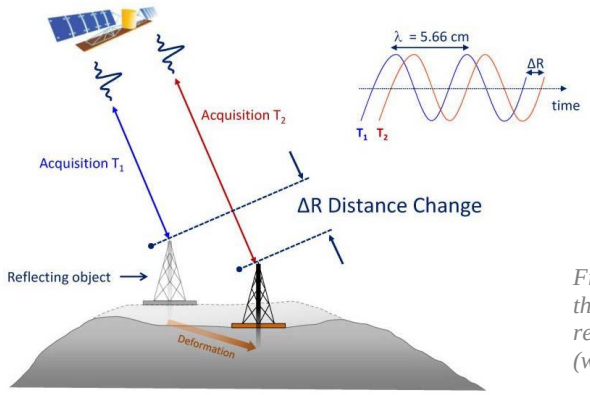


*Fig. 30: Relation between ground displacement and the phase variation of the signal. The wavelength reported is related to ERS sensor. (www.treuropa.com)*

The aim of InSAR is to monitor the crustal deformation caused by earthquakes, subsidence, uplift or landslides (Fig. 30). The displacement is detected by the sensor as a variation in the backscattered signal phase due to the change in sensor-target distance: RADAR sensor measures the signal return period and its intensity coming from the terrestrial surface.

Due to the combination of a SAR images called *master* and *slave*, the resultant image is an *interferogram*, a map that, through fringes, reproduces phase difference between two acquisitions and that allows to determine the variations of sensor-target distance (Fig. 31). In particular, *master* is acquired before than the *slave* and it is used as reference. An interferometric fringe (usually in a coloured scale from blue to red), measured along the LOS, corresponds to a target displacement equal to half of the signal wavelength in meters.

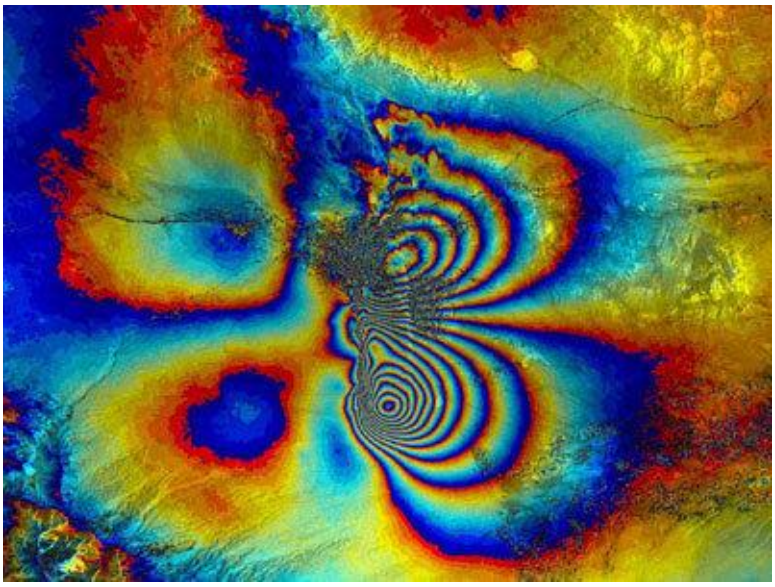

*Fig. 31: Interferogram of the 2003 Bam earthquake generated with Envisat data (C-Band). Many concentric fringes are visible. In this case one fringe=28mm (www.esa.int, Courtesy of A. Monti Guarnieri, POLIMI)*

Two acquisition modes exist for InSAR: *single pass* and *dual pass.* The first one consists in the employment of two antennae built above the satellite that acquire simultaneously the same area. In the second one, images are acquired in two different time period with a unique antenna. Thus, *dual pass* is based on the revisiting time of the satellite over the same area. In this case, the orbits over which the satellite flights, can be subject to variations due to normal baseline (Bn), the distance between the satellite during the first acquisition and the LOS (*Line Of Sight*) of the second acquisition and the temporal baseline, the interval of days between the two different acquisitions. Critical baseline is the value over which two different acquisitions do not give any information about the phase difference. B is the distance between the two antennae, situated in the plane perpendicularly to the flight path. (Fig. 32)

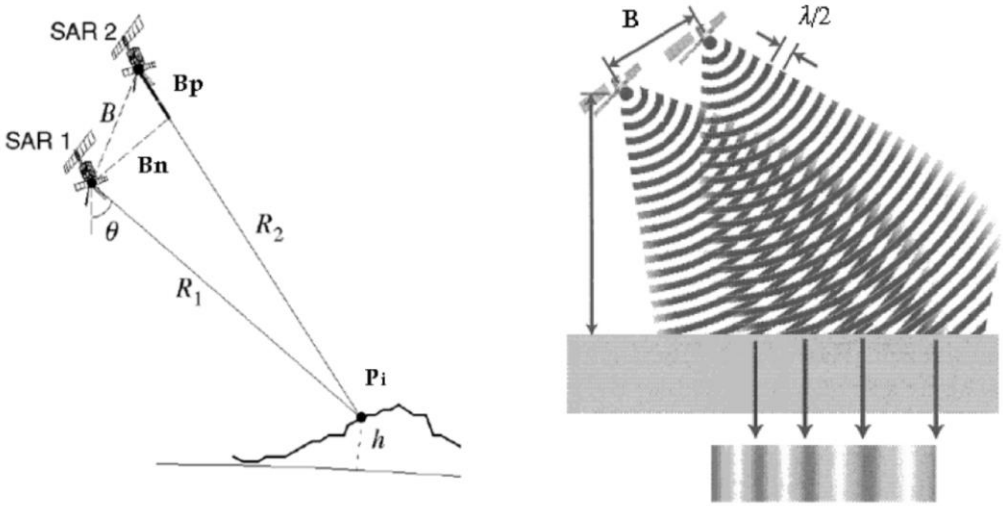


*Fig. 32: To the left the geometry of the dual pass SAR acquisition mode. To the right the generation of fringes caused by the phase difference generated by normal baseline. (Luzi, 2010, modified from Shang-Ho, 2008)*

The phase difference (Δφ) between two consecutive acquisitions depends on the path difference (Δr) and it is proportional to the phase cycle in radians (2π) and the wavelength (λ). Δr is considered as 2r because is related to round trip of the signal. (Fig. 30)

$$\Delta\varphi = \frac{2\pi\Delta r}{\lambda} = \frac{4\pi r}{\lambda}$$ (Gomarasca, 2009)

Due to the periodical sinusoidal signal, the displacements (Δr) corresponding to an integer multiple of wavelength are not distinguishable, because they produce the same difference of phase.

Considering the maximum difference phase (2π) an interferometric fringe measured a displacement of (Fig. 31):

$$r = \frac{\Delta\varphi\lambda}{4\pi} = \frac{2\pi\lambda}{4\pi} = \frac{\lambda}{2}$$

Then, the displacements should be projected along the real direction to obtain the true ground deformations.

The interferometric phase is the amount of different contributions:

$$\Phi_{int} = \Phi_{geom} + \Phi_{topo} + \Phi_{displ} + \Phi_{atm} + \Phi_{noise}$$

Where $\Phi_{geom}$ is the contribute related to the different geometry acquisition; $\Phi_{topo}$ is the topographic contribute at the first acquisition; $\Phi_{displ}$ is the ground displacement; $\Phi_{atm}$ corresponds to the atmospheric variations between two acquisitions: radar wavelength

can penetrate the atmosphere, but there are some cases and conditions, in which the troposphere can create a phase delay of waves, influencing the interferometric phase accuracy. This is caused by temperature, air pressure, composition and the presence of moisture; $\Phi_{noise}$ is the contribute connected to the radiometric distortion, phase unwrapping errors or orbital errors.

To obtain the object displacement some corrections are needed: the topography can be improved with a *reflattening* of the image through a DEM (Digital Elevation Model), the atmosphere and the noise can be reduced with some filters and the geometric contribute of the baseline (normal and temporal) need to be corrected to decrease the decorrelation and to increase coherence between two SAR images.

The coherence is a parameter that expresses how much constant reflectivity is maintained by a target, in two images acquired in two different time period. (Bamler and Just, 1993). Coherence is defined with a value between 0 (completely different backscatterers between two images) and 1 (same backscatterers) and depends on normal and temporal decorrelation, on the presence of vegetation that seasonally change and on atmospheric condition (moisture, pressure, temperature).

### *3.3.1 Interferometric processing*

The program used to process SAR data in this work is SARscape, that is developed by Sarmap SA, located in Switzerland.

After the acquisition and before the interferometric processing, SAR images have to be *focused*, *multilooked* and filtered (to eliminate speckle). *Multilooking* and *speckle* filtering are included in algorithm for the data analysis, while the focusing needs to be previously done.

In the raw data, the backscattered energy coming from a punctual target, is diffused in different pixels along *range* and *azimut*h directions. The aim of the *focusing* is to attribute this energy inside to a unique pixel associated to the target. Focalised images have .slc extension (*Single Look Complex*) and contain amplitude and phase information extracted from a complex matrix.

*Multilooking:* the initial *azimuth* and *range* resolution are modified and make comparable with ground objects converting pixels from rectangular to square. The extension obtained is .pwr (*Power*). A first filtering reduces noise in this step.

*Coregistration:* it overlaps two SAR images covering the same area, acquired with same geometry and same acquisition mode, giving the same reference frame. In this step rotation and shifting are reduced using a reference image (*master*), which is overlapped by a second one (*slave*).

This allows to calculate in the next steps, the phase difference between two pixels referred to the same resolution cell in the *Interferogram Generation.* The value obtained considers all the contributes already described (acquisition geometry, the topography, the atmosphere and ground displacements), but some of them are reduced in the next steps.

In the step *Flattering*, the topography is subtracted to the interferometric phase through a DEM. The resultant _dint file extension has a diminishing of the fringes frequency depending on the DEM resolution. Residual fringes are related to the remaining contributes.

To first create a coherence maps, where the stable areas are highlight with white pixels and variable areas are shown in black pixels and then to reduce noise in the interferogram phase, the step *Adaptative Filter and Coherence Generation* is used. Three types of filter can be adopted (Tessari, 2014):

- *Adaptative*, where the coherence is used to calculate the size of filtering window with the purpose of preserving the smallest interferometric fringes;
- *Boxcar*, where the local fringes are used to optimize band-pass filter with the aim of preserving the smallest fringes;
- *Goldstein* is a filter for noisy frequencies with variable width. Changing some of the parameters it is possible filtering much more areas with low coherence than those with high coherence.

The file generates have _fint extension.

Every series of coloured fringes (from blue to red in a scale coloured) in the interferogram phase represent a $2\pi$ completed cycle, variable between $-\pi$ and $+\pi$. Because of the periodical nature of the sinusoidal signal, if displacement ($\Delta r$) generate a phase difference of more than a multiple integer of the wavelengths, a phase ambiguity occurs and it is not

possible to estimate its value. The *Phase Unwrapping* step allows to calculate the absolute phase value, which is converted in altitude or displacement (in meters) though the use processing algorithm. (Fig. 33)

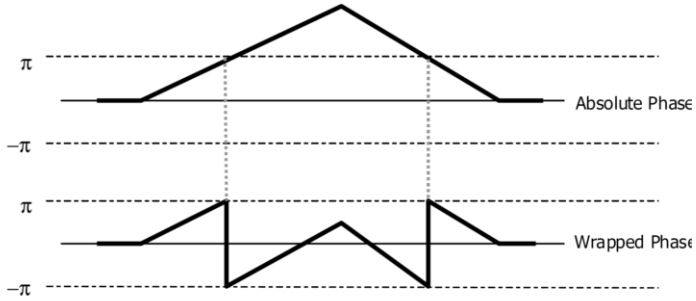


*Fig. 33: The wrapped phase (down) in the range -π, π that need to be correct and the unwrapped phase (up). (SAR-Guidebook, Sarmap, 2009)*

The common algorithms used to solve phase ambiguities in presence of many areas with low coherence are *Minimum Cost Flow, Delaunay MCF* and *Region Growing.*

The first two consider different grids and numbers of pixels covering the image. In particular, *Delaunay MCF* use triangulation that doesn't cover all the pixels, minimizing phase jumps. Only the points with high coherence are unwrapped. The third limits phase ambiguities through a growing process, that first unwraps adjacent points with low coherence and then, progressively, the others with more coherence. Other two parameters need to be evaluated during this step: the *Unwrapping Decomposition Level* and the *Unwrapping Coherence Threshold.* The first is intended to multilook and undersample the data. The interferogram is unwrapped at lower resolution and reconstructed back at the original resolution. *Decomposition Level* can help to reduce unwrapping errors as in case of distributed low coherence areas, but if the phase image is characterized by very frequent displacement variation (dense fringe distribution), this option must be set with care or avoided, because these fringes can be lost. (Sarscape User Guide, Sarmap, 2014)

The second is the threshold below which pixels are not unwrapped. In this step, _upha file are created.

The orbital correction is necessary to convert in the last step, the unwrapped phase in altitude and displacement maps. It is developed in *Refinement and Reflattening* step and using *GCP (Ground Control Points)* is possible to remove the presence of phase ramps. GCPs (or GPS) can be generated in *slant range* or already geocoded and they should be considered as stable points and set far from areas where the displacement is very variable. File _reflat.dint, _reflat.fint and _reflat.upha are generated.
In the step *Phase to Displacement (or Height) Conversion and Geocoding*, phase is converted in displacement or altitude map and geocoded using a reference coordinate system as WGS84 or UTM. The result is _reflat_disp file.
If both the descending and ascending geometries are available, it is possible to project the _reflat_disp file from *slant* to *ground range* through the *Displacement Decomposition from Asc and Desc Geometries* to obtain vertical and EW horizontal displacements.
NS displacements are not detectable by the SAR, because satellites orbit along this direction.

## 3.4 Advanced interferometric techniques: SBAS and PS

Differential Interferometric techniques (DInSAR, Differential Interferometric Synthetic Aperture RADAR) use a multi-temporal series of SAR images to describe ground deformations and their evolution during time (Tessari, 2014). Through this method, it is possible to investigate target deformations in different images, acquisition geometry and climatic condition. The two most important techniques are *Persistent Scatterers* (PS) (Ferretti et al., 2001; Hooper et al., 2004) and *Small Baseline Subset* (SBAS) (Berardino et al., 2002, 2004, CNR-IREA di Napoli). Both identify displacements with an accuracy of the order of the millimetres per year in range resolution of 15-20 m (Gomarasca, 2009) and used a minimum of 20 images of the same area, detected from the same sensor and with similar acquisition geometry.
One of the advantages of these techniques is the possibility to estimate the atmospheric contribute in the single differential interferogram, through a stack of SAR images

distributed in the time, with the purpose to remove it. It is important to diminish this contribution, because atmosphere can create fringes that can be confused with fringes produced by displacement. Also topography generates fringes that need to be reduced and they are caused by the refractive index variable with the altitude in the troposphere. Associated to the time series, also spatial and temporal filter should be used to reduce decorrelation factor, as vegetation or the same atmosphere already mentioned.

PS combines a *master* with more *slaves* as possible. The numbers of interferograms generated is limited. This technique detects deformations through small and punctual objects with backscattered properties and stable in time. SBAS uses wide obstacles and open space and it is slightly accurate, because of its areal investigation.

In tab. 2, the major differences between SBAS and PS are listed.

| PS | SBAS |
|---|---|
| Analyse independent, uncorrelated motions | Monitor at best spatially correlated motions |
| Expect pixel-wise continuous time series | Capable of handling time series with temporal holes |
| Time interval between two acquisitions limited by displacement rate | Time interval between two acquisitions limited by temporal decorrelation |
| Very accurate on PSs | Slightly less accurate |
| Linear displacements favoured | Larger variety of parametric models possible. Non-parametric modelling possible |

*Tab. 2: Comparison between PS and SBAS characteristics. (Pasquali et al., 2014)*

In this work, the technique used to process SAR images is the SBAS. It can better estimate displacements in Aso volcano, through the combination between all the SAR images, after setting a temporal and normal baseline.

Below, are described the different steps in SBAS technique. (Fig. 34)

*Connections Graph*

With the SAR images already focalised, as more connections as possible are created. Two parameters should be set: *normal* and *temporal baseline* to combine images pairs. The wider range chosen by operator for both baselines is, the more connections are possible to obtain, but with the risk to have many images with low coherence and low coverage.

*Normal baseline* depends on the acquisition geometry and the distance between orbits during the different acquisitions. *Temporal baseline* depends on the satellite revisiting time. Two graphics are created: the *time-position plot,* which shows the connections between a reference image called *supermaster* and the others in relation with acquisition time and a *time-baseline plot* that correlates acquisition time with *normal baseline.*
Parameter: *Allow Disconnected Block* is often set as *True,* to avoid the loss of some connections and consequently of information.

*Interferogram Generation*
In this step _dint, _fint and _upha are created. Parameters as *Unwrapping Method Type (Delaunay MCF), Unwrapping Decomposition Level, Unwrapping Coherence Threshold* and *Filtering Method (Goldstein*), already discuss in section 3.3.1, should be set. Values below the threshold are not considered. The lower the threshold is, the more data are available, but also more noise can be present generating not reliable data.

*First Editing*
Through *SBAS Edit Connection Graph* is possible to eliminate from _upha, pairs with problems as low covering or phase jumps. In our case, this wasn't necessary, because *Min valid interferogram*s%, *Min valid images%* and *Min valid acquisitions%* were set in *First* and *Second Inversion*. This allows to preserve images and interferograms, in which the same pixel is present in a certain percentage in them and to avoid the *SBAS Edit Connection Graph* step, maintaining all the connections and consequently more information and covering.

*Refinement and Reflattening*
Orbital parameters are corrected through GCPs located in areas with low displacements velocities or null.

*First Inversion*
A first velocity and displacements estimation are obtained after that a second *phase unwrapping* occurs. Here is possible to choose the *Min valid interferogram*s%.

If *Allow Disconnected Block* was used in *Connection Graph,* also here it should be set as *True.*

*Second Editing*

In this step other pairs and connections can be modified, if images present low covering or problems.

*Second Inversion*

The atmosphere contribution is reduced through filters. Displacements and altitude are estimated one more time, after that *Min valid interferograms%* and *Min valid acquisition%* are chosen. If *Allow Disconnected Block* was used in *Connection Graph,* here *Interpol Disconnected Block* should be set as *True.*

*Geocoding*

Results are geocoded in *ground range* and plot with *Time Series Analyser* can be observed. *Velocity* and *Height Precision* should be modified to increase the covering with the risk to increase also the noise, because of the less precision to estimate data by the software. If both acquisition geometries are available, the *Displacement Decomposition from Asc and Desc Geometries* can be used to project displacements values along *the ground range* for vertical and horizontal (EW) component.

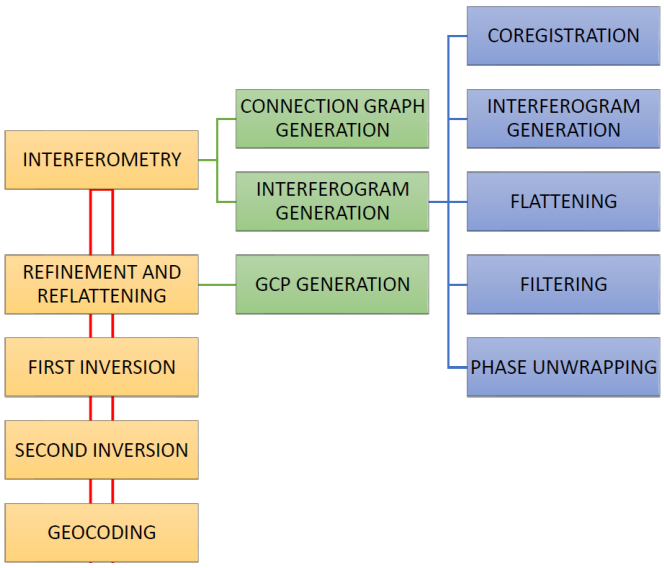


*Fig. 34: Diagram showing all the SBAS processing steps. (Beccaro, 2018)*

## 3.5 Satellites and sensors dataset

SAR data that have already undergone *focusing* and *multi-looking* processing, are composed by an amplitude (A) and a phase (φ) content. The first one allows to identify at the sensor the intensity of the backscattered electromagnetic field received from an object on the terrestrial surface. These images are representative of the dielectric properties of the encountered obstacles: the image is light, where there are metallic buildings as antenna, railways, etc, instead, it is dark in correspondence of water, streets and everything is characterized by a specular reflection (only a little portion of the reflected signal is sent back to the satellite). It is mainly used for case of floods or evolution of the plants growth. The second one measures the reflected signal and it is representative of the distance between the sensor and the investigated target. Phase is based on the satellite revisiting time and normal baseline and it changes if there is a ground displacement; it is fundamental for interferograms generation and can be used also for produce DEM (Digital Elevation Model).

SAR data acquired by Sentinel-1, ALOS Palsar-1 and ALOS Palsar-2 missions both in ascending and descending orbit, from 2007 to 2011 and from 2014 to 2018, have been used in this work, with the aim to study the behaviour and the main features of Aso volcano.

The employment of two geometries allows to obtain the real component of the vertical and horizontal (EW) displacement. This was not possible in the case of ALOS Palsar-2, because of the insufficient number of available images for the ascending orbit (Fig. 35).

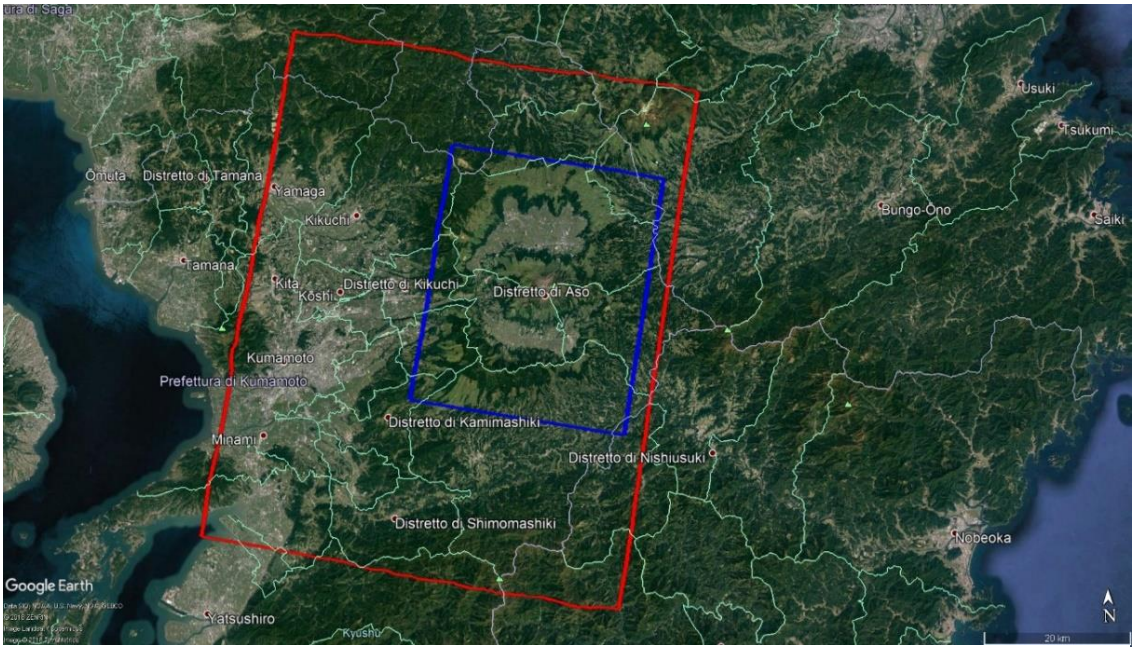


*Fig. 35: View of the full-frame image considered for Palsar-2 (red rectangle). Blue rectangle is representative of the area considered for our discussion.*

Sentinel-1 is a mission of ESA (European Space Agency) part of the Copernicus program. It comprises a constellation of two near-polar, sun-synchronous orbit satellites (Sentinel-1A and Sentinel-1B), acquiring in C-band and with a revisiting time of 12 days for a single geometry and 175 revolutions for cycle. Both the satellites offer a 6 days repeat cycle (period to return to the original path) at the equator and they share the same orbit plane with a 180° orbital phasing difference. Sentinel-1A was launched on April 3, 2014 and Sentinel-1B on April 25, 2016. In our case, the swath width considered is of 250 km with a ground resolution of 15 m and an incident angle between 29.1° - 46.0°.

ALOS Palsar-1 (Phased Array type L-band Synthetic Aperture Radar) is a sensor developed by JAXA (Japan Aerospace Exploration Agency) in collaboration with the Japan Resources Observation System Organization (JAROS) and it acquire in L-band with a ground resolution of 15 m. It is a sun-synchronous orbit and revolved around the earth every 100 minutes (14 times a day) with a repeat cycle and revisiting time of 46 days. Launched on January 24, 2006 and operating until May 12, 2011, its swath width was 70 km for the fine mode with an incident angle of 34,3°.

ALOS Palsar-2 is the consequent sensor of Palsar-1 launched on 2014 by JAXA it acquires in L-band with a *range* resolution of 3 m, an *azimuth* resolution of 1 m, a ground resolution of 3 m and a swath area of 50 km (incident angle: 37°). In our cases, we process full-frame images with a ground resolution of 15 m. Its revisiting time is of 14 days and it has a sun-synchronous orbit. The difference from the other satellites, that have only the right-side looking, is that ALOS-2 has the capability to right- or left-side looking observation.

Each Sentinel-1 geometry was processed full-frame in two different intervals considering the $M_w$ 7.0 Kumamoto earthquake happened on April 16, 2016: it has been evaluated a period before the mainshock (from 11/21/2014 to 03/27/2016 for descending geometry along track 163 and from 05/08/2015 to 04/08/2016 for ascending geometry along track 156) and a period after the event (from 04/20/2016 to 10/07/2018 for track 163 and from 05/02/2016 to 07/09/2018 for track 156). For ALOS Palsar-2, the time interval considered for path number 73 (descending orbit) is after the earthquake. (Tab. 3).
Both sensor Palsar-1 and Palsar-2 can have single (FBS) polarisation with HH or HV types or dual (FBD) polarisation with HH+HV or VV+VH type. The Interferometric Wide swath (IW) acquisition mode of Sentinel-1 has the same polarisation products of ALOS and ALOS-2. In this work, HH type has been used for Palsar-1 and Palsar-2, instead for Sentinel-1 has been used the VV type.
All the SAR images was processed using a SRTM-1 V3 DEM (30 meters of resolution).

| MISSION | BAND | TIME PERIOD (MM/DD/YY) | TRACK/PATH AND GEOMETRY | RESOLUTION (m) | N° IMAGES | N° INTERFEROGRAMS |
|---|---|---|---|---|---|---|
| ALOS Palsar-1 | L | 06/10/2007_12/19/2010 | 423A | 15 | 22 | 102 |
| | | 01/07/2007_04/20/2011 | 73D | | 22 | 102 |
| Sentinel-1 | C | 11/21/2014_03/27/2016<br>04/20/2016_10/07/2018 | 163D | 15 | 27+62 | 105+327 |
| | | 05/08/2015_04/08/2016<br>05/02/2016_07/09/2018 | 156A | | 12+60 | 81+313 |
| ALOS Palsar-2 | L | 04/18/2016_03/05/2018 | 23D | 3 | 20 | 83 (used: 60) |

*Tab. 3: Characteristics of SAR data used in SBAS processing.*

The main parameters set in the SBAS processing of each SAR dataset are reported in tab. 4 for Sentinel-1 and in tab. 5 for ALOS-1 and ALOS-2.

| **Sentinel-1** | 156A_B | 156A_A | 163D_B | 163D_A |
|---|---|---|---|---|
| *Normal Baseline (%)* | 0-5 | 0-5 | 0-5 | 0-5 |
| *Temporal Baseline (days)* | 0-100 | 0-80 | 0-90 | 0-80 |
| $\alpha max$ | 3 | 3 | 3 | 3 |
| $\alpha min$ | 1 | 1 | 1 | 1 |
| *Decomposition Level* | 2 | 2 | 1 | 1 |
| *Coherence Threshold* | 0,3 | 0,3 | 0,3 | 0,3 |
| *% interferogram* | 50 | 50 | 50 | 50 |
| *% images* | 50 | 50 | 50 | 50 |
| *Height precision* | 5 | 5 | 5 | 5 |
| *Velocity precision* | 8 | 8 | 8 | 8 |
| *Processing resolution (m)* | 15 | 15 | 15 | 15 |

*Tab. 5: Main parameters set in the SBAS processing of the Sentinel-1 SAR data.*

| **ALOS Plasar-1** | 73D | 423A | **ALOS Plasar-2** | 23D |
|---|---|---|---|---|
| *Normal Baseline (%)* | 0-45 | 0-45 | *Normal Baseline (%)* | 0-35 |
| *Temporal Baseline (days)* | 0-365 | 0-365 | *Temporal Baseline (days)* | 0-130 |
| $\alpha max$ | 3 | 3 | $\alpha max$ | 2,5 |
| $\alpha min$ | 1 | 1 | $\alpha min$ | 0,3 |
| *Decomposition Level* | 2 | 2 | *Decomposition Level* | 1 |
| *Coherence Threshold* | 0,3 | 0,3 | *Coherence Threshold* | 0,3 |
| *% interferogram* | 50 | 50 | *% interferogram* | 70 |
| *% images* | 50 | 50 | *% images* | 70 |
| *Height precision* | 5 | 5 | *Height precision* | 15 |
| *Velocity precision* | 8 | 8 | *Velocity precision* | 26 |
| *Processing resolution (m)* | 15 | 15 | *Processing resolution (m)* | 15 |

*Tab. 4: Main parameters set in the SBAS processing of ALOS Palsar-1 and ALOS Palsar-2 SAR data.*

After velocity and displacement maps have been obtained, we tried to correlate ground variation with the corresponding time interval activity of Aso volcano. This was made plotting displacement time series calculated in some different sector of the volcanic apparatus (tab. 6)

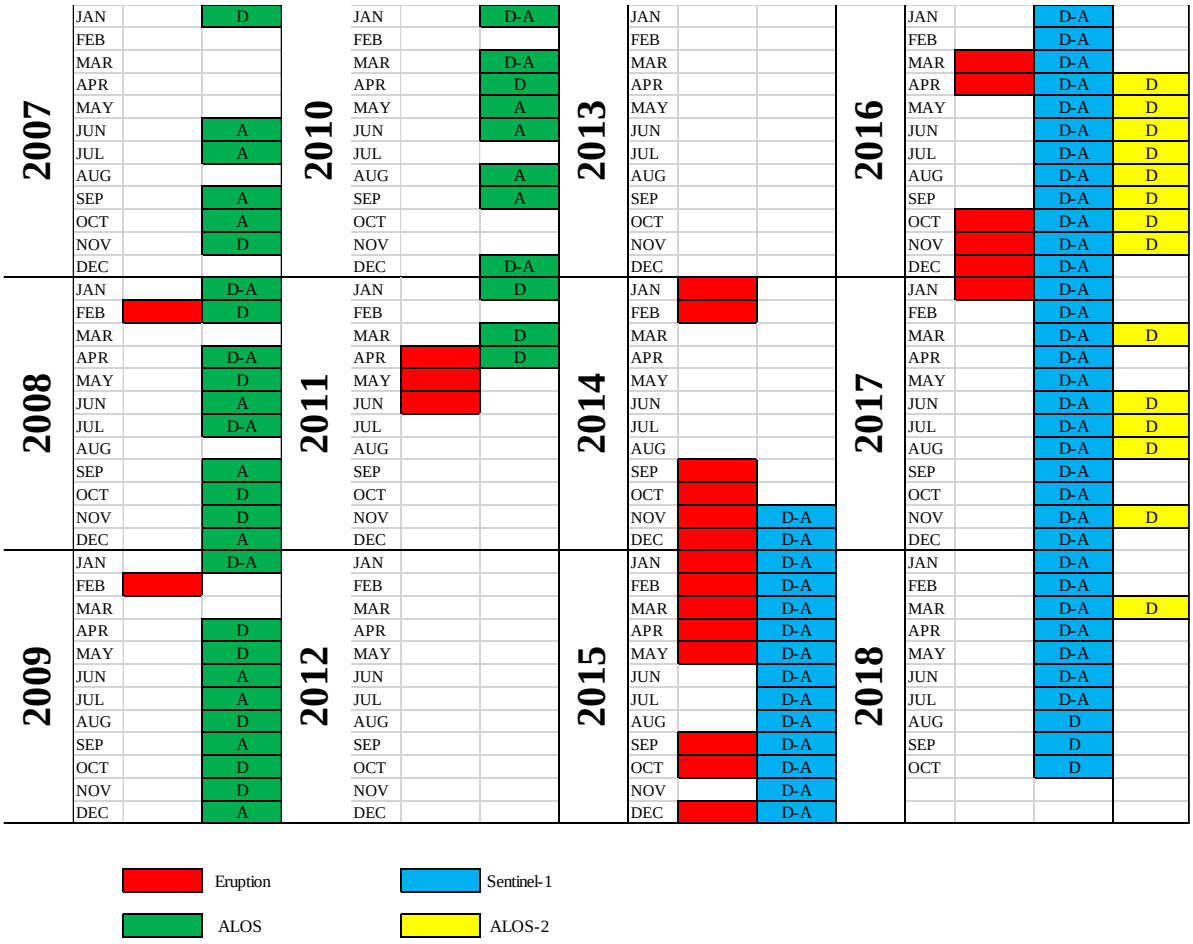


*Tab. 6: Correlations between the volcanic activity Aso and acquisition of SAR from 2007 to 2018. Letter D indicates the descending orbit, A the ascending one.*

All the SAR data have been compared with GPS describe in the next section 3.6.

To study the $M_w$ 7.0 Kumamoto earthquake of April 16, 2016, pairs of images have been considered. For Sentinel 1, the images chosen for the descending orbit have been taken on 03/27/2016 and 04/20/2016 and for ascending orbit 04/08/2016 and 04/20/2016. For ALOS-2 the pairs 03/07/2016 and 04/18/2016 for descending geometry have been considered. The parameters used are reported in tab. 7.

| | ALOS Palsar-2 | Sentinel-1 |
|---|---|---|
| *Time Period (MM/DD/YY)* | 03/07/2016_04/18/2016 | 04/08/2016_04/20/2016 |
| $\alpha_{max}$ | 3 | 3 |
| $\alpha_{min}$ | 1 | 1 |
| *Unwrapping threshold* | 0,3 | 0,25 |
| *Decomposition level* | 1 | 1 |

*Tab. 7: Main parameters set in the interferometric processing of ALOS Palsar-1 and ALOS Palsar-2 SAR data.*

## 3.6 GPS dataset

As comparison to time series derived from the SAR images, continuous GPS data was used in this work. Since 1993, the first GPS network have been built and installed by GSI (Geographical Survey Institute) in Japan.

Successively, in 1996, GSI improved its network with the GEONET (GPS Earth Observation Network) to monitor and detecting significant crustal movement events. In 2004, GEONET became the largest regional GPS network in the world with about 1.200 continuous sites. Today, they also are important instrument for the earthquake studies (Sagiya 2004).

The raw data obtained from GSI consist of a .POS extension file reporting daily coordinates of each station estimated by assuming a fixed point or the reference frame, generally ITRF2005.

Through SARscape software, GPS have been imported and linearly fitted (or filtered to 7 days in the case of the coseismic slip study) to obtain an average velocity for NS component, an average velocity for EW component and one for a vertical component for each station. Every velocity value is measured in mm/yr.

In our case, 14 GPS around Aso volcano was considered (Fig. 36).

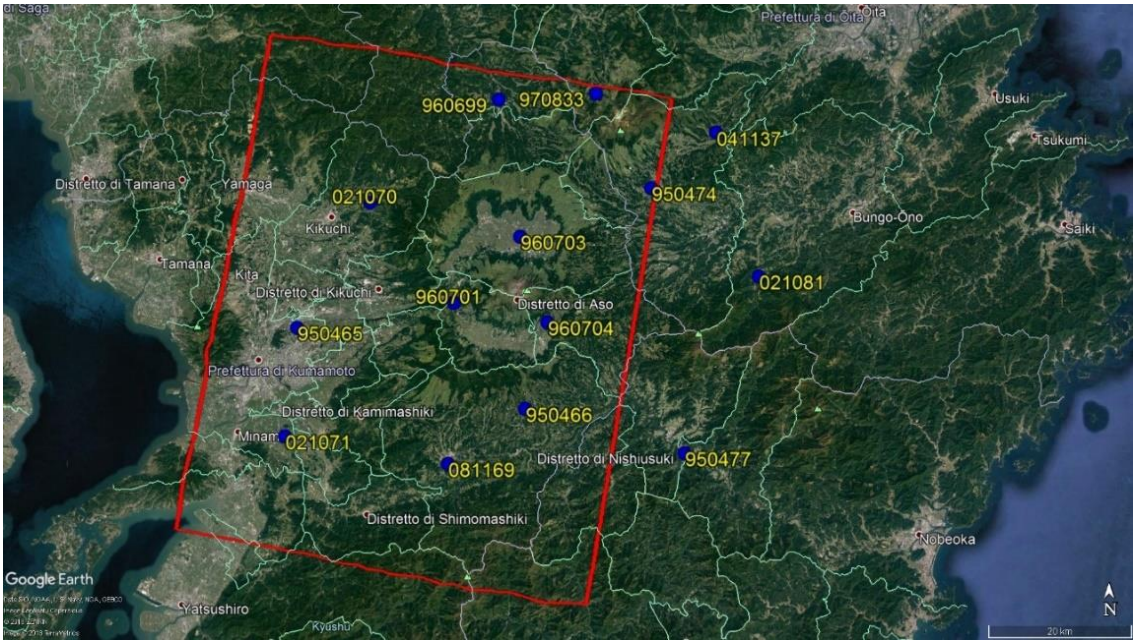


*Fig. 36: Position of the GPS used (blue circle) and their number respect to the full-frame Palsar-2.*

In general, GPS measurements are influenced by many factors: global tectonic, regional tectonic, local tectonic, seasonal motion, climatic and anthropic.

Considering that the Kyushu Island is a complex geodynamic area, one of the aims of this work was trying to eliminate global and regional component, before use them in SARscape software, with the purpose to study the behaviour of the volcanic apparatus through the estimation of ground displacements. To exclude the influence of the plate motion in all the dataset, it has been calculated an average velocity for horizontal (NS and EW) and vertical components measured by the 70 GPS in the whole Kyushu Island: these values with preponderant SE direction, have been subtracted to horizontal and vertical component of the 14 GPS station considered in our work. To avoid the coseismic displacements due to the mainshock $M_w$ 7.0 Kumamoto earthquake happened on April 16, 2016 and to make comparable the data with the SAR, it has been excluded the period of time one week before and one week after the event in the time series.

The period of time considered for every GPS station and used during the *Second Inversion* of the SAR images processing are: for Sentinel 1 and Palsar-2 from October 2014 to April 9, 2016 and from April 21, 2016 to July 14, 2018 and for Palsar-1 from January 2007 to December 2011. Instead, for studying the coseismic slip during the earthquake, were

considered the displacements measured one month before and after the mainshock during the *Refinement and Reflattening* step.

# Chapter 4: Results

Our study was mainly focused on the Aso caldera using SBAS (Small Baseline Subset) technique to understand the ground displacements variations due to the magmatic chamber in three different periods, as shown in section 3.5 (Tab. 3).

The study of the earthquake through InSAR, was focused over the Kumamoto city to understand Futagawa and Hinagu fault behaviour and if it has some effects on the volcano activity, as shown in Fig. 35.

As discussed in section 3.6, the use of GPS was necessary for a comparison with the SAR velocity maps in the *Second Inversion* processing step for SBAS technique and in *Refinement and Reflettening* for InSAR. After their elaborations, different velocity directions were obtained for each time period considered.

The GPS mean velocity directions calculated for the time span 2007-2011 are shown in Fig. 37. Some of them reflect the WSW trend of Fig. 6, due to the subduction of the PHS plate beneath the Eurasian one. In the northern and in the southern part, GPS 950465, 021071, 021070, 081169, 960669 have different directions respect to the other.

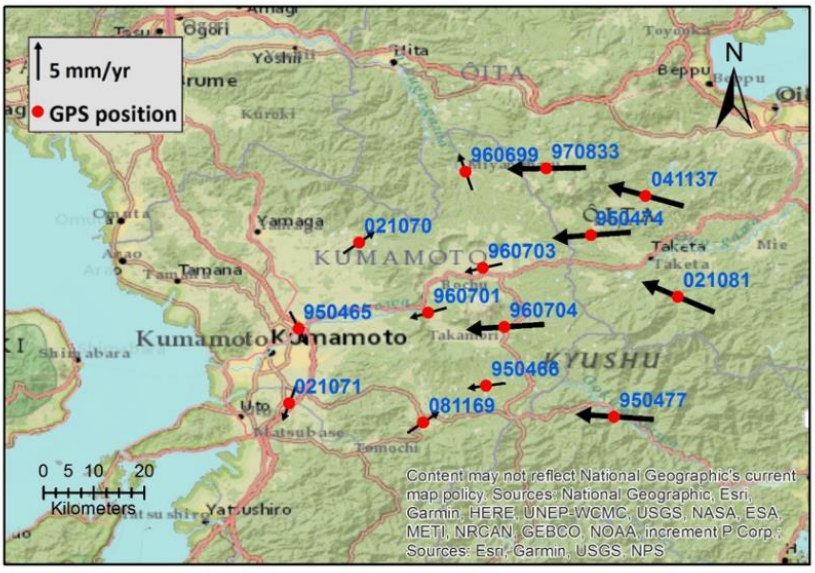


*Fig. 37: GPS horizontal velocity vectors in the time span from 2007 to 2011.*

In Fig. 38 are reported the GPS vertical velocity for the same period of time. All of them are characterized by a subsidence.

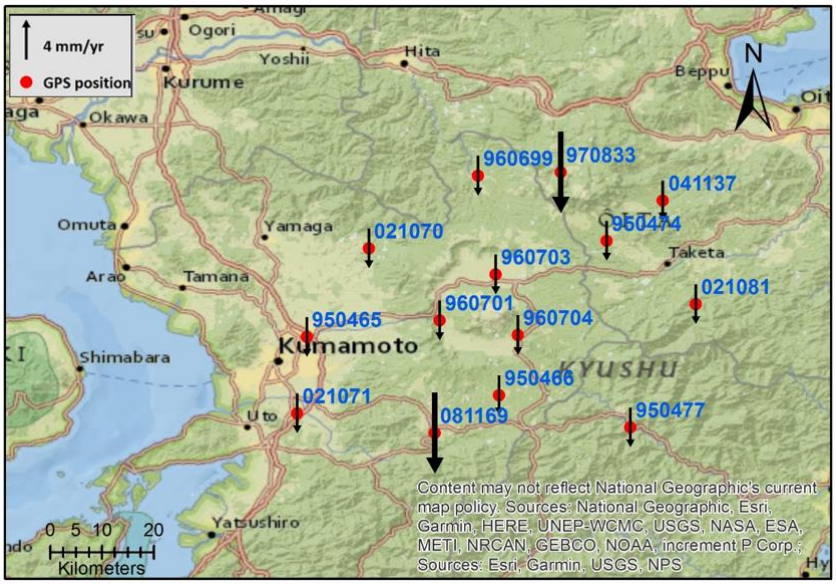


*Fig. 38 GPS vertical velocity vectors in the time span from 2007 to 2011.*

In the case of the time span before the earthquake (October 2014-9 April 2016), the resultant vectors for each station (Fig. 39) have direction similar to Fig. 6.

The main direction is toward WSW.

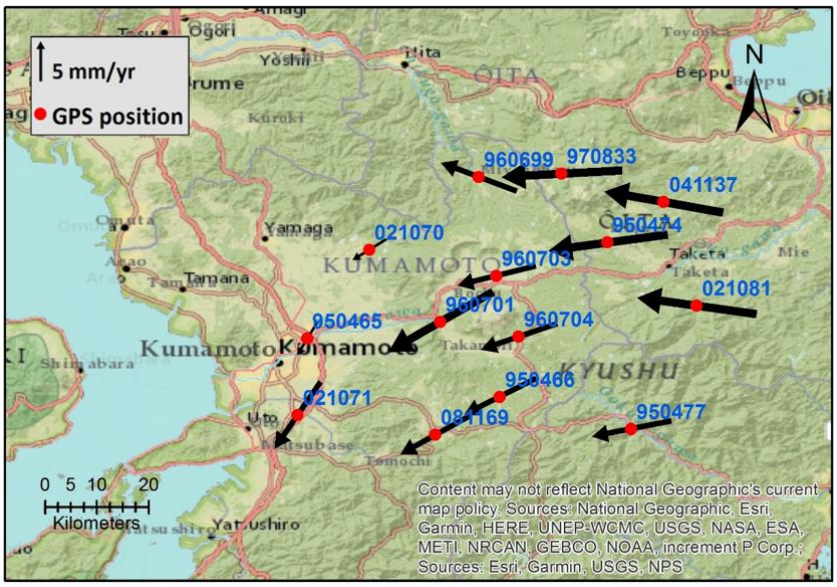


*Fig. 39: GPS horizontal velocity vectors in the time span from 2014 to 2016.*

In Fig. 40 are reported the GPS vertical velocity for the period 2014-2016. GPS 021071 and 950474 show an uplift.

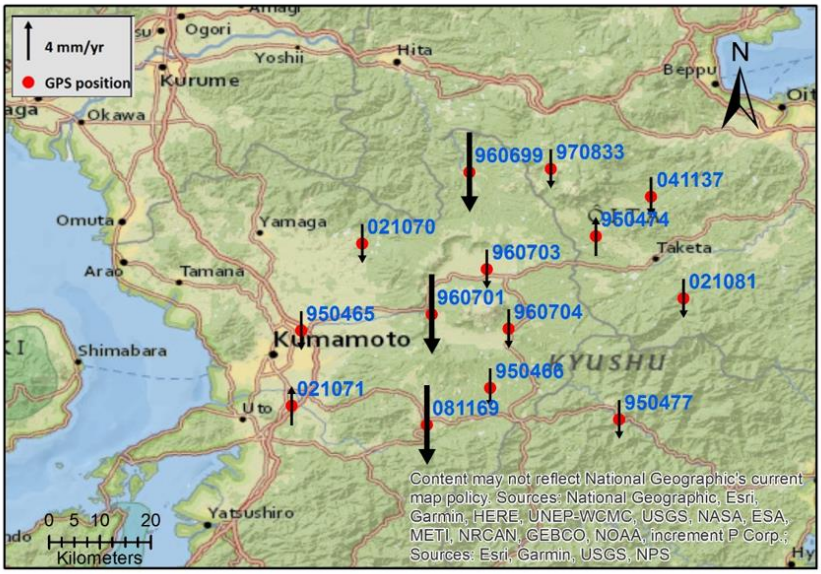


*Fig. 40: GPS vertical velocity vectors in the time span from 2014 to 2016.*

The calculated coseismic horizontal vectors are reported in Fig. 41. Most of them have directions conformed to the regional deformation patterns on geological timescale of the MLT fault. In fact, GPS 950465 and 021071 move toward NE, 960701, 950466 and 081169 move toward SW reflecting the right lateral slip along Futagawa-Hinagu fault. These results are in agreement with Kato et al. (2016).

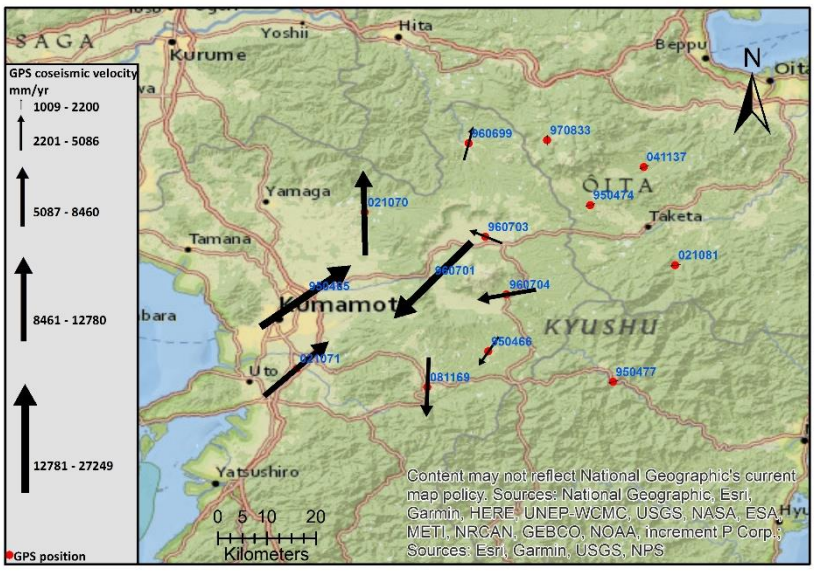


*Fig. 41: GPS horizontal velocity vectors during the Kumamoto earthquake.*

In Fig. 42, the mean velocity vectors show subsidence more evident in GPS 950465 and 021071 due to the seismic event. GPS 960701 indicates an uplift.

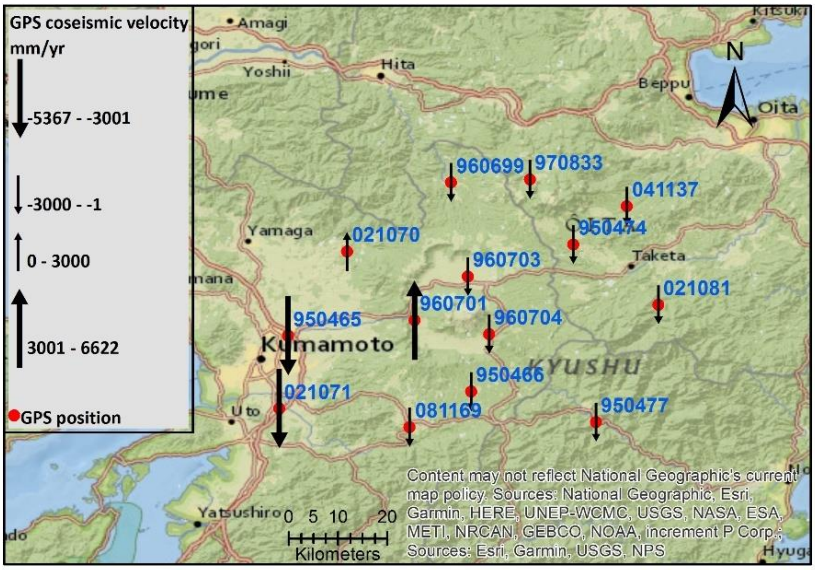


*Fig. 42: GPS vertical velocity vectors during the Kumamoto earthquake*

After the mainshock (21 April 2016-14 July 2018), the resultant velocity vectors, considering the subtraction of the SE main component, show a WSW main trend due to the post seismic effect: GPS 950465, 021070 and 960699 move toward NNW and 021071 toward SE (Fig. 43).

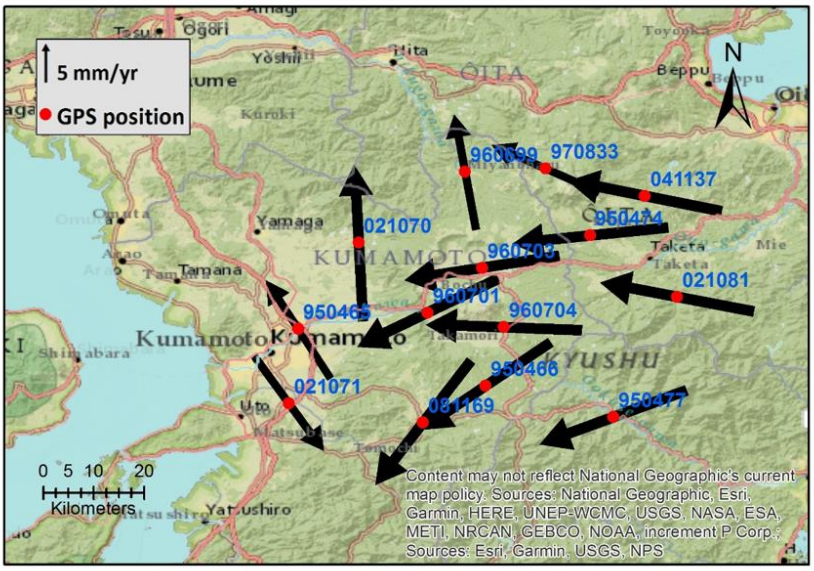


*Fig. 43: GPS horizontal velocity vectors in the time span from 2016 to 2018.*

In Fig. 44 the most of the vertical velocity vectors, in the period 2016-2018, show an uplift except for GPS 960699, 970833 and 960704

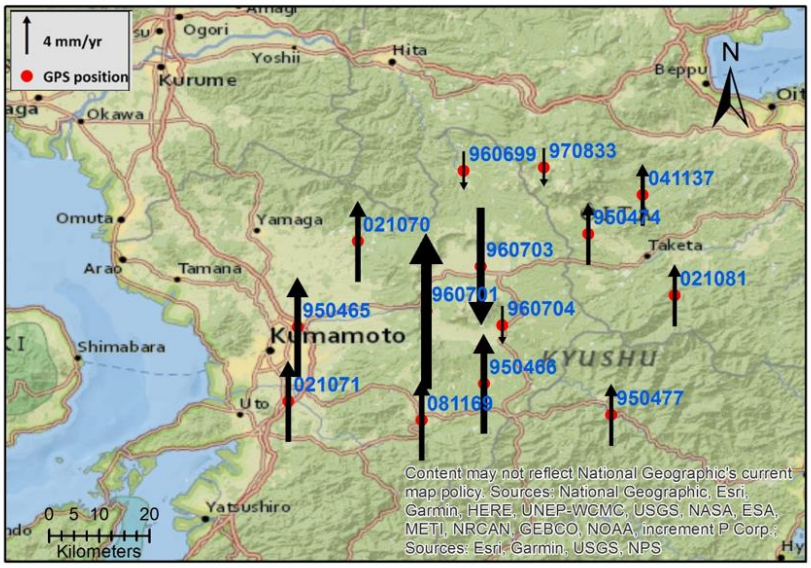


*Fig. 44: GPS vertical velocity vectors in the time span from 2016 to 2018.*

In section 4.1, the displacement rates analysed for each period are relative to the plot in correspondence to GPS 960701, 960703, 960704 (Fig. 36), inside the caldera, and to Nakadake and Kusasenri craters, located in the post caldera central cones. (Fig. 11).

# 4.1 Velocity maps and displacement time series

## *4.1.1 Palsar-1 dataset*

Starting from 22 SAR images for each ascending and descending geometries, 102 interferograms have been generated for each geometry, setting 45% for the normal baseline and 360 days for the temporal baseline (Fig. 45).

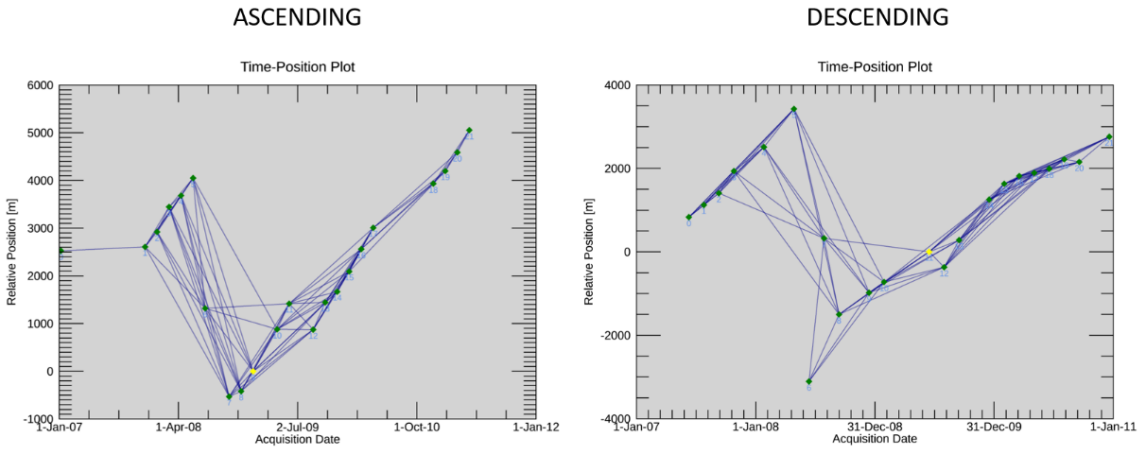


*Fig. 45: Time-Position plot for ascending (left) and descending (right) geometry. In green are shown the different images used for the processing. In yellow is indicated the supermaster.*

Observing velocity maps obtained after the processing with the setting reported in Tab. 4 (section 3.5), it can be detected a wide noisy coverage in the whole frame (Fig. 46). A prevalent stability is highlighted within the caldera (green colour) and an isolated subsidence (blue colour) outer the southern rim for ascending geometry. Instead, for the descending geometry apparent stability prevails inside the caldera and accentuated subsidence in the western part of the post-caldera central cones.

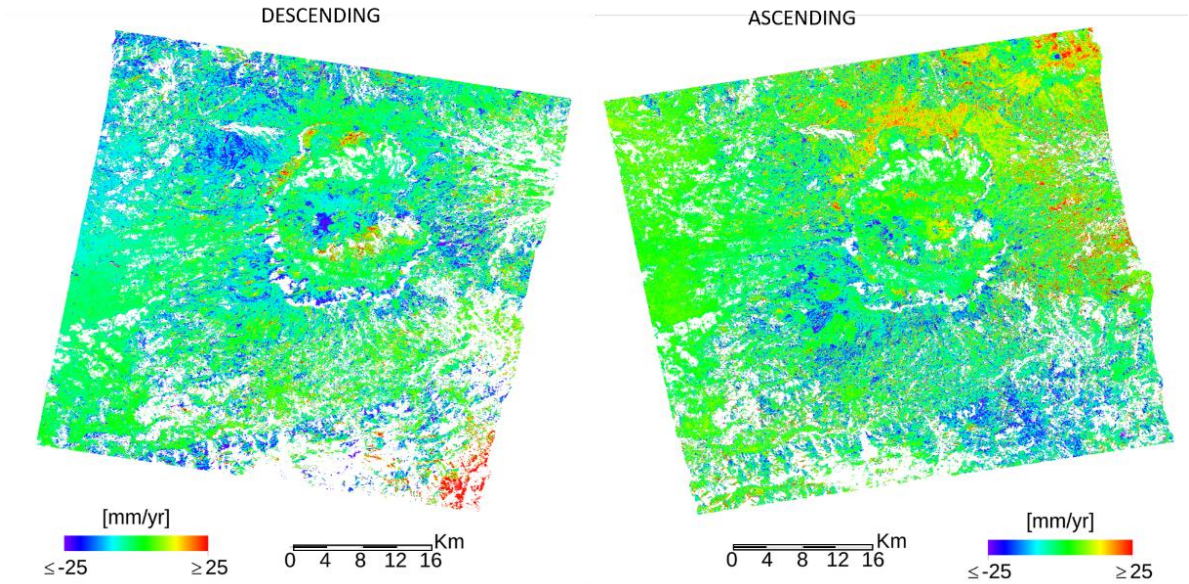


*Fig. 46: Velocity map for the descending and the ascending geometry in the time span 2007-2011. Blue indicate subsidence, green stability and red uplift.*

Having two geometries available, it was possible to combine them with *Displacement Decomposition from Asc and Desc Geometries.* The results for vertical and horizontal (EW) displacements are shown in Fig. 47.

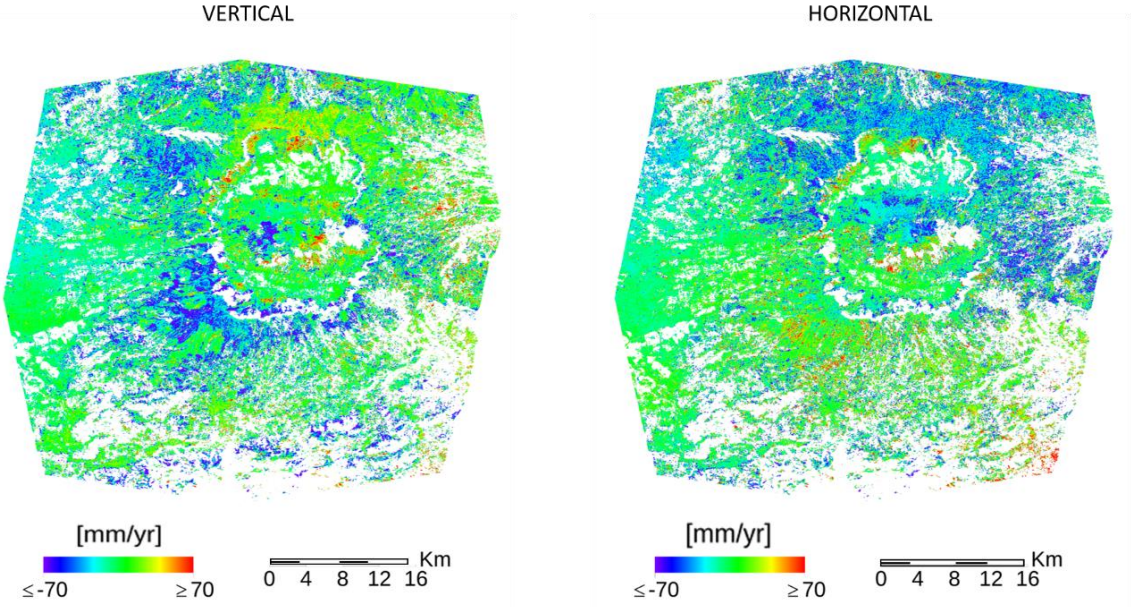


*Fig. 47: Vertical and horizontal (EW) displacement rate in the period 2007-2010. In the case of vertical map, blue indicates subsidence, green stability and red uplift. In case of the horizontal one blue represents a westward motion and red an eastern one.*

For the horizontal deformations, in the northern and central part of the caldera, it is visible a prevalent motion westward (blue colour), in the southern part it is quite stable (green colour). The vertical map indicates similar colour inside the rim: blue colour (subsidence) in the central part of the caldera and green colour (stability) in the northern and southern part. In particular, this one seems to confirm the subsidence in the western part of Kusasenri, showed by the descending geometry.

Any of the three GPS, situated within the caldera, don't agree with the vertical and horizontal deformation trend estimated by interferometry. In fact, GPS 960701, 960703, 960704 in Fig. 38 show a prevalent negative vertical trend (downlift) in opposition to the vertical displacement plot, in correspondence of the GPS location in Fig. 48: 960701 and 960703 have a positive trend (uplift). Four earthquakes are visible in the displacement time series reported in Fig. 48: the $M_w$ 3.9 on August 07 2007 with epicentre 60 km far from the caldera, the $M_w$ 3.8 on September 12 2008 with epicentre 50 km far from Aso, the $M_w$ 4.5 on June 25 2009 with epicentre 100 km far from the volcano and the $M_w$ 4.8 May 2010 with epicentre 100 km far.

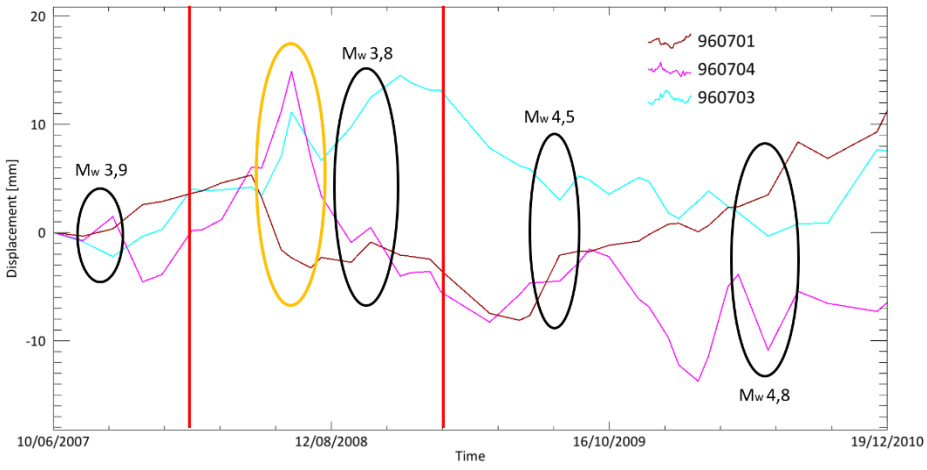


*Fig. 48: Vertical SAR time series plot in correspondence of the three GPS positions, situated inside the caldera rim. Black ellipses highlight seismic events, orange ellipse show a systematic effect in the frame, red line indicate the degassing activity in time period from January 2008 and February 2009. Date format: DD/MM/YY.*

The same problem is present in the horizontal displacement plot in correspondence of GPS 960704 (Fig. 49), which doesn't reflect the negative information trend given by the GPS (Fig. 37).

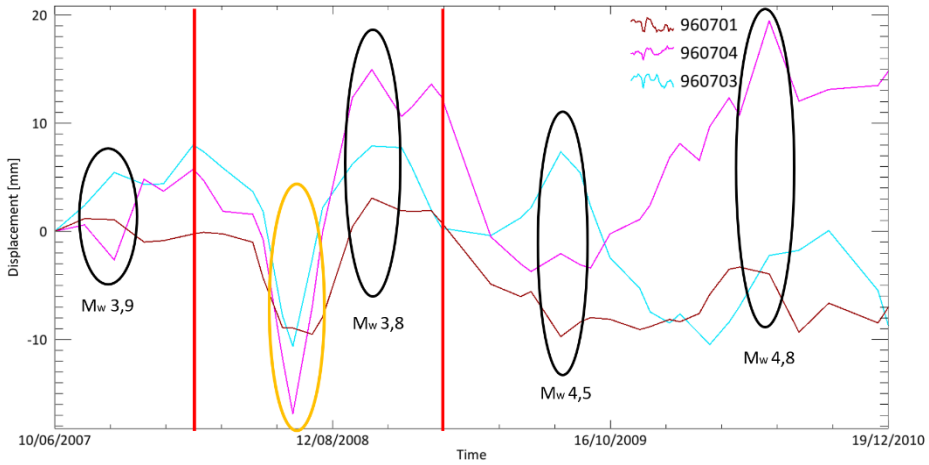


*Fig. 49: Horizontal SAR displacement time series in correspondence of the three GPS, situated inside the caldera rim. Black ellipses highlight seismic events, orange ellipse show a systematic effect in the frame, red line indicate the degassing activity in time period from January 2008 and February 2009. Date format: DD/MM/YY.*

However, the vertical and the horizontal curves are always in opposition in Fig. 48 and Fig. 49: when there is an uplift (positive trend), the plot shows a motion toward west (negative trend) and vice versa.

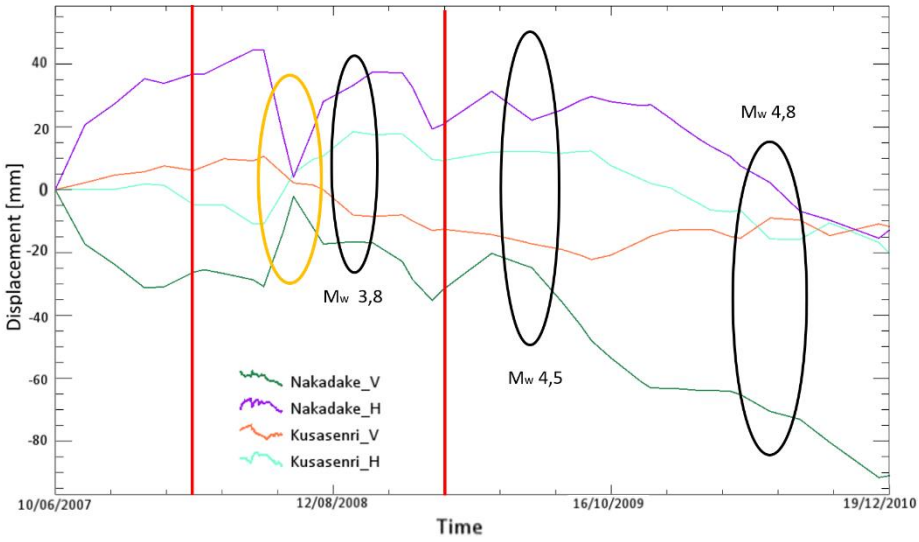


*Fig. 50: Time series plot of vertical (V) and horizontal (H) displacements directions for the Nakadake and Kusasenri craters. Black ellipses highlight seismic events, orange ellipse show a systematic effect in the frame, red line indicate the degassing activity in time period from January 2008 and February 2009. Date format: DD/MM/YY.*

In Fig. 50 are shown the time series of the vertical and horizontal deformations affecting the western part of the Kusasenri crater: when an inflation occurs, a slightly motion toward west is present. On the contrary, when a deflation occurs, an eastward motion is

present. In case of the Nakadake crater: until July 2008 an opposite behaviour respect to Kusasenri crater was observed, vertical and horizontal motions have the same negative trend, which means subsidence and horizontal displacements directed to West.

### *4.1.2 Sentinel-1 dataset*

For Sentinel-1, starting from 12 images for the period May 2015 - April 2016 for ascending geometry and 27 images for the period November 2014 - April 2016 for descending geometry, 81 and 105 interferograms were generated, respectively (Fig. 51).

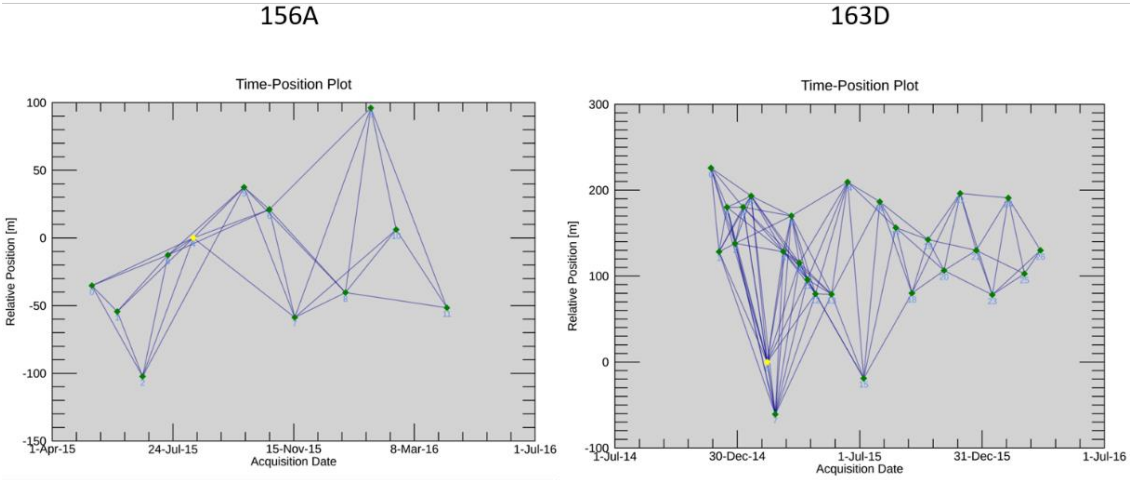


*Fig. 51: Time-Position plot for ascending (left) and descending (right) geometry. In green are shown the different images used for the processing. In yellow is indicated the supermaster.*

The resultant velocity maps processed with parameters reported in Tab. 4 (section 3.5), are show in Fig. 52. The descending geometry is very noisy and totally different from the ascending one. In both a subsidence (blue colour) is evident in the post-caldera central cones.

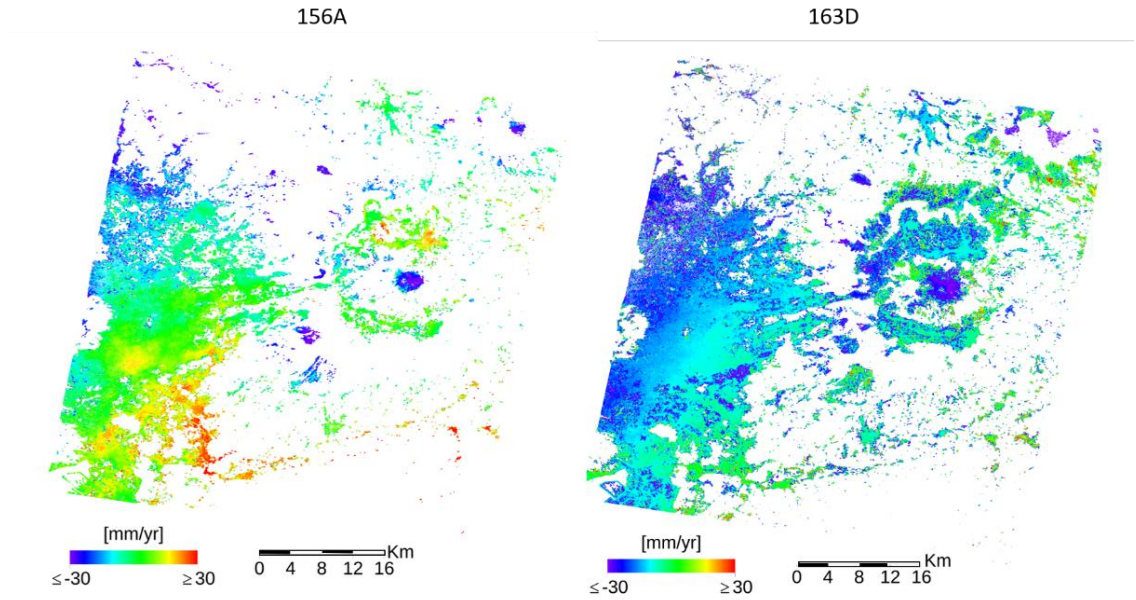


*Fig. 52: Velocity map for the ascending and the descending geometry in the time span 2014-2016. Blue indicates subsidence, green stability and red uplift.*

The vertical and horizontal displacements rates maps are reported in Fig. 53.

The two maps are very noisy and with low coverage and this not allows to plot the displacements measured by interferometry in correspondence of GPS locations; as a consequence, it is not possible compare displacement rates by the two different techniques.

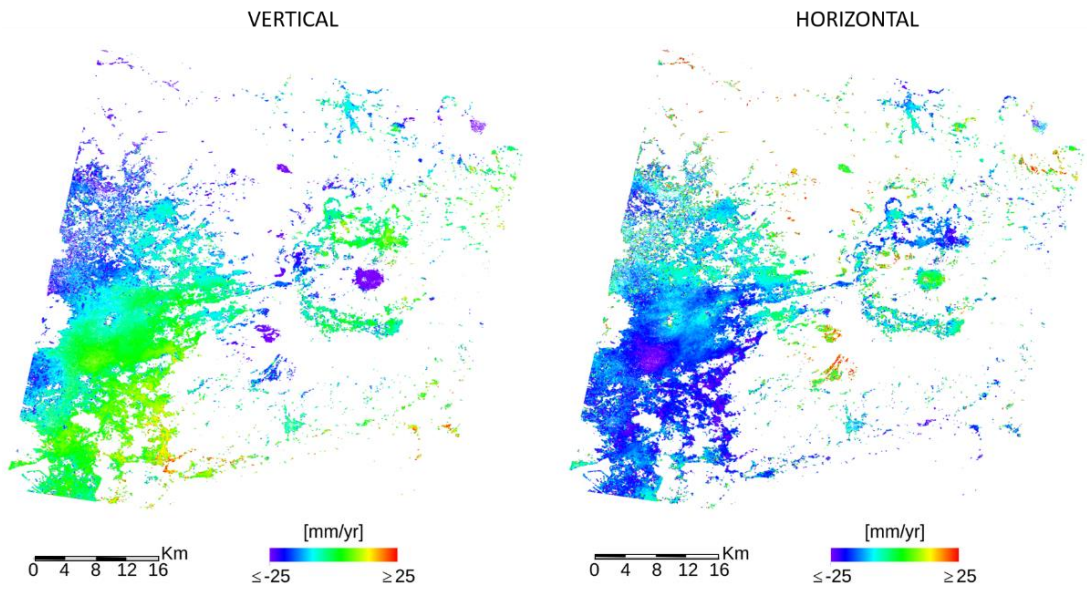


*Fig. 53: Vertical and in horizontal (EW) displacement rate in the period 2014-2016. In the case of vertical map, blue indicates subsidence, green stability and red uplift. In case of the horizontal one blue represents a westward motion and red an eastern one.*

Despite the low availability of starting images, it is possible to plot some points inside the post-caldera central cones, in particular in the main Nakadake crater.

As shown in Fig. 54, the vertical movement has a negative trend (downlift) as for the horizontal one (motion to West). A general subsidence has occurred in this period. A positive peak is associated to the $M_w$ 5.5 earthquake happened on July 12, 2015, ca. 100 km far from the caldera rim. Subsequently from August to October 2015, a series of small eruptions have occurred: the October 23, 2015 eruption can be identified by the charge-discharge trend represented by red arrows.

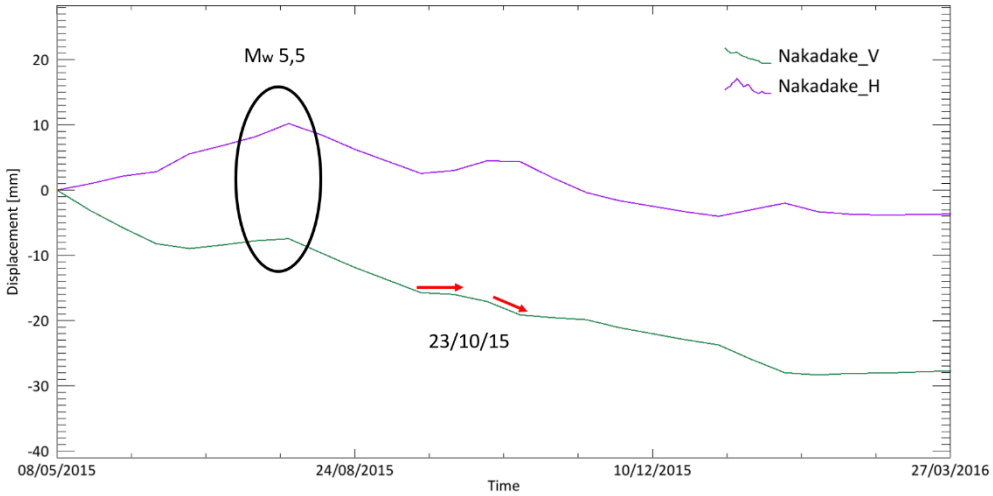


*Fig. 54: Time series plot of vertical (V) and horizontal (H) displacement directions for the Nakadake crater. Black ellipse highlights the Mw 5.5 earthquake. Red arrows represent rise and decrease due to the eruption of the October 23, 2015. Date format: DD/MM/YY.*

For Sentinel-1 in the period April 2016 - July 2018, 313 interferograms were generated for the 156 ascending geometry, instead for the 163 descending one (from April 2016 to October 2018), 327 interferograms were created. A temporal baseline of 80 days was used for both dataset (Fig. 55).

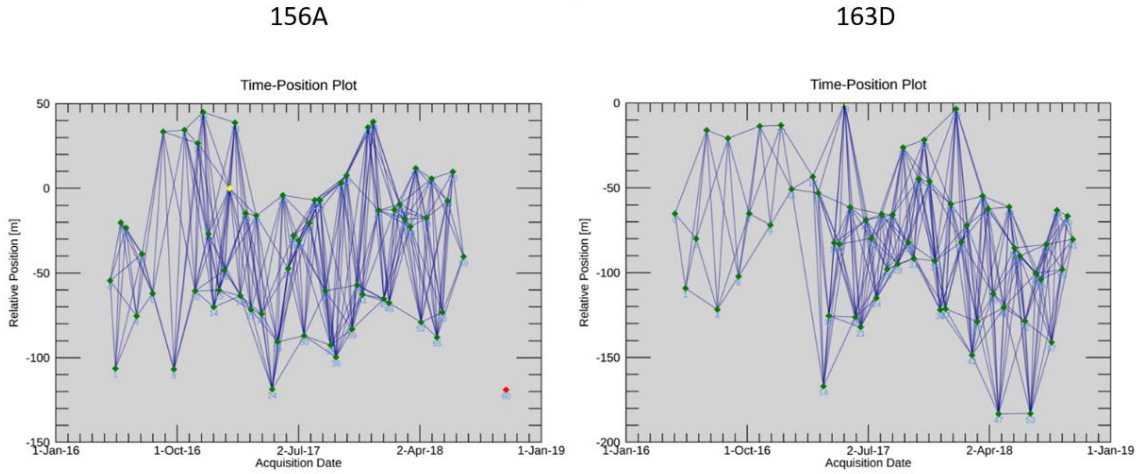


*Fig. 55: Time-Position plot for ascending (left) and descending (right) geometry. In green are shown the different images used for the processing. In yellow is indicated the supermaster and in red the image eliminated after the Interferogram Generation step.*

In the time span of the considered images, the coverage is not so good for both the geometries. The ascending has more information than the descending one, but both give the same deformation trend with a slight difference in the rate, in particular in the southwestern part of the caldera rim (Fig. 56).

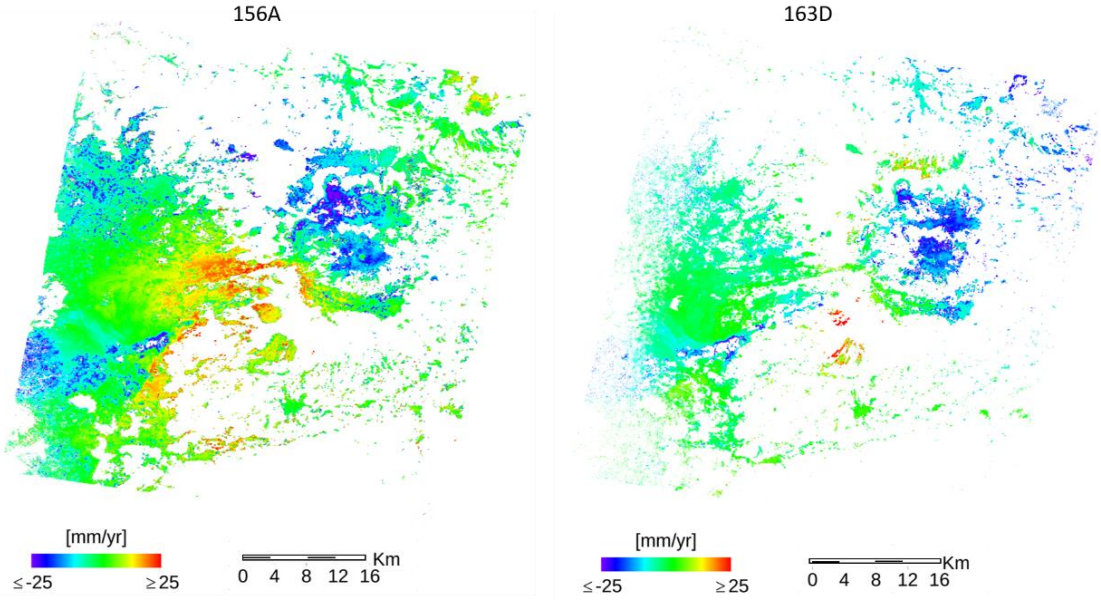


*Fig. 56: Velocity map for the ascending and the descending geometry in the time span 2016-2018. Blue indicates subsidence, green stability and red uplift.*

As in Palsar-1, the plot of the displacements time-series was done using the composition between the two geometries. The trend inside the caldera show, in most of cases, a different vertical displacement respect to the horizontal one: for instance, in the southern rim to an uplift (red colour/positive trend), correspond a westward motion (blue colour/negative trend) (Fig. 57).

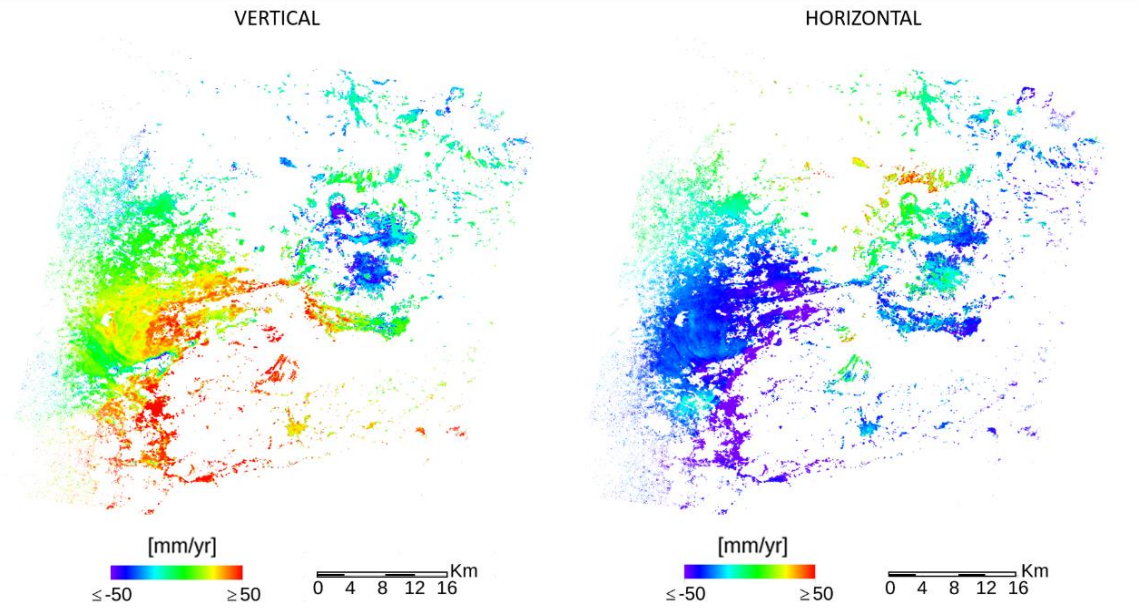


*Fig. 57: Vertical and in horizontal (EW) displacement rate in the period 2016-2018. In the case of vertical map, blue indicates subsidence, green stability and red uplift. In case of the horizontal map, blue represents a westward motion and red an eastern one.*

Plotting the vertical displacement in correspondence of the three GPS within the caldera (960701, 960703, 960704) and for a point in correspondence of the main Nakadake crater and one above Kusasenri, it is possible to observe that the general trend is different for each point, but that the oscillations are similar. For instance, the most evident positive peaks (in black ellipses) present in most of the series, correspond to earthquakes occurred in different period in northern and central part of the Kyushu Island. The strongest occurred in this time span are: the $M_w$ 4.8 on June 08 2016, the $M_w$ 4.1 on August 01 2016, the $M_w$ 4.2 on August 19 2016, the $M_w$ 4.9 and $M_w$ 4.6 on August 31 2016, the $M_w$ 4.5 on July 01 2017, the $M_w$ 4.4 on May 06 2018 and the $M_w$ 4.2 on June 07 2018 (Fig. 58).

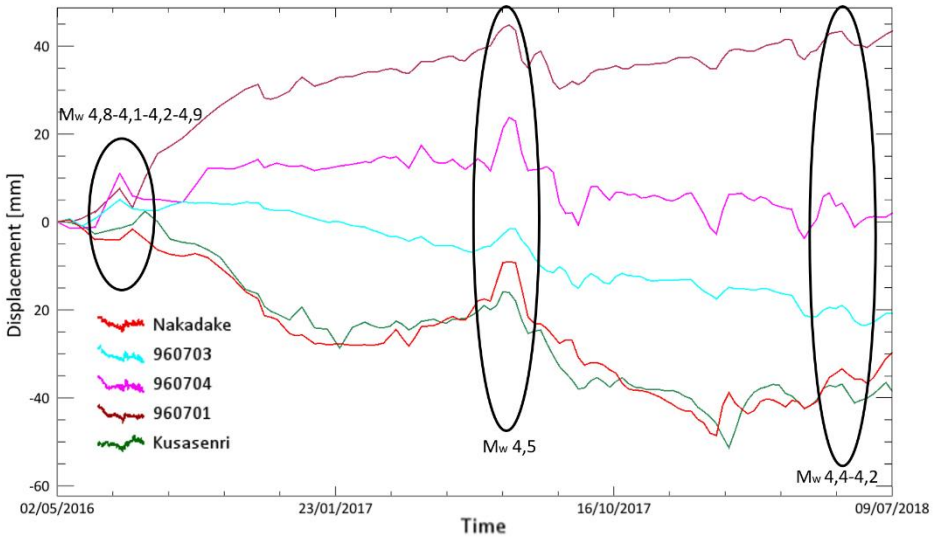


*Fig. 58: Time series plot of vertical displacements for the Nakadake and Kusasenri craters and the three GPS inside the caldera. Black ellipses highlight seismic events. Date format: DD/MM/YY.*

Results from the evaluation of horizontal displacements are similar to those from vertical one. Among the various fluctuations, in all the series are present negative peaks in correspondence of the seismic events: they represent a westward motion (Fig. 59).

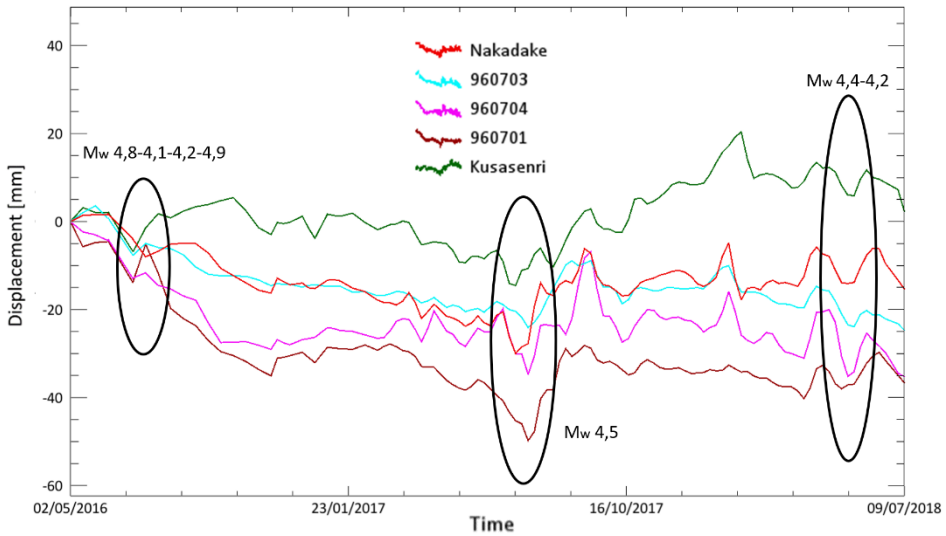


*Fig. 59: Time series plot of horizontal displacements for the Nakadake and Kusasenri craters and the three GPS inside the caldera. Black ellipses highlight seismic events. Date format: DD/MM/YY.*

Observing Fig. 58 and Fig. 59, when for GPS 960701 the horizontal displacement trend is negative (toward west), the trend for the vertical one is positive (eastward); both

displacements trend are negative for 960704 and 960703. The two displacement maps are in concordance with the mean velocity GPS directions in Fig. 43 and Fig. 44.

### *4.1.3 Palsar-2 dataset*

For Palsar-2, only the descending geometry was available, thus, the displacements plot is relative to the LOS, which represents a component of the real displacement. The time period investigates with this sensor is from April 2016 to March 2018. Starting from 20 images, 83 interferograms were created, but only 60 was maintained until the end of the processing. Temporal baseline chosen is of 130 days (Fig. 60). The decision to eliminate some pairs was due to the low coverage or phase ambiguities present after the unwrapping.

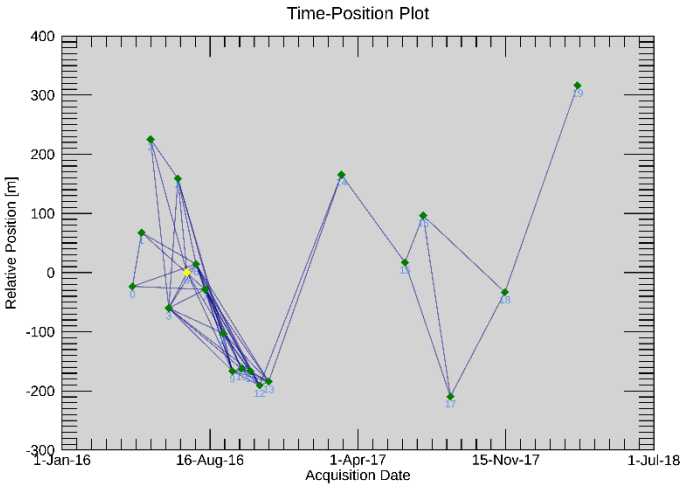


*Fig. 60: Time-Position plot for descending geometry. In green are shown the different images used for the processing. In yellow is indicated the supermaster.*

In Fig. 61 is reported the mean velocity map obtained from the processing.

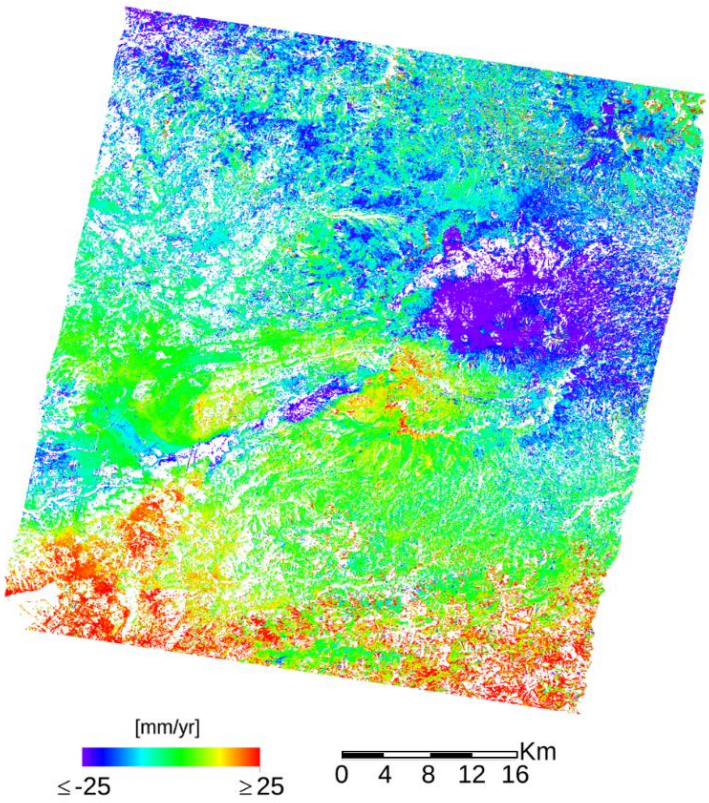


*Fig. 61: Velocity map for the descending geometry in the time span 2016-2018. Blue indicates subsidence, green stability and red uplift.*

The image shows a good coverage and in the northern and in the central part of the caldera is dominant a deflating activity, instead in the southwestern part an uplift.

In Fig. 61 and Fig. 62 is evident also the Futagawa-Hinagu fault (orange line) and Idenokuchi fault (red line) related to seismic and post-seismic effects. Also, in the descending geometry of Sentinel-1 (Fig. 56) is possible to identify this tectonic structure.

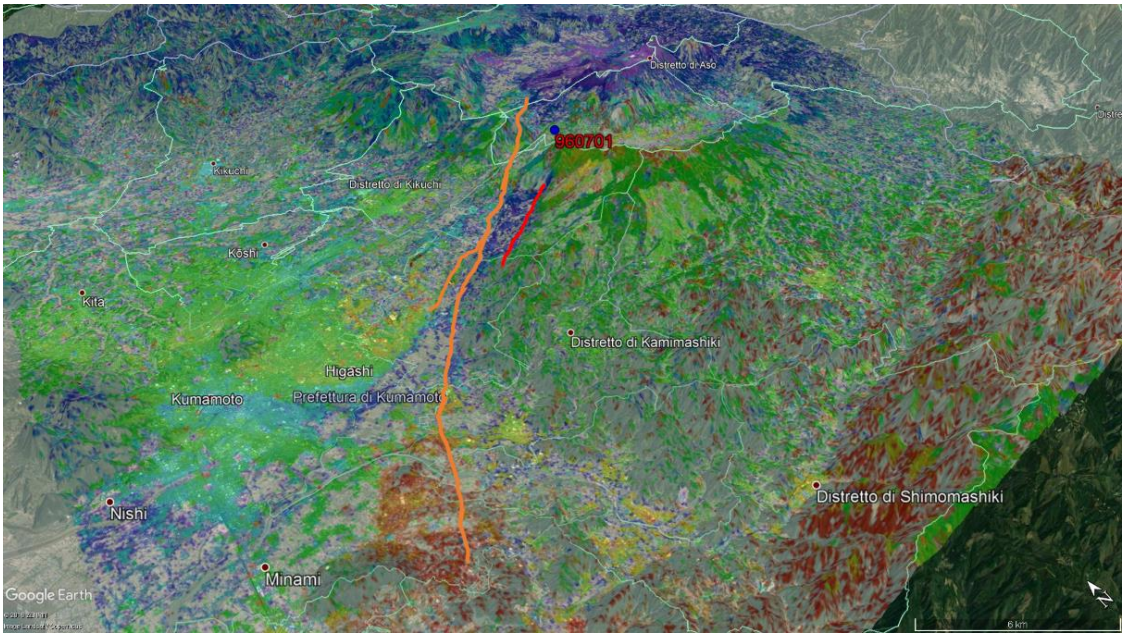


*Fig. 62: Palsar-2 velocity map (descending geometry) in the time span 2016-2018. Red line represents the Idenokuchi fault. The orange line shows the Futagawa-Hinagu fault.*

The displacement rate plotted in correspondence of the GPS within the caldera rim (Fig. 63) confirm the trend directions showed also by Sentinel-1 in Fig. 58, thus they are similar to Fig. 44.

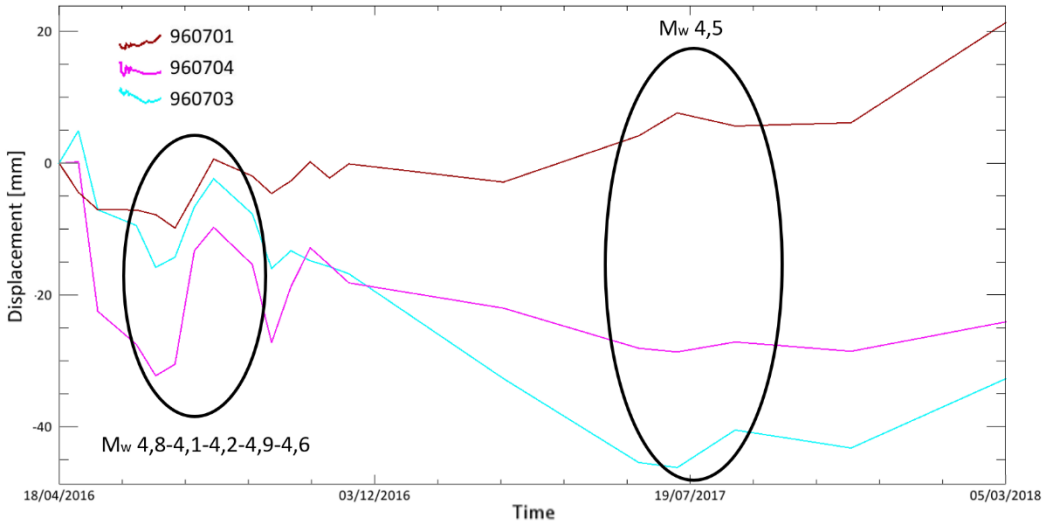


*Fig. 63: Time series plot of vertical displacements for the three GPS inside the caldera. Black ellipses highlight seismic events. Date format: DD/MM/YY.*

## 4.2 Kumamoto earthquake

To better study the coseismic behaviour of the $M_w$ 7.0 Kumamoto earthquake, two different sensors were used to create the interfeograms: Palsar-2 for the time period from March 7, 2016 to April 18, 2016 and Sentinel-1 from April 4, 2016 to April 20, 2016. The parameters used during the processing are reported in Tab. 7 (section 3.5).

In Fig. 64 is shown the Sentinel-1 interferogram, where the main right lateral movement is highlighted. The Aso caldera is subjected to a strong westward displacement. as indicate by the coseismic GPS in Fig. 41.

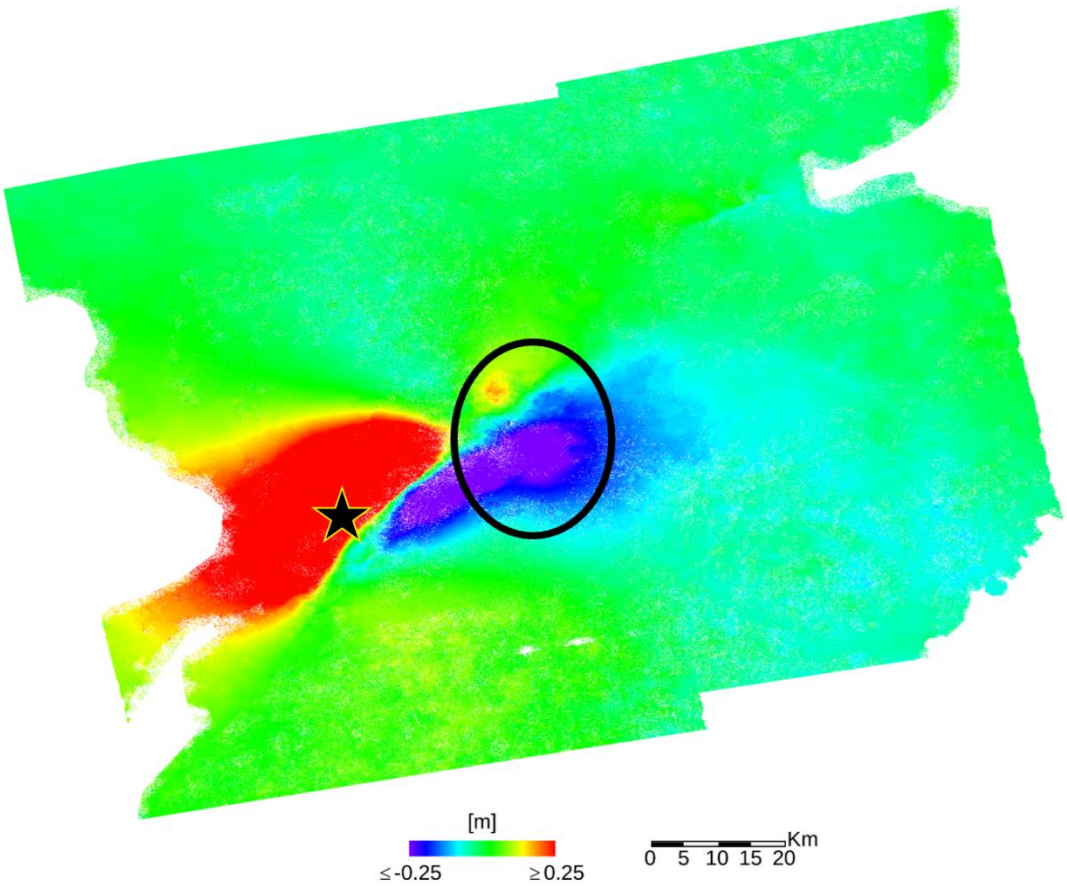


*Fig. 64: Sentinel-1 horizontal displacement map representative of the Kumamoto earthquake. Blue indicates a westward movement, red an eastern ward one. Aso caldera is shown by the black ellipse. Black star highlights the mainshock epicentre.*

In the case of Palsar-2, the displacement map generates the same slip trend of Sentinel-1 and of the coseismic GPS in Fig. 41.
The displacement rates are different from Sentinel-1 values in correspondence of the GPS positions (Fig. 65).

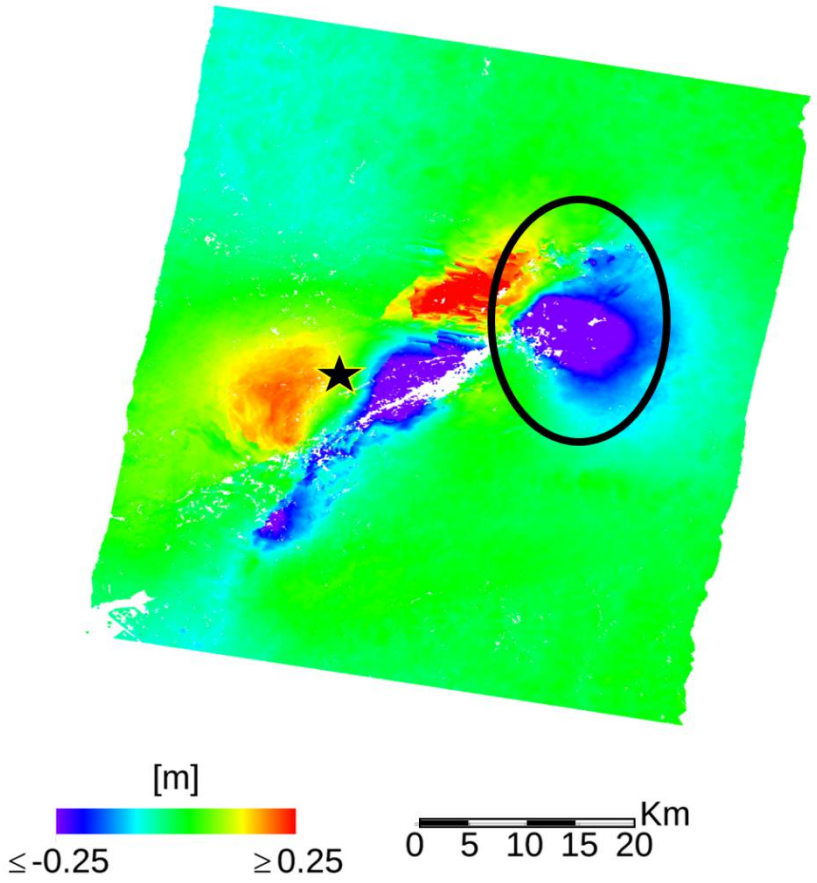


*Fig. 65: Palsar-2 horizontal displacement map representative of the Kumamoto earthquake. Blue indicates a westward movement, red an eastern ward one. Aso caldera is shown by the black ellipse. Black star highlights the mainshock epicentre.*

# Chapter 5: Discussion

Aso volcano is characterized by many periods of unrest: in the time interval between the main eruptions, volcano activity is characterized by fumaroles and degassing, in particular from Nakadake crater.

Considering the velocity maps, it is possible to plot, through the tool *Time Series Analyzer*, displacements along the LOS for a specific point in a certain time span. In case of availability of two geometries, also vertical and horizontal (EW) motion can be plotted.

In this study, we have tried to correlate ground deformations detected by different sensors to the volcanic activity of Aso caldera, with the help of the GPS mean velocity directions obtained after the subtraction of the SE prevalent trend. To this purpose, time series were plotted in correspondence of the GPS 960701, 960703 and 960704 and of the Nakadake and Kusasenri craters. All these points are situated within the caldera rim.

Although the low number of images (22 for each geometries), Palsar-1 shows a good coverage thanks to the possibility of L-Band (wavelength 23.5 cm) to penetrate vegetation, which is very diffused within and around the volcano. The time span of these SAR images covers the period 2007-2011 and it was characterized by a general subsidence trend inside the caldera rim, highlighted by the vertical plot in correspondence of the GPS 960704 (Fig. 48) and of Nakadake and Kusasenri craters (Fig. 50).

The Fig. 50 shows that the vertical trend in Nakadake crater and in surrounding areas, has the same negative displacement trend, which indicate subsidence, and the horizontal displacement general trend, representative of a westward motion. This could be related to the position of the point plotted respect to the magma chamber, assumed below the crater Kunsaseri: if the magma reservoir deflates, there is a western motion, in opposite, if the magmatic chamber inflates, the movement is to the East (Fig. 66).

Observing the small fluctuations (Fig. 50), it can be observed that Kusasenri crater shows a different behaviour: during the uplift, a slightly motion toward west happens, during subsidence, an eastward movement is identified. (Fig. 66)

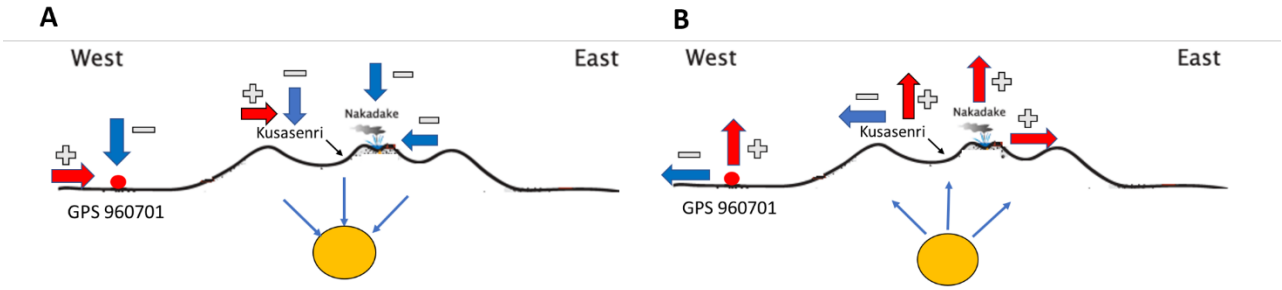


*Fig. 66: EW section of Aso volcano. A) Representation of the main craters and GPS 960701 behaviour in case of magma chamber inflation. B) Representation of the main craters and GPS 960701 behaviour in case of magma chamber deflation. (Unglert et al., 2011, modified)*

In the vertical displacement maps, during the period April-July 2008 are evident anomalous positive (or negative) peaks in most points of the frame, as the one in the orange ellipse in Fig. 48, Fig. 49 and Fig. 50. This could not be attributed to the volcano activity: in fact, the problem is related to an atmospheric effect in the June 12, 2008 ascending image, which overestimate (or understimate) the rate displacements.

The general negative vertical trend showed by the post-caldera central cones could be due to degassing activity between the main eruption of the volcano as observed also by Nobile et al. (2017). In fact, this period 2007- 2011 was characterized by only one significative episode of tephra falls emission in the period from 2008 to February 2009 (Cigolini et al., 2018), but no evidences of this activity inside the caldera are present in the plots, because of the $M_w$ 3.8 seismic event and the atmospheric effect.

The vertical and horizontal movement directions in Fig. 38 and in Fig. 37 is not reflected by the time series trend in correspondence of the GPS position. The main reason of this mismatch may be caused by a not correct phase adaptation between the GPS and the SAR during the processing, because of the very high noise present in the maps, generated by the long revisiting time of Palsar-1 (46 days). In fact, these observed trends don't allow to identify, where the GPS are located respect to the magmatic chamber, also because of their distance to the reservoir.

In Fig. 48 and Fig. 49, the possible reasons of the low presence of peaks related to degassing activity in the time series plotted in correspondence of the GPS position, could be caused by: the low intensity of gas emission, the low availability of starting images

before the processing (22), the stronger energy released by earthquakes present in the time period or the far location of the GPS from the magmatic chamber, that couldn't record the volcanic activity or more likely due to the resultant noise in the vertical and the horizontal displacement maps.

In case of Sentinel-1, the results derived by the processing of SAR data acquired before the $M_w$ 7.0 Kumamoto earthquake show low coverage, due to the low number of images: for the ascending geometry are 12 and for the descending geometry are 27. Another reason of the low coverage is related to the C-band used (wavelength of 5.6 cm) which has difficulties to penetrate vegetation (very dense outer and inner the caldera), consequently decorrelation and loss of information occur.

For the 156 ascending geometry, a subsidence is evident in the post-caldera central cones in agreement with the calculated GPS trend and in part also with Palsar-1. Although the low number of available images (12), this can be related to the good parameters chosen for the processing. A wider coverage above the volcano is available for the track 163 descending, but at the same time it appears very noisy. The combination between the two geometries is a displacement map for vertical and horizontal directions, that in both cases have a low and very noisy coverage, and no reliable information can be extrapolated from the time series of points located inside the caldera.

Despite this problem, the $M_w$ 5.5 earthquake on July 12, 2015 and the October 23, 2015 eruption seem to be detected by the displacement time series of the Nakadake crater (Fig. 54). It can be observed that various small vertical oscillations are present after the $M_w$ 5.5 earthquake: this could reflect the magma ascent in correspondence of the different eruptions happened from August to December 2015. Degassing activity persists in the period between the eruptions and this could be the cause of the subsidence in the post-caldera central cones. The plot of the Nakadake crater in Fig. 54 seems to reflect its position respect to the magmatic chamber: when a deflation occurs, an eastern ward motion happens (Fig. 66).

Different situation occurs for the images generated for Sentinel-1 after the seismic event (2016-2018 time period): the coverage is low as before the earthquake, but the mean velocity maps result less noisy and more reliable due to the larger number of starting images for ascending (60) and for the descending geometry (62).

Plotting the vertical and horizontal displacement time series in correspondence of the GPS 960701, 960703 and 960704 and of the Nakadake and Kusasenri crater (Fig. 58 and Fig. 59), it is possible to observe a lot of oscillations, where the most intensive peaks are associated to earthquakes. This fluctuation trend is related to the revisiting time (12 days for this sensor), that allows to detect also small displacements, probably due to the ascent of not erupted magma or degassing activity. In fact, as in the time span covered by Palsar-1, also the period from July 2016 up to mid-November 2016 was characterized by degassing activity without eruptions, according to Japan Meteorological Agency. This could explain the negative vertical trend, indicative of subsidence, in correspondence of the two main craters time series, after the earthquakes $M_w$ 4.8 on June 08, 2016, $M_w$ 4.1 August 01, 2018, $M_w$ 4.2 August 19, 2016 and $M_w$ 4.9 and $M_w$ 4.6 on August 31, 2016.
In the post-caldera central cones, horizontal and vertical displacements don't show the same trend observed as in the case of Palsar-1: during the subsidence, both Nakadake and Kusasenri crater shows a westward motion. This is not representative of the position of the plotted point respect to the magmatic chamber (Fig. 66), probably because of the strong WSW horizontal trend established during and after the Kumamoto earthquake, as shown in Fig. 41 and in Fig. 43, respectively. However, the horizontal and vertical displacements trend in correspondence of GPS 960701, 960703 and 960704 (Fig. 58; Fig. 59), agrees with the mean velocity GPS directions in Fig. 43 and in partly with Fig. 44, respectively. This means that having a large number of starting images with a shorter revisiting time, help to avoid obtaining a noisy result and allows to better overlap the SAR with the GPS phase.
Regarding Palsar-2 the mean velocity map in Fig. 61 has a wide noisy coverage with information over area not covered by Sentinel-1, thanks to the longer and more penetrating wavelength (23,5 cm), which allows to have more coherence and to better estimate the results. It is necessary to consider that the displacements in Palsar-2 is calculated along the LOS, because the estimation of vertical and horizontal components was not possible due to the unavailability of images acquired in ascending geometry.
Despite the noise, in Fig. 63, the GPS seem to have adapt well their phase with the SAR, because the plotted trend agrees with the mean velocity calculated for GPS.

Moreover, Palsar-2 seems to reflect and confirm the projection of the vertical rate movement of Sentinel-1 inside and outside the caldera rim. The difference between the two sensors consists in the revisiting time above the area, which determine the availability of images: from 14 days to three months for Palsar-2, and 12 days for Sentinel-1. In fact, in the case of Sentinel-1 the time series show more detailed displacements (Fig. 67).

In Fig. 67, are reported the displacements time series of Palsar-2 along the LOS (dark blue line), Sentinel-1 descending geometry (green line) and Sentinel-1 vertical (red line) and horizontal (light blue line) displacements for the same point located between Nakadake and Kusasenri crater in period 2016-2018. Green, red and dark blue line show a similar deflating trend: Palsar-2 and Sentinel-1 detect the same wide displacements, but with different rates. The subsidence surrounding the Nakadake and Kusasenri crater up to the present could be caused by the degassing activity from July 2016 to mid-November 2016, but it could be also a consequence of the post-seismic effect of the right-lateral strike slip Kumamoto earthquake. All the whole 2017 was characterized by a high intense degassing activity (600-2500 tons a day, according to Japan Meteorological Agency). This is mainly represented by the oscillations in the Sentinel-1 time-series thanks to the high number of images, while displacement time series from Palsar-2 don't clearly show this inflate-deflate cycle.

It must be considered that seismic events are present in the series and they should not be confused with peaks due to degassing activity. For instance, it is evident in the Palsar-2 time series (Fig. 63; Fig. 67), a vertical uplift in July-August 2017, related to the $M_w$ 4.5 earthquake on the July 01, 2017. Nevertheless, as shown in Fig. 67, uplift can be also be observed before the October 7, 2016 eruption: it can be due to magma ascent (indicated by red arrows) triggered by seismic events.

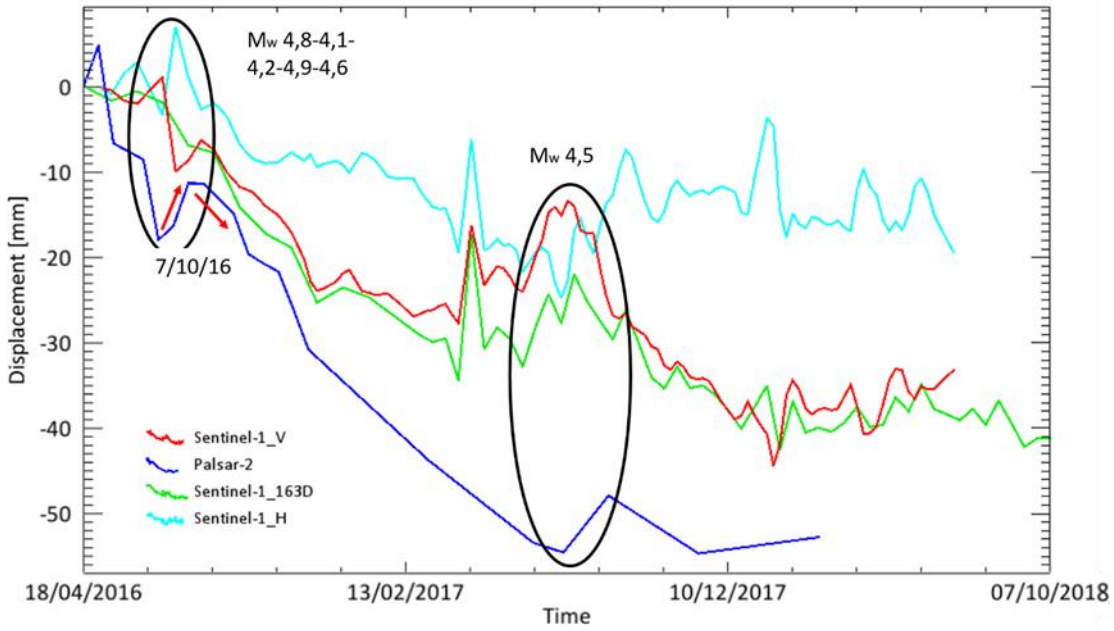


*Fig. 67: Time series plot of Sentinel-1 descending geometry, vertical and horizontal displacements compared with Palsar-2 descending geometry. Black ellipses highlight seismic events. Red arrows represent rise and decrease cycle due to October 7, 2016 eruption. Date format: DD/MM/YY.*

The uplift presents in the southwestern part of the caldera in the Palsar-2 mean velocity map (Fig. 61) and in the vertical displacements of Sentinel-1 (Fig. 57) could be related to the right lateral strike-slip movement of the Futagawa fault during the $M_w$ 7.0 Kumamoto earthquake on April 16, 2016. In particular, this is evident from the GPS 960701 mean vertical velocity: it shows a negative trend before the earthquake (Fig. 40) and a positive trend after (Fig. 44), confirming the GPS position in the foot wall zone respect to the Futagawa-Hinagu fault. This large change in the vertical trend could be caused by the strike-slip fault, but also by the rearrangement of the ground surface and the GPS after the event.

In Palsar-2 velocity map (Fig. 61) is evident a subsiding area between the Futagawa-Hinagu fault (orange line) and the Idenokuchi fault (red line). Idenokuchi fault was originated during the earthquake and was detected by InSAR, but also by seismic and geodetic survey. Its behaviour can be associated to the model proposed by Toda et al., (2016) in Fig. 68. Also, in the descending geometry of Sentinel-1 (Fig. 56) is possible to identify this tectonic structure, but in a less accurate way, because of the lower spatial coverage due to the different wavelength used by the two sensors.

This detachment block is also detected by the Palsar-2 displacements map in Fig. 65 and it is highlighted by white pixels indicative of a decorrelation factor caused by the wide displacement and by the large number of days between the two SAR images used for the processing respect Sentinel-1, correlated to the revisiting time. The differences between the two sensors also in this case can be related to the L-band used by Palsar-2, which detect larger movements, because of its wavelength, than the C-band used by Sentinel-1, which acquires mainly the small displacements and results more accurate. In fact, the Sentinel-1 horizontal displacement rates (Fig. 64) in correspondence of the GPS position, agree with the values reported by Kawamoto et al., (2016) more than Palsar-2.

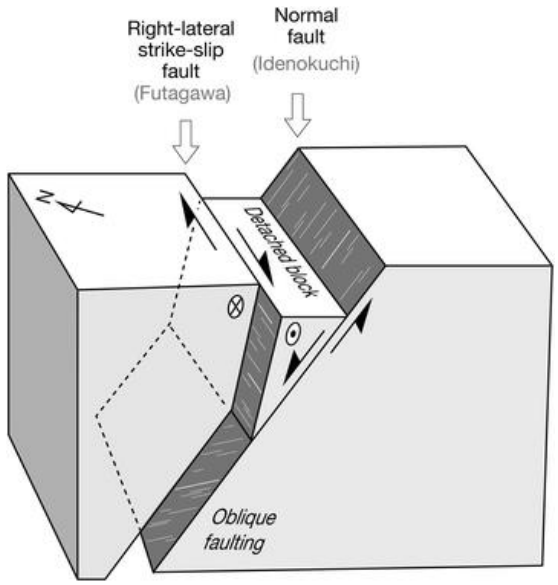


*Fig. 68: The planes of movement are shown in dark grey, and the white lines in these areas indicate the slip direction. (Toda et al., 2016)*

# Chapter 6: Conclusions

With the aim of studying the activity of the Aso volcano magma chamber, we decided to analyse three different SAR datasets acquired by Palsar-1 (2007-2011), Sentinel-1 (2014-2016 and 2016-2018) and Palsar-2 (2016-2018) sensors.

Using the SBAS (*Small Baseline Subset*), one of the commonly multi-temporal advanced DInSAR technique, it was possible to get information on ground deformations in wide areas characterized by dense vegetations.

During the processing, the employment of punctual information as GPS was important to adapt the SAR displacement values to the GPS time series. In case of noisy data or absence of coverage where the GPS are located, this optimisation didn't work well, as occurred in Palsar-1 processing, where the SAR time series don't reflect the GPS trend. Another factor that can condition the mismatch between interferometric data and GPS could be related to the elaboration of the GPS, in which strong WSW geodynamic contribute and seismic events, minor than Kumamoto earthquake, haven't been excluded. Besides the rearrangement of the GPS, the presence of seismic events in the SAR series masks the small oscillations caused by inflate-deflate cycle of the magma reservoir, in particular in Palsar-1 and -2, where the revisiting time is lower than Sentinel-1 and can't detect small displacements. Even if their low magnitude, some evidences of magma ascent triggered by earthquakes or degassing activity due to the hydrothermal system, are present in Palsar-2.

In general, a subsidence trend of the post-caldera central cones is evident during inactivity periods in according to Nobile et al. (2017), in particular in the time spans 2007-2011 (Palsar-1) and 2016-2018 (both Palsar-2 and Sentinel-1). The general trend along vertical and horizontal components in the post-caldera central cones corresponds to the GPS time series. The small fluctuations due to the volcanic activity and to the hydrothermal system (Biggs and Pritchard, 2017), can reflect where the position of the plotted point is respect to the magma chamber, mainly in Palsar-1 and Sentinel-1 (2014-2016). This behaviour is less evident in some case in Sentinel-1 from 2016 to 2018, because of the strong WSW horizontal component present in this period, but this can't be confirmed by Palsar-2

because of the absence of the horizontal displacements due to the unavailability of both the geometries.

In conclusion, Aso volcano is situated in an area affected by a complex tectonic component, which masks low intensity activity in the plots and makes difficult the identification of the magma reservoir. Moreover, the characteristics of the sensors employed, as the revisiting time, the number of available images and wavelength used, can influence the final coherence, the final coverage and the accuracy of the displacements detected and, consequently, the possibility to relate ground deformations with the behaviour of the volcanic apparatus.

# References

Abe, Y., Ohkura, T., Shibutani, T., Hirahara, K., Kato, M. (2010) 'Crustal structure beneath Aso Caldera, Southwest Japan, as derived from receiver function analysis', Journal of Volcanology and Geothermal Research. Elsevier B.V., 195(1), pp. 1–12. doi: 10.1016/j.jvolgeores.2010.05.011.

Aizawa, K., Asaue, H., Koike, K., Takakura, S., Utsugi, M., Inoue, H., Yoshimura, R. et al. (2017) 'Seismicity controlled by resistivity structure: The 2016 Kumamoto earthquakes, Kyushu Island, Japan', Earth, Planets and Space. Springer Berlin Heidelberg, 69(1), pp. 2–11. doi: 10.1186/s40623-016-0590-2.

Anderson, R. (1908) 'The Japanese Volcano Aso and its Large Caldera', The Journal of Geology, 16(6), pp. 499–526.

Asaue, H., Koike, K. and Yoshinaga, H., Shinichi, T. (2006) 'Magnetotelluric resistivity modeling for 3D characterization of geothermal reservoirs in the Western side of Mt. Aso, SW Japan', Journal of Applied Geophysics, 58, pp. 296–312.

Ayele, A., Jacques, E., Kassim, M., Kidane, T., Omar, A., Tait, S., Nercessian, A., de Chabalier, J.B., King, G. (2007) 'The volcano-seismic crisis in Afar, Ethiopia, starting September 2005.', Earth Planet. Sci. Lett., 255, pp. 177–187. doi: https://doi.org/10.1016/j.epsl.2006.12.014.

Baize, S. (2016) 'M7.2 Kumamoto Earthquake 14 and 15 April 2016 - A compilation of data and results with focus on surface rupture', Surface, Inqua Project, (April), pp. 1–86.

Bamler, R. and Just, D. (1993) 'Phase statistics and decorrelation in SAR interferograms', in Geoscience and Remote Sensing Symposium, 1993, IGARSS93 Better Understanding of Earth Environment, pp. 980–984.

Bamler, R. (2000) 'Principles Of Synthetic Aperture Radar', Surveys in Geophysics, 21.

Beccaro, L. (2018) Monitoraggio del vulcano attivo Sakurajima (Giappone) con dati SAR satellitari: dalla misura degli spostamenti alla modellazione e previsione dell'evoluzione. Università degli Studi di Padova.

Berardino P., Casu G., Fornaro R., Lanari R., Manunta M., Manzo M., Sansosti E. (2004) 'A quantitative analysis of the SBAS algorithm performance.', in International Geoscience and Remote Sensing Symposium, Anchorage. Alaska, pp. 3321–3324.

Berardino P., Fornaro G., Lanari R., S. E. (2002) 'A new algorithm for surface deformation monitoring based on small baseline differential interferograms.', IEEE Transactions on Geoscience and Remote Sensing, 40(11), pp. 2375–2383.

Biggs, J., Anthony, E.Y., Ebinger, C. J. (2009) 'Multiple inflation and deflation events at Kenyan volcanoes, East Afrinca Rift.', Geology, 37, pp. 979–982. doi: https://doi.org/10.1130/G30133A.1.

Biggs, J. and Pritchard, M. E. (2017) 'Global volcano monitoring: What does it mean when volcanoes deform?', Elements, 13(1), pp. 17–22. doi: 10.2113/gselements.13.1.17.

Blanpied, M. L., Lockner, D. A. and Byerlee, J. D. (1995) 'Frictional slip of granite at hydrothermal conditions', Journal of Geophysical Research: Solid Earth, 100(B7), pp. 13045–13064. doi: 10.1029/95JB00862.

Cigolini, C., Coppola, D. and Yokoo, A., Laiolo, M. (2018) 'The thermal signature of Aso Volcano during unrest episodes detected from space and ground-based measurements', Earth, Planets and Space. Springer Berlin Heidelberg, 70(1). doi: 10.1186/s40623-018-0831-7.

Dzurisin, D. (2007) Volcanic deformation. Geodetic monitoring techniques., Springer. Chichester, UK: Praxis Publishing.

Ferretti, A., Prati, C. and Rocca, F. (2001) 'Permanent Scatters in SAR Interferometry.', IEEE Transactions on Geoscience and Remote Sensing, 39(1), pp. 8–20.

Ferretti A., Monti-Guarnieri A., Prati C., Rocca F., M. D. (2007) InSAR Principles: Guidelines for SAR Interferometry Processing and Interpretation, ESA-TM 19, ESA Publication. Edited by K. Fletcher. The Netherlands.

Fiaschi, S., Closson, D., Abou Karaki, N., Pasquali, P., Riccardi, P., Floris, M. (2017) 'The complex karst dynamics of the Lisan Peninsula revealed by 25 years of DInSAR observations. Dead Sea, Jordan.', ISPRS Journal of Photogrammetry and Remote Sensing, 130, pp. 358–369. doi: https://doi.org/10.1016/j.isprsjprs.2017.06.008.

Fisher, R.V. and Schmincke, H. U. (1984) Pyroclastic Rocks. Springer-Verlag, Berlin Heidelberg.

Fitch, T. J. (1972) 'Plate convergence, transcurrent faults, and internal deformation adjacent to southeast Asia and western Pacific', Lamont-Doherty Geological Observatory Contribution, (0000).

Fujiwara, S., Yarai, H., Kobayashi, T., Morishita, Y., Nakano, T., Miyahara, B., Nakai, H., Miura, Y., Ueshiba, H., Kakiage, Y., Une, H. (2016) 'Small-displacement linear surface ruptures of the 2016 Kumamoto earthquake sequence detected by ALOS-2 SAR interferometry', Earth, Planets and Space. Springer Berlin Heidelberg, 68(1), p. 160. doi: 10.1186/s40623-016-0534-x.

Gomarasca, M. A. (2009) Basics of geomatics, Basics of Geomatics. Springer Dordrecht Heidelberg.

Hao, J., Ji, C. and Yao, Z. (2017) 'Slip history of the 2016 Mw7.0 Kumamoto earthquake: Intraplate rupture in complex tectonic environment', Geophysical Research Letters, 44(2), pp. 743–750. doi: 10.1002/2016GL071543.

Hooper, A., Zebker, H., Segall, P. and Kampes, B. (2004) 'A new method for measuring deformation on volcanoes and other natural terrains using InSAR persistent scatterers.', Geophysical Research Letters, 31(23).

Huang, Y.-C. et al. (2018) 'Shallow volcanic reservoirs and pathways beneath Aso caldera revealed using ambient seismic noise tomography', Earth, Planets and Space. Springer Berlin Heidelberg, 70(1), p. 169. doi: 10.1186/s40623-018-0941-2.

Ichikawa, K. (1980) 'Geohistory of the Median Tectonic Line of Southwest Japan.', Memoir Geol. Soc. Japan, 18, pp. 187–212.

Iisaka, J. (1998) Synthetic aperture RADAR image handbook. Tokyo: Asakura.

Ishibashi, K. (1986) 'Transformation of Northeast Japan to North American plate versus eastward movement of Southwest Japan', Monthly Chikyu, 8, pp. 103–144.

Kagami, H. (1989) 'Origin of Nankai fore-arc sliver and uplifting of coastal mountains in southwest Japan', Report of the Institute of the Kuroshio Sphere, Kochi University., 4, pp. 21–35.

Kamata, H. (1989) 'Volcanic and structural history of the Hohi volcanic zone, central Kyushu, Japan', Bulletin of Volcanology, 51(5), pp. 315–332. doi: 10.1007/BF01056894.

Kamata, H. (1998) 'Quaternary volcanic front at the junction of the south-west Japan Arc and the Ryukyu Arc', Journal of Asian Earth Sciences, 16(1), pp. 67–75. doi: 10.1016/S0743-9547(97)00044-5.

Kamata, H. and Kodama, K. (1999) 'Volcanic history and tectonics of the Southwest Japan Arc', Island Arc, 8(3), pp. 393–403. doi: 10.1046/j.1440-1738.1999.00241.x.

Kaneko, K., Inoue, K., Koyaguchi, T., Yoshikawa, M., Shibata, T., Takahashi, T., Furukawa, K. (2015) 'Magma plumbing system of the Aso-3 large pyroclastic eruption cycle at Aso volcano, Southwest Japan: Petrological constraint on the formation of a compositionally stratified magma chamber', Journal of Volcanology and Geothermal Research, pp. 41–58. doi: 10.1016/j.jvolgeores.2015.07.016.

Kaneko, K. et al. (2007) 'Repeated large-scale eruptions from a single compositionally stratified magma chamber: An example from Aso volcano, Southwest Japan', Journal of Volcanology and Geothermal Research, 167(1–4), pp. 160–180. doi: 10.1016/j.jvolgeores.2007.05.002.

Kato, A., Nakamura, K. and Hiyama, Y. (2016) 'The 2016 Kumamoto earthquake sequence', Proceedings of the Japan Academy, Series B, 92(8), pp. 358–371. doi: 10.2183/pjab.92.359.

Kawamoto, S., Hiyama, Y., Kai, R., Suga, F., Yamaguchi, K., Furuya, T., Abe, S., Takamatsu, N. (2016) 'Crustal Deformation Caused by the 2016 Kumamoto Earthquake Revealed by GEONET', Bulletin of the Geospatial Information Authority of Japan, 64, pp. 27–33.

Kobayashi, T., Morishita, Y., Munekane, H. (2018) 'First detection of precursory ground inflation of a small phreatic eruption by InSAR.', Earth and Planet. Sci. Lett., 491, pp. 244–254. doi: https://doi.org/10.1016/j.epsl.2018.03.041.

Kodama, K., Tashiro, H. and Takeuchi, T. (1995) 'Quaternary counterclockwise rotation of south Kyushu, southwest Japan', Geology, 23(9), pp. 823–826. doi: 10.1130/0091-7613(1995)023<0823:QCROSK>2.3.CO;2.

Kumahara Y, Goto H, Nakata T, Ishiguro S, Ishimura D, Ishiyama T, Okada S, Kagohara K, Kashihara S, Kaneda H, Sugito N, Suzuki Y, Takenami T, Tanaka K, Tanaka T, Tsutsumi H,

Toda S, Hirouchi D, Matsuta N, Mita T, Moriki H, Yoshida H, W. M. (2016) 'Distribution of surface rupture associated the 2016 Kumamoto earthquake and its significance.', in Abstract (MIS34-05) of the Japan Geoscience Union Meeting 2016.

Kusumoto, S. (2016) 'Dip distribution of Oita – Kumamoto Tectonic Line located in central Kyushu, Japan, estimated by eigenvectors of gravity gradient tensor', Earth, Planets and Space. Springer Berlin Heidelberg, 68(153). doi: 10.1186/s40623-016-0529-7.

Lin, A., Satsukawa, T., Wang, M., Mohammadi Asl, Z., Fueta, R., Nakajima, F. (2016) 'Coseismic rupturing stopped by Aso volcano during the 2016 Mw 7.1 Kumamoto earthquake, Japan', Science, 354(6314).

Loveless, J. P. and Meade, B. J. (2010) 'Geodetic imaging of plate motions, slip rates, and partitioning of deformation in Japan', Journal of Geophysical Research, 115(B2), p. B02410. doi: 10.1029/2008JB006248.

Luzi, G. (2010) Ground based SAR interferometry: a novel tool for Geoscience and Remote Sensing New Achievement. Edited by D. Riccio and P. Imperatore.

Mahony, S. H., Wallace, L. M., Miyoshi, M., Villamor, P., Sparks, R. S. J., Hasenaka, T. and Science, G. N. S., Drive, F., Hutt, L. (2011) 'Volcano-tectonic interactions during rapid plate-boundary evolution in the Kyushu region, SW Japan', Geological Society of America Bulletin, 123(11), pp. 2201–2223. doi: 10.1130/B30408.1.

Matsubara, Y. and Seno, T. (1980) 'Paleogeographic reconstruction of the Philippine Sea at 5 m.y.B.P.', Earth and Planetary Science Letters, 51, pp. 406–414.

Matsumoto, N., Yoshihiro, H. and Sawada, A. (2016) 'Continuity, segmentation and faulting type of active fault zones of the 2016 Kumamoto earthquake inferred from analyses of a gravity gradient tensor', Earth, Planets and Space. Springer Berlin Heidelberg, 68(1). doi: 10.1186/s40623-016-0541-y.

Merryman Boncori, J.P., Papoutsis, I.; Pezzo, G., Atzori, S., Ganas, A., Karastathis, V., Salvi, S., Kontoes, C., Antonioli, A. (2015) 'The February 2014 Cephalonia earthquake (Greece): 3D deformation field and source modeling from multiple SAR techniques.', Seismol. Res. Lett., 86, pp. 1–14. doi: https://doi.org/10.1785/0220140126.

Miyabuchi, Y., Ikebe, S. ichiro and Watanabe, K. (2008) 'Geological constraints on the 2003-2005 ash emissions from the Nakadake crater lake, Aso Volcano, Japan', Journal of Volcanology and Geothermal Research. Elsevier B.V., 178(2), pp. 169–183. doi: 10.1016/j.jvolgeores.2008.06.025.

Miyabuchi, Y. and Terada, A. (2009) 'Subaqueous geothermal activity revealed by lacustrine sediments of the acidic Nakadake crater lake, Aso Volcano, Japan', Journal of Volcanology and Geothermal Research. Elsevier B.V., 187(1–2), pp. 140–145. doi: 10.1016/j.jvolgeores.2009.08.001.

Moro, M., Chini, M., Saroli, M., Atzori, S., Stramondo, S., Salvi, S. (2011) 'Analysis of large, seismically induced, gravitational deformations imaged by high-resolution COSMO-SkyMed synthetic aperture RADAR.', Geology, 39, pp. 527–530. doi: . https://doi.org/10.1130/G31748.1.

Nakada, S. and Kamata, H. (1991) 'Temporal change in chemistry of magma source under Central Kyushu, Southwest Japan: progressive contamination of mantle wedge.', Bulletin of Volcanology, 53(3), pp. 182–194.

Nakata, K. and Imaizumi, T. (2002) 'Digital active fault map of Japan'. Tokyo: University of Tokyo Press, p. 60.

National Institute of Advanced Industrial Science and Technology (2007) Investigations on the activity and tectonic history of the Futagawa- Hinagu fault zone, Report of Results on "Basic Investigations of Additional Fault Zone," no. H18-7.

Nishimura, S. and Hashimoto, M. (2006) 'A model with rigid rotations and slip deficits for the GPS-derived velocity field in Southwest Japan', Tectonophysics, 421(3–4), pp. 187–207. doi: 10.1016/j.tecto.2006.04.017.

Nobile, A., Acocella, V., Ruch, J., Aoki, Y., Borgstrom, S., Siniscalchi, V., Geshi, N. (2017) 'Steady subsidence of a repeatedly erupting caldera through InSAR observations: Aso, Japan', Bulletin of Volcanology, 79(5). doi: 10.1007/s00445-017-1112-1.

Ohsawa, S., Saito, T., Yoshikawa, S., Mawatari, H., Yamada, M., Amita, K., Takamatsu, N. Sudo, Y., Kagiyama, T. (2010) 'Color change of lake water at the active crater lake of Aso volcano, Yudamari, Japan: Is it in response to change in water quality induced by volcanic activity?', Limnology, 11(3), pp. 207–215. doi: 10.1007/s10201-009-0304-6.

Okada, A. (1980) ‘Quaternary faulting along the Median Tectonic Line of southwest Japan’, Mem. Geol. Soc. Japan, 18, pp. 79–108.

Okumura, K. (2016) Earthquake Geology of the April 14 and 16, 2016 Kumamoto Earthquakes.

Onda, Y., Ohsawa, S. and Takamatsu, N. (2003) ‘A colorimetric and geochemical study of the coloration factor of hyper-acid active crater lakes’, Jpn J Limnol, 64, pp. 1–10.

Ono, K., Watanabe, K., Hoshizumi, H., Ikebe, S. (1995) ‘Ash eruption of the Naka-dake crater, Aso volcano, southwestern Japan’, Journal of Volcanology and Geothermal Research, 66(1–4), pp. 137–148. doi: 10.1016/0377-0273(94)00061-K.

Ono, K. and Watanabe, K. (1985) ‘Geological Map of Aso Volcano’.

Ono K, Matsumoto Y, Miyahisa M, Teraoka Y, K. N. (1977) ‘Geology of the Taketa district. Quadrangle Series 1:50000 Map’, Geol Surv Japan, pp. 1–145.

Ono, K. and Watanabe, K. (1983) ‘Aso Caldera’, Earth Monthly, 44, pp. 73–82.

Di Paola, G., Alberico, I., Aucelli, P.P.C., Matano, F., Rizzo, A., Vilardo, G. (2018) ‘Coastal subsidence detected by Synthetic Aperture Radar interferometry and its effects coupled with future sea-level rise: the case of the Sele Plain (Southern Italy).’, J. of Flood Risk Manag., 11, pp. 191–206. doi: https://doi.org/ 10.1111/jfr3.12308.

Pasa, D. (2014) Valutazione del tasso di subsidenza nell’area di Ravenna attraverso tecniche avanzate di interferometria RADAR differenziale. Università degli Studi di Padova.

Pasquali P., Cantone A., Riccardi P., Defilippi M., Ogushi F., Gagliano S., Tamura, M. (2014) ‘Mapping of ground deformations with interferometric stacking tecniques. Land applications of RADAR remote sensing’, InTech 2014, pp. 234–259.

Prati, C. (2008) ‘Introduction to SAR and InSAR.’, in IV Conférence canadienne sur les géorisques: des cause à la gestion, Université Laval.

Richards, J. A. (2009) ‘Remote Sensing with imaging RADAR.’, Springer Series on Signals and Communication Technology, p. 373.

Sabins, F. F. (1997) Remote Sensing and Principles and Image Interpretation. New York: WH

Freeman.

Sagiya, T. (2004) 'A decade of GEONET: 1994-2003 - The continuous GPS observation in Japan and its impact on earthquake studies -', Earth, Planets and Space, 56(8), pp. 1994–2003. doi: 10.1186/BF03353077.

Sarmap, S. A. (2009) 'SAR-Guidebook. Synthetic Aperture Radar Systems and Signal Processing.' Switzerland: Sarmap, S.A., pp. 1–274.

Sarmap, S. A. (2014) 'Sarscape 5.1 User Guide'. Switzerland: Sarmap, S.A., pp. 1–841.

Seno, T., Maruyama, S. (1984) 'Paleogeographic reconstruction and origin of the Philippine Sea.', Tectonophysics, 102, pp. 53–84.

Seno, T. (1985) '"Northern Honshu microplate" hypothesis and tectonics in the surrounding region', Journal of Geodetic Society of Japan, 31, pp. 23–106.

Shang-Ho, Y. (2008) Volcano Deformation Modeling Using Radar Inteferometry. VDM Verlag Dr. Mueller e.K.

Shinjo, R. and Kato, Y. (2000) 'Geochemical constraints on the origin of bimodal magmatism at the Okinawa Trough, an incipient back-arc basin', LITHOS. Elsevier, 54(3–4), pp. 117–137. doi: 10.1016/S0024-4937(00)00034-7.

Shinohara, H., Yokoo, A. and Kazahaya, R. (2018) 'Variation of volcanic gas composition during the eruptive period in 2014–2015 at Nakadake crater, Aso volcano, Japan', Earth, Planets and Space. Springer Berlin Heidelberg, 70(1). doi: 10.1186/s40623-018-0919-0.

Sibuet, J., Hsu, S., Shyu, C., Liu, C. (1995) Backarc Basin, Tectonics and Magmatism. Edited by B. Taylor. New York: Plenum Press.

Sudo, Y., Tsutsui, T. and Nakaboh, M., Yoshikawa, M., Yoshikawa, S., Inoue, H. (2006) 'Ground deformation and magma reservoir at Aso volcano: Location of deflation source derived from long-term geodetic surveys', Bull. Volcanol. Soc. Jpn., 51(5), p. 291–309 (in Japanese with English abstract). doi: 10.18940/kazan.51.5_291.

Sudo, Y. and Kong, L. (2001) 'Three-dimensional seismic velocity structure beneath Aso Volcano, Kyushu, Japan', Bulletin of Volcanology, 63(5), pp. 326–344. doi:

10.1007/s004450100145.

Taira, A. (2001) 'Tectonic Evolution of the Japanese Island Arc System', Annual Review of Earth and Planetary Sciences, 29(1), pp. 109–134. doi: 10.1146/annurev.earth.29.1.109.

Tessari, G., Floris, M., Pasquali, P. (2017) 'Phase and amplitude analyses of SAR data for landslide detection and monitoring in non-urban areas located in the North-Eastern Italian pre-Alps.', Environ. Earth Sci., 76(85). doi: https://doi.org/10.1007/s12665-017-6403-5.

Tessari, G. (2014) Caratterizzazione e modellazione di fenomeni geologici di instabilità attraverso tecniche di telerilevamento satellitare e simulazioni numeriche. Università degli Studi di Padova.

Toda, S. et al. (2016) 'Slip-partitioned surface ruptures for the Mw 7.0 16 April 2016 Kumamoto, Japan, earthquake', Earth, Planets and Space. Springer Berlin Heidelberg, 68(1), p. 188. doi: 10.1186/s40623-016-0560-8.

Tomás, R., Romero, R., Mulas, J., Marturià, J.J., Mallorquí, J.J., Lopez- Sanchez, J.M., Herrera, G., Gutiérrez, F., González, P.J., Fernández, J., Duque, S., Concha-Dimas, A., Cocksley, G., Castañeda, C., Carrasco, D., Blanco, P. (2014) 'Radar interferometry techniques for the study of ground subsidence phenomena: a re-view of practical issues through cases in Spain.', Environ. Earth. Sci., 71, pp. 163–181. doi: https://doi.org/10.1007/s12665-013-2422-z.

Tosi, L., Da Lio, C., Strozzi, T, Teatini, P. (2016) 'Combining L- and X-Band SAR Interferometry to Assess Ground Displacements in Heterogeneous Coastal Environments: The Po River Delta and Venice Lagoon, Italy.', Remote Sens., 308. doi: https://doi.org/10.3390/rs8040308.

Triglia, D. S. (2010) Applicazioni di interferometria RADAR da satellite per la generazione di mappe di spostamento nell'analisi di fenomeni dinamici. University of Bologna.

Tsukuda, E. (1992) 'Active tectonics of southwest Japan arc controlled by the westward translation of the foreare sliver', Memoirs of the Geological Society of Japan, (40), pp. 235–250.

Unglert, K., Savage, M. K., Fournier, N., Ohkura, T., Abe, Y. (2011) 'Shear wave splitting, vP/vS, and GPS during a time of enhanced activity at Aso caldera, Kyushu', Journal of Geophysical Research: Solid Earth, 116(11), pp. 1–14. doi: 10.1029/2011JB008520.

Usami, T. (1996) 'Materials for Comprehensive List of Destructive Earthquakes in Japan.'

Tokyo: University of Tokyo Press, p. 423.

Wasowski, J. and Bovenga, F. (2014) 'Investigating landslides and unstable slopes with satellite Multi Temporal Interferometry: current issues and future perspectives', Engineering Geology, 174, pp. 103–138. doi: 10.1016/j.enggeo.2014.03.003.

Wunderman, R. (2012) 'Global Volcanism Program, 2012. Report on Asosan (Japan). Smithsonian Institution', Bulletin of the Global Volcanism Network, 37(8).

Xie, M., Huang, J., Wang, L., Huang, J., Wang, Z. (2016) 'Early landslide detection based on D-InSAR technique at the Wudongde hydropower reservoir', Environ. Earth Sci., 75(717). doi: https://doi.org/10.1007/s12665-016-5446-3.

Yerro, A., Corominas, J., Monells, D., Mallorquí, J. J. (2014) 'Analysis of the evolution of ground movements in a low densely urban area by means of DInSAR technique.', Eng. Geol., 170, pp. 52–65. doi: https://doi.org/10. 1016/j.enggeo.2013.12.002.

Yu, C., Li, Z., Chen, J., Hu, J. C. (2018) 'Small magnitude co-seismic deformation of the 2017 Mw 6.4 Nyingchi earthquake revealed by InSAR measurements with atmospheric correction.', Remote Sens., 10(684). doi: https://doi.org/ 10.3390/rs10050684.

Zhao, C.; Kang, Y.; Zhang, Q.; Lu, Z.; Li, B. (2018) 'Landslide identification and monitoring along the Jinsha River catchment (Wudongde reservoir area), China, using the InSAR method.', Remote Sens., 10(993). doi: https://doi.org/10.3390/rs10070993.

Zhao, D., Yanada, T., Hasegawa, A., Umino, N., Wei, W. (2012) 'Imaging the subducting slabs and mantle upwelling under the Japan Islands', Geophysical Journal International, 190(2), pp. 816–828.

Zhou, X., Chang, N. Bin and Li, S. (2009) 'Applications of SAR interferometry in earth and environmental science research', Sensors, 9(3), pp. 1876–1912. doi: 10.3390/s90301876.